Supramolecular Order and Dynamics of Functional Materials Studied by Solid State NMR

Dissertation
Zur Erlangung des Grades

"Doktor des Naturwissenschaften"

am Fachbereich Chemie und Pharmazie der
Johannes Gutenberg-Universität
in Mainz

Mihail Mondeshki
Geboren in Sofia

Mainz, Dezember 2007

Tag der mündlichen Prüfung: 05.12.2007

CONTENTS

Results

Abbreviations and Acronyms

BABA *ba*ck-to-*ba*ck
CODEX *c*enterband-*o*nly *d*etection *o*f *ex*change
CSA *c*hemical *s*hift *a*nisotropy
CP *c*ross-*p*olarization
CW *c*ontinuous-*w*ave
DD *d*ipolar *d*ecoupling
DF *d*irector *f*rame
DMS dimethylsulfone $(CH_3)_2SO_2$
DQ *d*ouble-*q*uantum
DQF double-quantum filtered
DSC *d*ifferential *s*canning *c*alorimetry
ERM *e*volution *r*otor *m*odulation
FET *f*ield *e*ffect *t*ransistor
FID *f*ree *i*nduction *d*ecay
FT *f*ourier *t*ransformation
FWHM *f*ull *w*idth at *h*alf *m*aximum
HBC hexa-*peri*-*h*exa*b*enzo*c*oronene
HDOR *h*eteronuclear *d*ipolar *o*rder *r*otor-*e*ncoding
HETCOR *h*eteronuclear *c*orrelation
HMQ *h*eteronuclear *m*ultiple-*q*uantum
HSQC *h*eteronuclear *s*ingle-*q*uantum *c*orrelation
INEPT *i*nsensitive *n*uclei *e*nhanced by *p*olarization *t*ransfer
LAB *lab*oratory frame
LC *l*iquid *c*rystal
LED *l*ight *e*mitting *d*iode
MAS *m*agic-*a*ngle *s*pinning
MF *m*olecular *f*rame
MQ *m*ultiple-*q*uantum
NMR *n*uclear *m*agnetic *r*esonance
PAS *p*rincipal *a*xes *s*ystem
Pc *p*hthalo*c*yanine
Pch2 metal-free *p*hthalo*c*yanine
POM *p*olarized *o*ptical *m*icroscopy
PTCDI *p*erylene *t*etracarboxy *di*i*mide*
REDOR *r*otational *e*cho, *d*ouble *r*esonance
REREDOR *r*otor *e*ncoded *r*otational *e*cho, *d*ouble *r*esonance
REPT *r*ecoupled *p*olarization *t*ransfer
RF *r*adio *f*requency
RRE *r*econversion *r*otor *e*ncoding
RT *r*oom *t*emperature
SAXS *s*mall-*a*ngle *X*-ray *s*cattering
SQ *s*ingle-*q*uantum
SUPER *s*eparation of *u*ndistorted *p*owder patterns by *e*ffortless *r*ecoupling
TEDOR *t*ransferred *e*cho, *d*ouble *r*esonance
TOSS *to*tal *s*uppression of spinning *s*idebands
TPPI *t*ime *p*roportional *p*hase *i*ncrementation
TPPM *t*wo-*p*ulse *p*hase-*m*odulated
WAXS *w*ide-*a*ngle *X*-ray *s*cattering

Chapter 1. Introduction

Since the discovery of the nuclear magnetic resonance (NMR) by Purcell[1] and Bloch[2] in 1946 the technique has developed to become one of the most powerful analytical methods with applications in all areas of science. The first NMR experiments, conducted independently on solid (paraffin) and liquid (water) samples using proton (^{1}H) resonances, proved the applicability of the NMR spectroscopy to both liquid and solid phases of condensed matter, thus giving the start respectively of two research areas - liquid-state (or high resolution) NMR spectroscopy and solid state NMR spectroscopy. Later in 1973, magnetic resonance imaging (MRI) was developed by Lauterburg[3] and Mansfield[4] to join the former methods; all three nowadays are considered as more or less independent research and application fields.

The broad application of solid state NMR was initially hampered by its inherent lack of spectral resolution, expressed in severe line broadening in the static spectra. Anisotropic interactions like the anisotropy of the chemical shift (CSA) due to the different crystallite orientations in the powder, the homo- and heteronuclear dipole-dipole couplings, as well as the much stronger quadrupolar couplings, cause resonance broadening. To provide sufficient spectral resolution the *magic angle spinning* (MAS)[5,6] technique was developed and is nowadays routinely used. The basic concept is applying fast sample rotation about an axis inclined at the magic angle (54.7°) with frequencies exceeding the strength, and thus averaging, the CSA and dipolar couplings (typically up to 30 kHz, in some cases 50 kHz[7] or even 70 kHz[8]). This results in sharp spectral lines but comes at the price of a loss of valuable information inherent to these anisotropic interactions. So other techniques, namely the *recoupling* methods[9,10], are needed to selectively reintroduce the interactions of interest and respectively benefit from the related information. These *recoupling* methods are accomplished by the application of *radio frequency* (RF) *pulse* sequences which induce a "counterrotation" of the spin part of the nuclear wave function and thus *recouple* the investigated anisotropic interaction. So, a precise measurement of dipolar coupling strengths is achieved in combination with chemical shift resolution and thus acquiring accurate internuclear distances (up to 2 nm) or angles, as well as evaluating the site specific molecular dynamics.

Therefore, solid state nuclear-magnetic resonance (NMR) spectroscopy is a powerful (often indispensable) analytical tool for investigating the structure, organization and

dynamics in different supramolecular systems. This information is particularly needed in the field of solid polymers, liquid crystals, as well as in the case of any insoluble organic or inorganic compound. In addition, based on this knowledge, it is easier to direct the synthetic efforts to fine-tune the existing or create novel structures with improved properties.

Recently a lot of scientific interest has been focused on the design, synthesis and detailed characterization of columnar functional materials for use in optoelectronic devices. Examples of such materials are hexasubstituted hexa-peri-hexabenzocoronenes, tetra- or octafunctionalized phthalocyanines and phthalocyanine-perylene mixtures (Figure 1). Solid state NMR investigations of the structure, supramolecular assembly and dynamics of these compounds are described in this work together with complementary spectroscopic studies like X-ray, DSC and dielectric spectroscopy.

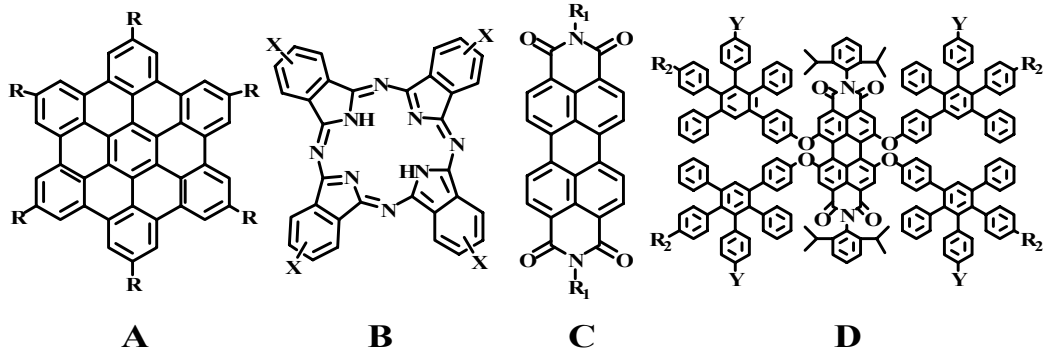

Figure 1. *Core structures of the (A) hexa-peri-hexabenzocoronenes, (B) tetra- or octasubstituted phthalocyanines, (C) perylenetetracarboxydiimides, (D) dendronized perylene tetracarboxydiimides*

The hexa-peri-hexabenzocoronenes (HBCs), recently discovered coronene analogues, are known to form thermotropic columnar liquid crystalline mesophases over exceptionally broad temperature ranges depending on the type, number and functionality of the side chains attached. The HBC disc-shaped molecules stack one above the other mostly due to π–interactions. The columns thus formed, as the aromatic cores, are a hole-transporting media (if not further modified), with the flexible side-chains, being practically insulators, may serve as a good example for the so-called organic nano-wires. Also, the very high one dimensional charge carrier mobility, reaching values of 1.13 $cm^2V^{-1}s^{-1}$ for some representatives of the hexa-*peri*-hexabenzocoronenes[11], combined with good processability, are of particular interest for potential applications in field-effect transistors (FETs) and photovoltaics (solar cells. The influence of the length, respectively the spatial requirements of

branched side-chains on the columnar stacking and dynamics of the three HBC derivatives, was investigated by applying different solid state NMR recoupling techniques.

As the supramolecular order as well as the charge carrier mobility is determined largely from the nature of the stacked aromatic cores, another class of columnar liquid crystals, namely phthalocyanines (Figure 1), became a subject of interest. Here it should be mentioned that phthalocyanines are the second most important class of colorants, and copper phthalocyanine is the single largest-volume colorant sold. In addition, phthalocyanine compounds have found use in many important high-tech applications, including photodynamic therapy, optical data storage and solar screens. Presently, other possible usage of this industrially important class of compounds, namely in optoelectronic devices, is thoroughly investigated. To gain further insight in the organization and site-specific dynamics of liquid-crystalline columnar phthalocyanines (in particular esterified octacarboxyphthalocyanines) we applied (to the best of our knowledge) for the first time solid state NMR recoupling techniques. Also, for the first time we proved the applicability of the solid state NMR recoupling methods to columnar donor-acceptor mixtures for potential use in solar cells (phthalocyanine-perylene mixtures), where the need for spectral resolution combined with solid state effects makes the study quite demanding. Another question addressed in this thesis and extending the investigations on the perylene derivatives was to determine the influence of the side chains length and secondary structure on the packing and dynamics in polylysinesubstituted polyphenylene dendronized perylenes.

Chapter 2. General Theoretical Background

NMR Basics

In quantum mechanics the state of a system (the sample measured in an NMR experiment for example) is described by a continuous function of space $\psi_{full}(x,t)$ in case of a single spatial coordinate *x*. If all interactions in such a system are time invariant, the wavefunction is the solution of the time-independent Schrödinger equation[12]:

$$\hat{\mathrm{H}}\psi(x) = E\psi(x) \tag{2.1}$$

where $\hat{\mathrm{H}}$ is the Hamiltoinian operator, which contains terms describing both the kinetic and potential energy of the system. As the pulses applied during NMR experiments introduce time dependence, the time-dependent Schrödinger equation must be solved:

$$\hat{\mathrm{H}}_{full}(t)\psi_{full}(x,t) = -i\hbar\frac{\partial\psi_{full}(x,t)}{\partial t} \tag{2.2}$$

The wavefunction ψ_{full}, which is a solution of equation 2.2 and fully describes the system, contains information about the position, spin and velocity of all electrons and nuclei in the sample. However, it is practically not possible to calculate the full wavefunction, i.e. to solve the full time-dependent Schrödinger equation. So, it is assumed that the magnetic and electric influences of the rapidly moving electrons are averaged and the nuclei experience the average interaction. This average is then taken into account in the nuclear spin Hamiltonian $\hat{\mathrm{H}}_{spin}$, which contains information only about the direction of the nuclear polarization. This massive simplification, known as the spin Hamiltonian hypothesis[13], is based on the different timescales of motion of electrons and nuclei, and holds for ordinary temperatures. So, the wavefunction ψ_{spin}, which is a solution of equation 2.2 thus simplified, describes only the nuclear spin states of all spins in the sample.

2.1. Density Operator and Liouville-von-Neumann Equation

In a sample, there are approximately 10^{17} spins. It is theoretically possible, but practically not feasible to calculate each individual contribution of a single spin to the z magnetization. Thus, the spectroscopic information is acquired as an ensemble average over the individual spins in the sample. The method used is called the density operator[12], which makes possible to describe the quantum state of the entire ensemble without referring to the individual spin states.

A single spin in a general superposition state is described by the wavefunction $|\psi\rangle$, which in the bra-ket notation is given as:

$$|\psi\rangle = c_i|i\rangle \tag{2.3}$$

Thus for a spin-½ nucleus, the wavefunction is written as:

$$|\psi\rangle = c_\alpha|\alpha\rangle + c_\beta|\beta\rangle \tag{2.4}$$

where c_α and c_β are the normalized superposition coefficients for the respective eigenstates $|\alpha\rangle$ and $|\beta\rangle$. The bulk magnetization measured in an NMR experiment is proportional to the coefficients of the eigenstates. If all spins have identical wavefunctions, i.e. are in a pure state (only existing at 0 K), the spatial components of the magnetization are proportional to:

$$M_x \propto N_i(c_\alpha c_\beta^* + c_\beta c_\alpha^*) = N_i|c_\alpha||c_\beta|\cos\varphi \tag{2.5}$$

$$M_y \propto N_i(c_\alpha c_\beta^* - c_\beta c_\alpha^*) = N_i|c_\alpha||c_\beta|\sin\varphi \tag{2.6}$$

$$M_z \propto N_i(c_\alpha c_\alpha^* - c_\beta c_\beta^*) \tag{2.7}$$

as with N_i is denoted the number of spins in the sample, φ is the angle between the direction of the applied magnetic field and the direction of the bulk magnetization and with c_x^* is denoted the complex conjugate coefficient. However, in the conditions of the NMR experiment the spins in the sample exist in a mixed state, characterized by the wavefunction

$|\psi_i\rangle$. The mixed state, on the other hand, can be represented by a sum of n sub-ensemble states, each characterized by the same wavefunction (it may be considered as consisting of n sub-ensembles, each having the same wavefunction). In each sub-ensemble the number of spins is related to the probability p_i, as $p_i<1$ ($p_i = 1$ is valid only for a pure state, where the Boltzman distribution is invalid and all spins are in the lowest energy α state). In the mixed state c_α and c_β can be replaced by their weighted averages, so that:

$$\overline{c_\alpha c_\beta^*} = \sum_{i=1}^{n} p_i (c_\alpha c_\beta^*) \tag{2.8}$$

These average terms might then be used to describe the motion of the bulk magnetization from an ensemble of spins with respect of time. This is done by means of a density operator which in its matrix representation is given as:

$$\hat{\rho} = \begin{pmatrix} \overline{c_\alpha c_a^*} & \overline{c_\alpha c_\beta^*} \\ \overline{c_\beta c_\alpha^*} & \overline{c_\beta c_\beta^*} \end{pmatrix} \tag{2.9}$$

The diagonal elements of the density operator are called populations of the states $|\alpha\rangle$ and $|\beta\rangle$. The off-diagonal elements are called coherences between the states $|\alpha\rangle$ and $|\beta\rangle$. The populations sum to unity since the state of each spin is normalized. The difference between the two populations is the polarization of the system (in the direction of the applied field). If populations of the two states are equal, there is no net longitudinal polarization. The number of spin states n_{es} (also called eigenstates) depends on the different spin interactions (upon spin coupling the number of eigenstates increases), as well as on the spin quantum number I, so that:

$$n_{es} = \prod_{i=1}^{n} (2I_i + 1) \tag{2.10}$$

Thus for a pair of coupled spin-½ nuclei the number of elements of the 4 x 4 matrix is 16. Each element in the matrix represents one of the possible superpositions of the eigenstates. In the matrix, there are 4 populations and 12 coherences (which correspond to the possible transitions between the population states as shown on Figure 1).

$$\hat{\rho} = \begin{pmatrix} \overline{c_{\alpha\alpha} c_{\alpha\alpha}^*} & \overline{c_{\alpha\alpha} c_{\alpha\beta}^*} & \overline{c_{\alpha\alpha} c_{\beta\alpha}^*} & \overline{c_{\alpha\alpha} c_{\beta\beta}^*} \\ \overline{c_{\alpha\beta} c_{\alpha\alpha}^*} & \overline{c_{\alpha\beta} c_{\alpha\beta}^*} & \overline{c_{\alpha\beta} c_{\beta\alpha}^*} & \overline{c_{\alpha\beta} c_{\beta\beta}^*} \\ \overline{c_{\beta\alpha} c_{\alpha\alpha}^*} & \overline{c_{\beta\alpha} c_{\alpha\beta}^*} & \overline{c_{\beta\alpha} c_{\beta\alpha}^*} & \overline{c_{\beta\alpha} c_{\beta\beta}^*} \\ \overline{c_{\beta\beta} c_{\alpha\alpha}^*} & \overline{c_{\beta\beta} c_{\alpha\beta}^*} & \overline{c_{\beta\beta} c_{\beta\alpha}^*} & \overline{c_{\beta\beta} c_{\beta\beta}^*} \end{pmatrix} \tag{2.11}$$

It proves to be useful to classify the coherences based on a quantum number called coherence order p_{mn}. It is defined (equation 2.12) as the difference of the z-angular momentum M (in the magnetic field direction) of the connected states.

$$p_{mn} := M_m - M_n \tag{2.12}$$

Coherences connecting states whose total z-angular momentum quantum numbers differ by one are called (±1)-coherences or single quantum coherences. Coherences connecting states whose total z-angular momentum quantum numbers differ by two are called (±2)-coherences or double quantum coherences.

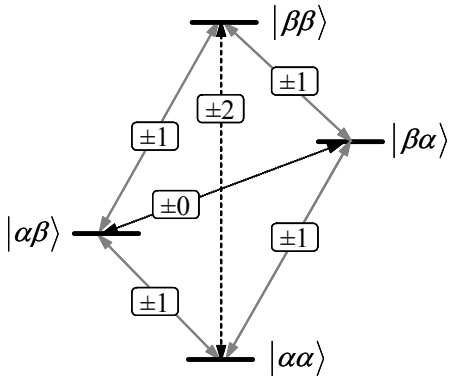

Figure 2.1. The four eigen states of a coupled two spin-½ system with the zero (points), single (grey line), and double quantum (dashed line) transitions shown. Negative transitions point up.

Coherences connecting states with identical total z-angular momentum quantum numbers are called zero quantum coherences. In general, coherences with coherence order different from ±1 are termed multiple quantum coherences (including the zero quantum coherence) and are converted to single quantum coherence prior to detection.

The single quantum coherence is the only one resulting in a transverse magnetization and so the only one directly detected. Once generated, it can be converted into other orders of coherence by the application of radio frequency pulses.

Thus for the system of two coupled spin-½ nuclei (see above) the density operator can be written:

$$\hat{\rho} = \begin{pmatrix} \alpha\alpha & +1 & +1 & +2 \\ -1 & \alpha\beta & +0 & +1 \\ -1 & -0 & \beta\alpha & +1 \\ -2 & -1 & -1 & \beta\beta \end{pmatrix} \tag{2.13}$$

In the matrix, the transitions are represented by elements of opposite sign symmetric about the diagonal. These elements are complex conjugates with the absolute value of the complex number being the amplitude of the coherence and the ratio between the real and imaginary part being related to the phase ϕ (it indicates the direction of the spin polarization in the xy-plane). The sign of the coherence order represents the direction in which the coherence evolves, as shown on Figure 1. For example, the transition from state $|\beta\beta\rangle$ to state $|\alpha\alpha\rangle$ is represented by the (-2)-double quantum coherence $\overline{c_{\beta\beta} c^*_{\alpha\alpha}}$.

The time evolution of the density operator $\hat{\rho}$ is described by the Liouville-von-Neumann equation (2.14), which is the density matrix form of the time dependent Schrödinger equation.

$$\frac{\partial \hat{\rho}}{\partial t} = -i\left[\hat{\mathrm{H}}(t), \hat{\rho}(t)\right]. \tag{2.14}$$

It describes the change of a system over time, which is reflected by the density operator $\hat{\rho}$ and is subject to the Hamiltonian $\hat{\mathrm{H}}$. Hence $\hat{\rho}$ describes the properties of a system, while $\hat{\mathrm{H}}$ all forces acting on it. The Liouville-von-Neumann equation is readily solved when the Hamiltonian is constant with respect to the time t. In the numerical simulations this is achieved as the time is divided in very small periods Δt, so that the Hamiltonian acting on the system is assumed to be approximately constant. In such cases, Δt has to be chosen at least

one order of magnitude smaller than the inverse of the largest interaction present in the system. In its most general form the solution of equation (2.14) reads:

$$\hat{\rho} = \hat{U}(t)\hat{\rho}(0)\hat{U}^{-1}(t) \tag{2.15}$$

where $\hat{U}(t)$ is the so called propagator. For a time-independent Hamiltonian, it writes:

$$\hat{U}(t) = \exp\{-i\hat{\mathrm{H}}t\}. \tag{2.16}$$

2.2. NMR Interactions

As the electric and magnetic fields experienced by the nuclear spin can be external (controlled by the experiment) or due to the sample itself (intrinsic), the nuclear spin Hamiltonian can be presented as a sum the contributing external and local (internal) spin interactions.

$$\hat{\mathrm{H}}_{spin} = \hat{\mathrm{H}}_{ext} + \hat{\mathrm{H}}_{\mathrm{int}} \tag{2.17}$$

The external interactions are magnetic in origin: the Zeeman interaction $\hat{\mathrm{H}}_z$ (the interaction of the spin I≠0 with the static magnetic field B_0) and the spin interaction with the radio frequency (RF) pulses $\hat{\mathrm{H}}_{RF}$. The internal interactions carry information about the environment of the nuclear spin. Described in the order of decreasing strength the internal interations and the related Hamiltonians are:

- the quadrupolar coupling $\hat{\mathrm{H}}_Q$ (the electronic interactions of spin I > ½ nuclei with the surrounding electric fields),
- the dipolar coupling $\hat{\mathrm{H}}_D$ (the dipole-dipole interaction of the nuclear spins with each other *via* their magnetic dipole moments),
- the chemical shift $\hat{\mathrm{H}}_{CS}$ (describes the chemical shift associated with the electronic screening of nuclei, which is generally anisotropic),
- the J-coupling $\hat{\mathrm{H}}_J$ (describes the indirect electron-coupled nuclear spin interactions)

So the nuclear spin Hamiltonian can be presented as a sum of the different terms as follows:

$$\hat{H}_{spin} = \hat{H}_{ext} + \hat{H}_{int} = \left(\hat{H}_Z + \hat{H}_{RF}\right) + \left(\hat{H}_Q + \hat{H}_D + \hat{H}_{CS} + \hat{H}_J\right) \quad (2.18)$$

The present thesis is in part concerned with investigations of the strength of homo- and heteronuclear dipolar couplings between spin-½ nuclei (as well as the related dynamic order parameters as a base for investigating the molecular dynamics) so a more detailed description of those would be presented on the expense of the quadrupolar couplings. Also, due to the low strength and the negligible influence of the J-couplings in the solid state, these are not going to be discussed any further, excluding a brief comparison between dipolar and J-couplings.

2.3. Zeeman Interaction and the Secular Approximation

The Zeeman interaction is the interaction of a nuclear spin ($I \neq 0$) with the external magnetic field B_0. For strong external magnetic fields B the influence of the B_x and B_y components is considered negligible compared to the B_z component. So the magnetic field tensor can be approximated to $B \approx (0, 0, B_z) = B_0$ (assuming that the external magnetic field is longitudinal, i.e. oriented along the z-axis of the laboratory frame). So, only the z component of the corresponding Hamiltonian deviates from zero:

$$\hat{H}_z = -\gamma \hbar B_0 \hat{I}_z \quad (2.19)$$

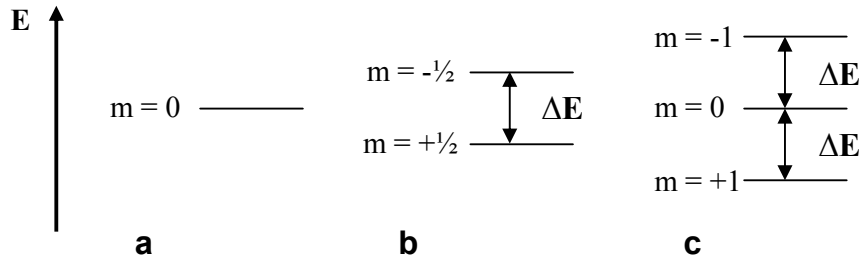

Figure 2.2. Energy level diagram illustrating the breakdown of nuclear spin degeneracy upon the application of a magnetic field for (a) I = 0, (b) I = ½ and (c) I = 1. $\Delta E = \hbar\omega_0 = -\hbar\gamma_j B_0$.

Being the strongest of all spin interactions, the Zeeman interaction causes the splitting of the degenerate (2I+1) energy levels, which are defined by the magnetic nuclear spin quantum number m_I = -I, -I+1, ….+I (Figure 2.2).

The energy of the m^{th} level depends on the type of the spin, characterized by its magnetogeric ratio γ and magnetic quantum number, and on the strength of the applied field B_0 acting on the spin. This dependence is expressed in:

$$E_m = -m\hbar\gamma B_0 \tag{2.20}$$

In the case of a spin-½ nucleus the energy splitting between the two levels is $\Delta E = \hbar\omega_0 = -\hbar\gamma_j B_0$, where ω_0 is the Larmor frequency. So in a sample of non-interacting spin-½ nuclei in a static magnetic field, each spin can exist in one of the two possible eigenstates with a Boltzman distribution over the states at equilibrium. If we consider all the spins in the sample, the z magnetization is given as a sum of all contributions from each possible eigenstate, weighted with the population of the state. This we consider as an ensemble average of the z magnetization.

Under strong external magnetic field the Zeeman interactions exceed (in most of the cases) the other interactions by a large degree. This allows the application of the so called secular (or high-field) approximation, according to which the weaker interactions are treated as perturbations of the Zeeman interaction in the z direction. The Hamiltonians of the internal interactions are divided in two parts; the secular part $\hat{H}'_{int}$ commutes with $\hat{H}_z$, and non-secular part, which does not. Only the secular part contributes to the observable spectrum in first approximation.

The high-field approximation is valid only in cases where the internal interactions are considerably smaller in strength compared to the Zeeman interaction. There are cases of quadrupolar nuclei where the quadrupolar coupling may even exceed the Zeeman interaction.

2.4. Interaction with the RF Pulses

The RF pulses allow for a well defined manipulation of the spin system. During a pulse, the RF coil generates a field B_1 with maximum amplitude A (expressed in units of Tesla) along the x-axis of the laboratory frame. The field, which oscillates at the spectrometer

reference frequency, can be presented as two rotating with the same frequency in opposite directions in the xy-plane components. The component rotating in the same sense as the spin precession (positive for spins with $\gamma<0$, negative for spins with $\gamma>0$) is called resonant component of the RF field and solely affects the motion of the spins. The other non-resonant component is neglected. Mathematically this can be expressed as:

$$B_1(t) = B_1^{res}(t) + B_1^{non\_res}(t) \tag{2.21}$$

The oscillating (with a frequency $\omega_{ref}t$ and initial phase φ) B_1 field may be presented as:

$$B_1(t) = A\cos(\omega_{ref}t + \varphi) \tag{2.22}$$

and so its two components are:

$$B_1^{res}(t) = \frac{1}{2}A\left\{\cos(\omega_{ref}t + \varphi)e_x + \sin(\omega_{ref}t + \varphi)e_y\right\} \tag{2.23}$$

and

$$B_1^{non\_res}(t) = \frac{1}{2}A\left\{\cos(\omega_{ref}t + \varphi)e_x - \sin(\omega_{ref}t + \varphi)e_y\right\} \tag{2.24}$$

Thus, the transverse part of the spin Hamiltonian may be approximated as:

$$\hat{H}^1(t) \cong -\frac{1}{2}\gamma\ A\left\{\cos(\omega_{ref}t + \varphi)\hat{I}_x + \sin(\omega_{ref}t + \varphi)\hat{I}_y\right\} \tag{2.25}$$

where the prefactor $\left| \tfrac{1}{2}\gamma A \right| = \omega_{nut}$ is called nutation frequency and can be considered as a measure of how strongly the RF field influences the resonant spins. The nutation frequency expressed in rad/s ($\omega_{nut}/2\pi$) is in the range 1-200 kHz, i.e. 3-4 orders of magnitude smaller than the Larmor frequency.

In experimental conditions it is the two fields B_0 (the static longitudinal field) and B_1 (the oscillating transverse field) that are to be taken into account when evaluating the effects of a pulse on the spin system. Also, the oscillating B_1 field introduces time dependence in the Hamiltonian describing the system.

$$\hat{\mathrm{H}}(t) = \omega_0 I_z + \hat{\mathrm{H}}_{RF}(t) \tag{2.26}$$

Thus, it is convenient to introduce the rotating reference frame (precessing around B_0 with the Larmor frequency) in which the B_1 field appears static. Using the sandwich relationship[13] and the notation of the rotating frame Hamiltonian, after a substitution of equation 2.25 in equation 2.26, we obtain:

$$\hat{\tilde{\mathrm{H}}} \cong \omega_{nut} \hat{R}_z(\varphi) \hat{I}_x \hat{R}_z(-\varphi) + \Omega_0 \hat{I}_z \tag{2.27}$$

which can also be written as:

$$\hat{\tilde{\mathrm{H}}} \cong \Omega_0 \hat{I}_z + \omega_{nut}(\hat{I}_x \cos\varphi + \hat{I}_y \sin\varphi) \tag{2.28}$$

In equation 2.15, which is the equation of the rotating-frame Hamiltonian during the pulse, with Ω_0 is denoted the resonance offset ($\Omega_0 = \omega_0 - \omega_{ref}$, the difference between the Larmor and reference frequencies). In equation 2.15 the time-dependence has vanished, which is the reason for introducing the rotating frame of references.

2.5. Shielding Anisotropy

In atoms and molecules, the electron clouds surrounding the nuclei locally influence the external magnetic field B_0. The moving electrons create a local (secondary) field, which added to the B_0 field, changes the resonance frequency of the nuclear spins. The interaction originating from the secondary field acting on the nuclei is called shielding interaction and the shift it causes in the NMR spectrum of a nucleus - a chemical shift. The different electrons contribute differently to the secondary, and respectively the overall magnetic field experienced by the nuclei, depending mostly on their distance to the nucleus. The core electrons have a diamagnetic contribution σ_d to the shielding (reduce the B_0 field), which can be calculated using the Lamb formula:

$$\sigma_d = \frac{e^2 \mu_0}{12\pi m_e} \left\langle \frac{1}{r} \right\rangle \tag{2.29}$$

where μ_0 is the vacuum permeability, r – the distance electron nucleus and $\langle 1/r \rangle$ - the expectation value of the respective atom orbital, e and m_e – the charge and mass of the electron respectively.

The local paramagnetic contribution σ_p arises from the ability of the applied field to force electrons to circulate through the molecule by making use of orbitals unoccupied in the ground state. It is said that the magnetic field mixes excited states which possess paramagnetic properties and ground electronic states. The degree of mixing depends on the energy difference between the electron levels and therefore strongly on the temperature. Thus, large paramagnetic contributions are expected for molecules with low-lying excited states.

The chemical shielding Hamiltonian acting on a spin is:

$$\hat{\mathrm{H}}_{CS} = -\gamma \hbar \hat{I} \sigma B_0 \tag{2.30}$$

where σ is the chemical shielding tensor. Obviously, the shielding tensor depends on the orientation of the molecule with respect to the B_0 field. As the electron shielding is not isotropic in space it can be presented as an ellipsoid, (Figure 2.3) fixed within the molecule with a centre the nucleus of interest, rather than a sphere. Therefore, the related second-rank Cartesian tensor (in its 3 x 3 matrix representation) is most conveniently written as:

$$\sigma = \begin{pmatrix} \sigma_{xx} & \sigma_{xy} & \sigma_{xz} \\ \sigma_{yx} & \sigma_{yy} & \sigma_{yz} \\ \sigma_{zx} & \sigma_{zy} & \sigma_{zz} \end{pmatrix} \tag{2.31}$$

It is useful to decompose the shielding tensor to two components – symmetric and antisymetric as follows: $\sigma = \sigma^s + \sigma^{as}$. As only the symmetric part influences the NMR spectrum to any great extent, the antisymetric component may be safely ignored.

In a principal axis frame (PAF) with axes x^{PAF}, y^{PAF}, z^{PAF}, defining σ, the symmetric part of the shielding tensor (henceforth considered only as the shielding tensor), σ is diagonal. The values situated on the diagonal are the principal values of σ_{aa}^{PAF} (σ_{xx}, σ_{yy}, σ_{zz}).

The three principal values are frequently expressed as the isotropic (orientation independent) value σ_{iso}, the anisotropy Δ and the asymmetry η. These quantities are defined as follows:

$$\begin{aligned}\sigma_{iso} &= \frac{1}{3}\left(\sigma_{xx}^{PAF} + \sigma_{yy}^{PAF} + \sigma_{zz}^{PAF}\right) \\ \Delta &= \sigma_{zz}^{PAF} - \sigma_{iso} \\ \eta &= \left(\sigma_{xx}^{PAF} - \sigma_{yy}^{PAF}\right) \Big/ \sigma_{zz}^{PAF}\end{aligned} \tag{2.32}$$

As we consider the z axis of the laboratory frame coinciding with the direction of the B_0 field, then only the zz component σ_{zz} of the tensor will govern the shielding field in the z direction (also the quantization axis for the spins). So the shielding Hamiltonian of equation 2.16 can be written as:

$$\hat{\mathrm{H}}_{CS} = -\gamma\hbar\hat{I}\sigma_{zz}^{LF}B_0 \tag{2.33}$$

Expressing the zz component of the shielding tensor in the LF in terms of its principal values (the two frames being shifted one relative to the other by the polar angles α and β (see Figure 2.3)) we obtain:

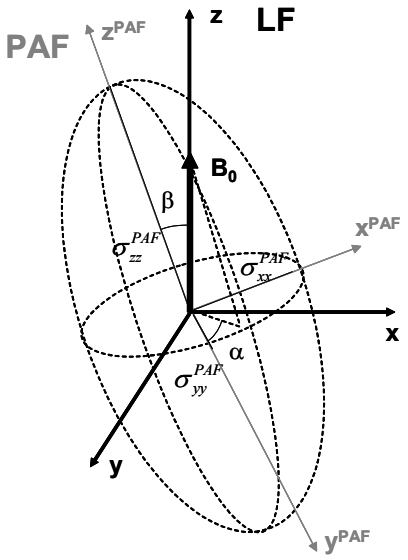

Figure 2.3. The CSA tensor with principal components $\sigma_{xx}^{PAS}, \sigma_{yy}^{PAS}, \sigma_{zz}^{PAS}$ represented as an ellipsoid in the laboratory frame (with axes x, y, z). α and β are the azimuthal and polar angles, respectively, that define the relative orientation of the shielding anisotropy tensor principal axis frame to the laboratory frame.

$$\sigma^{LF} = \sigma_{zz}^{LF} = \sigma_{xx}^{PAF} \sin^2\beta\cos^2\alpha + \sigma_{yy}^{PAF} \sin^2\beta\sin^2\alpha + \sigma_{zz}^{PAF} \cos^2\beta \tag{2.34}$$

For a tensor with axial symmetry ($\sigma_{xx}^{PAF} = \sigma_{yy}^{PAF}$) the equation simplifies to:

$$\sigma^{LF} = \sigma_{zz}^{PAF} \frac{1}{2}\left(3\cos^2\beta - 1\right) \tag{2.35}$$

Using the quantities defined in equation 2.17 we obtain:

$$\sigma^{LF} = \sigma_{iso} + \frac{1}{2}\Delta\left(3\cos^2\beta - 1 + \eta_{CS}\sin^2\beta\cos 2\alpha\right) \tag{2.36}$$

So, the contribution of the electron shielding ω_{CS} (expressed in frequency units) to the overall spectral frequency of a nucleus can be given as:

$$\omega = \omega_0 \pm \omega_{CS}(\alpha,\beta) = \omega_0 \pm \omega_0\sigma^{LF}(\alpha,\beta) = \omega_0\left[1 \pm \sigma^{LF}(\alpha,\beta)\right] \tag{2.37}$$

where ω_0 is the Larmor frequency, which is chemically shifted due to the electron shielding. The sign as well as the size of the shielding contribution depends on the influence of the low-lying electronic excited states, on the inductive effects of the neighbouring nuclei as well as on the influence of the electron density of neighbouring molecules in the solid state (to be discussed in chapter 2.6).

2.6. Chemical Shift

The chemical shift of a given nucleus depends on the type of the nucleus (different nuclei have different electronic shielding) and on the strength of the external magnetic field B_0 (as seen from equation 2.33). If the magnetic field is increased, the chemical shift also increases. To a very good approximation, the chemical shift, measured in frequency units, is linearly proportional to the applied magnetic field.

Since the Larmor frequency and the chemical shift are both proportional to the applied magnetic field, the ratio of these two quantities is fixed. For practical applications, it is convenient to specify chemical shifts in terms of this ratio, since it depends on the sample,

and not on the instrument. The field-independent expression for the chemical shift is as follows:

$$\delta = \frac{\omega^0 - \omega^o_{ref}}{\omega^0_{ref}} \tag{2.38}$$

The chemical shift tensor has elements

$$\delta_{\alpha\beta} = \frac{\sigma_{\alpha\beta}(ref) - \sigma_{\alpha\beta}}{1 - \sigma_{\alpha\beta}} \tag{2.39}$$

where σ_{mn} is the *mn* element of the shielding tensor of the spin of interest in some axis frame and δ_{mn} is the corresponding element of the chemical shift tensor in the same frame. The chemical shift anisotropy and asymmetry are defined analogously to the shielding anisotropy and asymmetry. Often the principal values of the elements are known, but not the axis frame. Then the axis are labelled by convention as $\delta_{11}^{PAF}, \delta_{22}^{PAF}, \delta_{33}^{PAF}$, where $\delta_{11}^{PAF} \geq \delta_{22}^{PAF} \geq \delta_{33}^{PAF}$. From the diagonal elements of this arbitrary frame, as already discussed for the shielding anisotropy, the chemical shift anisotropy and asymmetry can be defined:

$$\begin{aligned} \Delta_{CS} &= \delta_{11}^{PAF} - \delta_{iso} \\ \eta_{CS} &= \frac{\delta_{33}^{PAF} - \delta_{22}^{PAF}}{\delta_{11}^{PAF}} \end{aligned} \tag{2.40}$$

Observed chemical shifts are related to the chemical shift tensor through

$$\delta^{LF}(\alpha,\beta) = \delta_{iso} + \tfrac{1}{2}\Delta_{CS}\left(3\cos^2\beta - 1 + \eta_{CS}\sin^2\beta\cos 2\alpha\right) \tag{2.41}$$

as the isotropic chemical shift is given by:

$$\delta = \frac{\sigma_{iso(ref)} - \sigma_{iso}}{1 - \sigma_{iso(ref)}} \approx \sigma_{iso(ref)} - \sigma_{iso} = 1/3\left(\delta_{11}^{PAF} + \delta_{22}^{PAF} + \delta_{33}^{PAF}\right) \tag{2.42}$$

2.6.1. Influences on the Chemical Shift

The chemical shift variations may have intramolecular contributions (including the electron shielding of a nucleus as a function of the atom number and isotope type, as well as the electronegativity and respectively the inductive effects of neighbouring chemically bonded nuclei) or intermolecular contributions (such as the influence of neighbouring molecules with strong magnetic susceptibility inducing electron ring currents or fast chemical exchange processes between molecules existing in different chemical forms).

2.6.2. Neighbouring Group Contribution

The contribution of a neighbouring group arises from the currents induced in closely situated groups of atoms. In an H-X group (Figure 2.4) the external magnetic field generates currents in the electron distribution of X and induces a magnetic moment proportional to the field. The constant of proportionality is the magnetic susceptibility χ of the group X. If we assume that χ has two components $\chi_{\parallel}$ and $\chi_{\perp}$ (parallel and perpendicular to the axis of symmetry of X) and the axis of symmetry makes an angle θ to the vector connecting X and H, then to a good approximation the shielding constant $\sigma_{neighbour}$ can be given as:

$$\sigma_{neighbour} \propto \left(\chi_{II} - \chi_{\perp}\right)\left(\frac{1-3\cos^2\theta}{r^3}\right) \qquad (2.43)$$

where both $\chi_{\parallel}$ and $\chi_{\perp}$ are negative for diamagnetic group X and r is the distance between H and X. As seen from equation 2.29 and Figure 2.4 $\sigma_{neighbour}$ can be positive or negative depending on the magnitudes of $\chi_{\parallel}$ and $\chi_{\perp}$ and the relative orientation of H to X. The latter effect can be easily anticipated: if $54.7° < \theta < 125.3°$, then $1-3\cos^2\theta$ is positive, but negative otherwise.

Rigid molecules with well-defined three-dimensional structures that experience the shielding effect of the e^- density of neighbouring (in most cases large aromatic) systems are an example for this phenomenon. This is particularly true for columnar systems, where due to packing effects chemically identical nuclei from neighbouring disc may have different electronic environment and thus have different chemical shifts. This effect is due to the

strong anisotropy of the magnetic susceptibility of the aromatic ring, which results in the ability of the external field, applied perpendicular to the molecular plain, to induce a ring current (a circulation of the electron density above and below the plane of the ring).

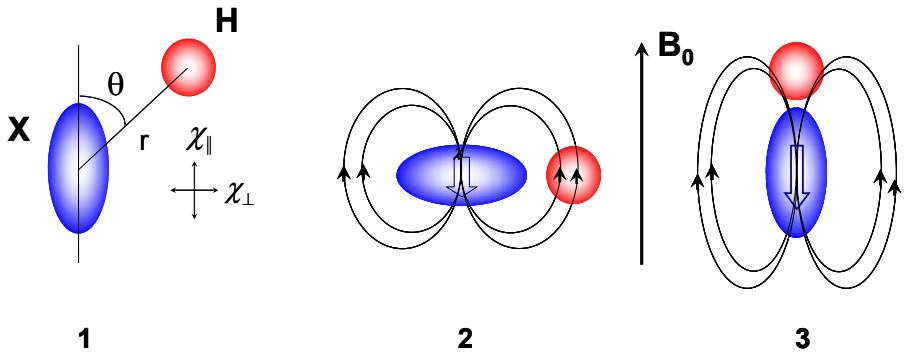

Figure 2.4 A tumbling (all anisotropic interactions are averaged) H-X molecule in external magnetic field, where $\chi_{\parallel}$ and $\chi_{\perp}$ are the components of the magnetic susceptibility of X

In this case, the nuclei (commonly observed for protons) situated in the ring plain are deshielded, while nuclei above and below are shielded. Such effect is typically found in the solid state, where molecules or molecular segments containing aromatic rings have fixed orientation and are closely situated. Ring currents are also observed in solutions, if the solvent is an aromatic molecule. The so-called NICS (nucleus-independent chemical shift) maps can conveniently visualize the shielding-deshielding effects.

2.6.3. Influence (Inductive effects) of the Electronegative Neighbouring Nuclei

The chemical shift also correlates strongly with the electronegativity of neighbouring groups, such as O, Cl, and F. These tend to withdraw electron density, increasing the field experienced by the neighbouring nuclei. Thus, the resonance frequency of such nuclei is shifted towards higher frequencies. This is of particular interest for N...H-O and O...H-O hydrogen bonds, where the ^{1}H chemical shift is influenced by the presence of two electronegative neighbouring sites. The degree to which these withdraw electron density and increase the chemical shift (as value) is approximately proportional to the hydrogen bond length N...H/O...H. This leads to relatively high proton chemical shifts of between 6–13 ppm and are thus an important handle on hydrogen-bonding in the solid-state.

2.7. Dipole-dipole Couplings

The classical picture of two interacting nuclei of magnetic moments μ_I and μ_S is illustrated in Figure 2.5 a. In each other's magnetic field, the spins acquire a magnetic energy

$$E = \frac{\mu_0}{4\pi}\left(\frac{\mu_I.\mu_S}{r^3} - 3\frac{(\mu_I.r)(\mu_S.r)}{r^5}\right) \tag{2.44}$$

Quantum mechanically, the magnetic moment operator $\hat{\mu}$ for the spin I, is given by:

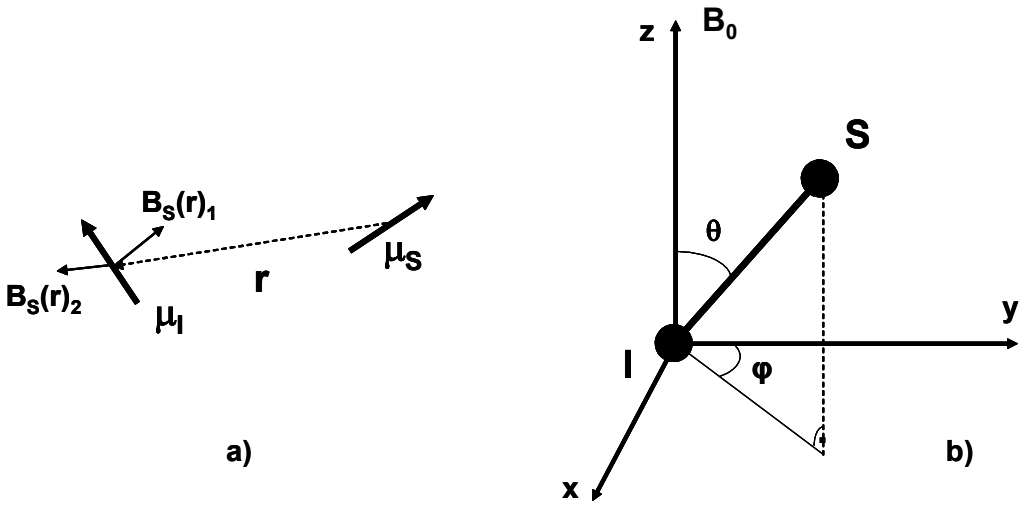

Figure 2.5 a) The interaction between two magnetic dipoles. The local field at the site of μ_I due to the presence of μ_J has two components: one in the direction of μ_S **($B_S(r)$**1) and the other one in the direction of the internuclear vector, r, **($B_S(r)_2$**). For the sake of simplicity, the local field created by μ_I at the site of μ_S is not shown.
b) Definition of the polar angles θ and φ specifying the orientation of the I-S internuclear vector in respect to the B_0 field (along the z axis of the laboratory frame).

$$\hat{\mu} = \gamma\hbar\hat{I} \tag{2.45}$$

Substituting 2.45 in equation 2.44, we obtain the interaction Hamiltonian for the dipolar coupling between two spins I and S in angular frequency units (rad/s):

$$\hat{H}_D = -\left(\frac{\mu_0}{4\pi}\right)\gamma_I\gamma_S\hbar\left(\frac{\hat{I}^I.\hat{I}^S}{r^3} - 3\frac{\left(\hat{I}^I.r\right)\left(\hat{I}^S.r\right)}{r^5}\right) \tag{2.46}$$

Expressing equation 2.18 in polar coordinates and after elimination of the terms that do not commute with the Zeeman Hamiltonian, we obtain a product characterized by spatial and spin terms:

$$\begin{aligned}\hat{H}_D^{IS} &= -D_{IS}\frac{1}{2}\left(3\cos^2\theta_{IS}-1\right)\left[2\hat{I}_z^I\hat{I}_z^S-\left(\hat{I}_+^I\hat{I}_-^S+\hat{I}_-^I\hat{I}_+^S\right)\right]= \\ &= -D_{IS}\frac{1}{2}\left(3\cos^2\theta_{IS}-1\right)\left[2\hat{I}_z^I\hat{I}_z^S-\hat{I}_x^I\hat{I}_x^S-\hat{I}_y^I\hat{I}_y^S\right]= \\ &= -D_{IS}\frac{1}{2}\left(3\cos^2\theta_{IS}-1\right)\left[3\hat{I}_z^I\hat{I}_z^S-\hat{I}^I\hat{I}^S\right]\end{aligned} \tag{2.47}$$

The terms $\hat{I}_+^I,\hat{I}_-^I,\hat{I}_+^S,\hat{I}_-^S$ are the corresponding raising and lowering operators ($\hat{I}_+=\hat{I}_x+i\hat{I}_y$ and $\hat{I}_-=\hat{I}_x-i\hat{I}_y$), θ_{IS} is the angle between the external magnetic field and the internuclear vector and D_{IS} is the dipolar coupling constant:

$$D_{IS}=\frac{\mu_0}{4\pi}\frac{\gamma_I\gamma_S\hbar}{r_{IS}^3} \tag{2.48}$$

The Hamiltonian operator describing the homonuclear dipolar spin interaction (here with I and S we denote the same type spin-½ nuclei) is given by equation 2.19.
In the case of a dipolar coupled heteronuclear I-S spin-½ pair, the flip-flop term is no longer energy conserving and is eliminated by the secular approximation, leading to a truncated Hamiltonian

$$\hat{\mathrm{H}}_{hetero}^{IS}=-\frac{1}{2}D_{IS}(\cos^2\theta_{IS}-1)2\hat{I}_z^I\hat{I}_z^S \tag{2.49}$$

For a homo- and heteronuclear spin pairs the splitting depends on the nature of the nuclei and the polar angle θ via the relations:

$$\nu_{\mathrm{hom}}=\nu_0\pm\frac{3D_{II}}{4}\left(3\cos^2\theta_{II}-1\right) \tag{2.50}$$

and

$$\nu_{hetero} = \nu_0 \pm \frac{3D_{IS}}{2}\left(3\cos^2\theta_{IS} - 1\right) \tag{2.51}$$

where with I and S we denote different spin-½ nuclei and ν_0 is the isotropic chemical shift in frequency units.

2.8. Comparison between Dipole-dipole and J-couplings

Dipole-dipole interaction between the nuclear spins significantly influences the spectral line shapes. In general, there are two types of such spin-spin interactions, namely the direct coupling between spins (dipolar coupling) and the indirect coupling via mediating (covalent bond) electrons (J-coupling). Obviously, the dipolar couplings can be either intra- or intermolecular, while the J-couplings exist only between nuclei of the same molecule. In addition, the dipolar coupling (with strength in the kHz range) is orientation dependent (and so anisotropic) and can be reduced or completely averaged by molecular motion. At the same time the J-coupling (or scalar coupling) is an isotropic interaction three orders of magnitude weaker compared to the dipolar coupling of a static pair and thus not influenced by the molecular motion. This feature makes the J-coupling a powerful tool in solution-state NMR, where information about bonded neighbours can be obtained. In solid-state NMR, on the other hand, the J-coupling is usually obscured by the direct dipole-dipole interaction and is much less relevant than in solution-state. In the following, the discussion will be restricted to the direct through-space dipole-dipole interaction.

2.9. Magic Angle Spinning

In solution the fast isotropic molecular tumbling leads to a complete averaging of the anisotropic (orientation dependent interactions, represented by the respective terms in the Hamiltonians describing the interaction), leaving only the scalar couplings and the isotropic chemical shift. In the solid state, the motion, if at all, is on a much slower timescale, so the dipole-dipole couplings and the CSA dominate the static spectrum of spin-½ nuclei. Thus it is possible to have two cases – an isolated spin (a narrow spectral line occurs at the resonance frequency; the frequency of the signal depends on the orientation of the shielding tensor in respect to the applied field) and a coupled spin pair (a well defined and orientation dependent

splitting occurs in the spectrum). As in powders all molecular orientations are present with equal probability, the static NMR spectrum is inhomogeneously broadened.

There have been proposed different approaches to record high-resolution NMR spectra in the solid state.

One approach relies on uniaxial sample orientation either mechanically (typically by extrusion, which can be done also directly in the rotor[14]) or via cooling the melt in a magnetic field for stationary samples[15]. In this case, the uniaxial orientation leads to line narrowing, yet the anisotropic interactions inherent for the spins are preserved.

Another approach, the so called "multiple pulse line narrowing", uses radio frequency pulses on the spins of interest, acting on the spin part of the wavefunction, thus averaging the spin term of the dipolar Hamiltonian (equation 2.46) to zero.

Recently, an approach[16,17] for improving the spectral resolution by using rotating magnetic fields has been proposed. However, further development is needed before such an idea is successfully implemented in a commercial product.

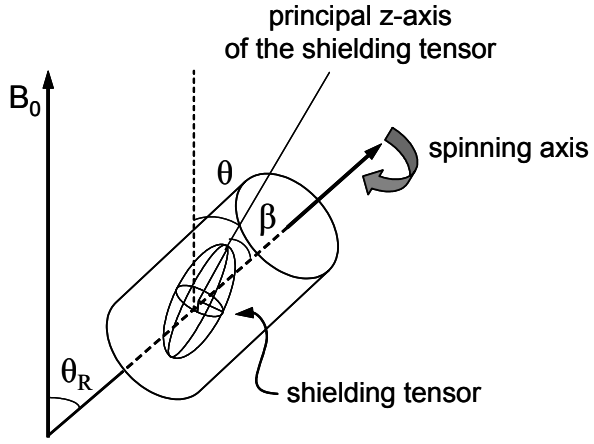

Figure 2.6 The magic angle spinning experiment. The sample is spun about an axis oriented at the magic angle (54.74°) with respect to the applied field B_0. The shielding tensor is represented by an ellipsoid fixed in the molecule to which it applies. θ, θ_R and β are respectively the angles between the B_0 and the principal axis of the shielding tenor, between the rotor (spinning) axis and B_0 and between the principal z-axis of the shielding tensor PAF and the rotor axis

The most widely used technique for line narrowing in solid state NMR spectroscopy is the so-called magic angle spinning[5,6] (Figure 2.6). MAS increases the spectral resolution by a fast mechanical rotation of the sample about an axis inclined at the magic angle (54.7° -

also defined as the angle between the edge of a cube and its body diagonal) in respect to the external magnetic field. MAS is routinely used to gain spectral resolution on the expense of removal the CSA contribution, as well as to assist in the removal of dipolar couplings. In addition, it is used to narrow the lines from quadrupolar nuclei and is increasingly the method of choice for averaging out the effects of the homonuclear dipole-dipole couplings.

The technique achieves similar results as fast isotropic molecular tumbling in solution, where the molecular orientations are rapidly changing and thus the angle θ (or in general the angles describing the orientation of the shielding/dipolar tensor with respect to the applied field) are taking rapidly all possible values and are thus averaged. This averages the $(3\cos^2\theta-1)$ dependence of the dipole-dipole couplings (equation 2.47) and shielding anisotropy (equation 2.35) to zero on the NMR timescale. The MAS mechanism of achieving line narrowing is, however, different. So if we consider a sample in a rotor spinning fast about the rotor axis and inclined at the angle θ_R in respect to the external field B_0 (Figure 2.6), then the orientation of the interaction tensor (depending on the angle θ) fixed in a molecule within the sample, varies with time as the sample and respectively the molecule rotates. Then the average of $<3\cos^2\theta-1>$ is:

$$\left\langle 3\cos^2\theta - 1 \right\rangle = \left(3\cos^2\theta_R - 1\right)\left(3\cos^2\beta - 1\right) \qquad (2.52)$$

where the angles θ, θ_R and β are the angles between B_0 and the principal axis of the shielding tenor, between the rotor (spinning) axis and B_0 and between the principal z-axis of the shielding tensor PAF and the rotor axis. The angle β is fixed for a given nucleus in a rigid solid. In a powder sample under rotation the angle θ takes all possible values. Therefore, if θ_R (which is under the experimental control) is set to 54.7° then the whole equation 2.52 equals to zero. So, if sufficiently fast spinning is applied, θ is averaged rapidly compared with the anisotropy of the interaction, i.e. the interaction anisotropy averages to zero. However, if the spinning is not sufficiently fast compared to the anisotropy of the interaction being spun out ("fast" meaning 3-4 times greater than the anisotropy), spinning sidebands appear in addition to the signal of the isotropic chemical shift. The sidebands are sharp lines set at the spinning frequency apart from the isotropic shift line, as the latter is the only line that does not change its position at different spinning speeds, but not necessarily the most intense one.

2.10. Hamiltonians under MAS

As discussed in the previous section the spectral representation of slow sample spinning is the appearance of sidebands due to the incomplete averaging of the CSA and the dipolar couplings. In addition, time dependence is imposed on the interaction Hamiltonians $\hat{H}_\lambda$ that leads to the inapplicability of the average Hamiltonian theory in such cases. However, only the space parts of the Hamiltonian gain time dependence under spinning, hence the Hamiltonian still commutes with itself. Thus, the zeroth-order average Hamiltonian in the secular approximation describing the evolution under an interaction λ and sample rotation for arbitrary times is written as:

$$\bar{\hat{H}}_{\lambda,MAS}(t) = \frac{1}{t}\int_0^t \hat{H}_\lambda(t)dt = \hat{T}_{00}A_{00}^{\lambda,LAB} + \hat{T}_{20}\frac{1}{t}\int_o^t tA_{20}^{\lambda,LAB}(\omega_R t)dt \qquad (2.53)$$

The explicit calculation of the average Hamiltonian requires the knowledge of the space part of the interaction in the laboratory frame A_{20}^{LAB}. In general, three Euler angle transformations (from the principal axis frame (PAS) to the molecular frame (MF); from the MF to the rotor frame (RF); and from RF to the laboratory frame (LF)) are necessary to transform an interaction tensor, usually defined in its PAF, to the LF:

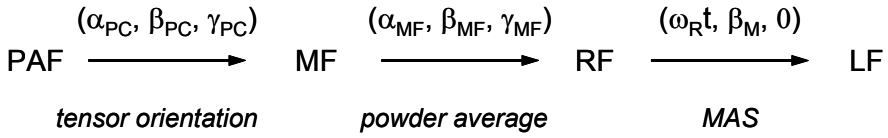

The only time dependent angle ($\omega_R t$) is in the last transformation from the rotor frame to the laboratory frame. The three independent transformations are needed if more than one interaction is to be considered, i.e. when relative orientations of different tensors are to be specified. Otherwise, a direct transformation from the PAF to the rotor frame is possible.

For the case of a single dipole-dipole coupled spin pair the time-dependent average Hamiltonian is:

$$H_{D,MAS}^{ij}(t) = \frac{3}{2}\Phi_{D_{ij}}(t)2\sqrt{\frac{2}{3}}T_{20}^{(ij)}\frac{1}{t}, \qquad (2.54)$$

for a coupled homonuclear spin-½ pair, and

$$\mathrm{H}^{ij}_{D,MAS}(t) = \Phi_{D_{ij}}(t) 2\hat{I}_z\hat{S}_z \frac{1}{t} \tag{2.55}$$

for a heteronuclear spin pair, where

$$\Phi_{D_{ij}}(t) = \frac{D_{ij}}{\omega_R}\frac{1}{\sqrt{2}}\sin 2\beta\{\sin(\gamma+\omega_R t)-\sin\gamma\} - \frac{D_{ij}}{\omega_R}\frac{1}{4}\sin^2\beta\{\sin(2\gamma+2\omega_R t)-\sin 2\gamma\} \tag{2.56}$$

If we consider the time evolution (or the phase acquired in the course of time) of the interaction tensors having an initial state $\hat{\rho}(0) = \hat{I}_x$ under the influence of the magic angle spinning we can write:

$$\hat{I}_x \xrightarrow{\bar{H}_{\lambda,MAS(t)}t} \hat{I}_x \cos\Phi_\lambda + \hat{W}\sin\Phi_\lambda \text{, where} \tag{2.57}$$

$$\Phi_{CSA} = \omega_{iso}t + \Phi_{CS}, \hat{W} = \hat{I}_y \tag{2.58}$$

$$\Phi_{\mathrm{hom},dip} = \frac{3}{2}\Phi_{D_{ij}}, \hat{I}_x = \hat{I}^{(i)}_x + \hat{I}^{(j)}_x, \hat{W} = 2\left(\hat{I}^{(i)}_y\hat{I}^{(j)}_z + \hat{I}^{(j)}_y\hat{I}^{(i)}_z\right) \tag{2.59}$$

$$\Phi_{het,dip} = \Phi_{D_{ij}}, \hat{W} = 2\hat{I}_y\hat{S}_z \tag{2.60}$$

The acquired phase angles Φ_λ are on one hand time-dependent, and on the other functions on the Euler angles (α, β, γ), transforming the interaction tensor from the principal axis frame to the rotor frame. While (α, β) are identical to the polar angles (θ, β) of the rotor axis in the PAF and the time-dependence on α is valid only for non-axially symmetric interaction tensors, γ describes the initial rotor phase, as seen from equation 2.55. The time dependence is presented (equation 2.56) as trigonometric functions of $\omega_R t$ and $2\,\omega_R t$ and can be considered simply as a rotor modulation of the Hamiltonian.

2.11. Spinning-Sideband Patterns

The anisotropic interactions (dipole-dipole couplings and CSA) are periodic in respect to the rotor period ($\tau_R = 1/\omega_R$) under magic angle spinning conditions. Also, the sin and cos

dependence of the signals periodic to $\omega_R t$ and $2\,\omega_R t$ (equation 2.57) leads to the appearance of spectral components oscillating at integer multiples of the τ_R. The latter components after Fourier transformation show up in the spectra as signals spaced by ($\pm n\omega_R$).

The sideband manifold in the time domain can be presented as:

$$S_{MAS}(t) = \left\langle \sum_{n=-\infty}^{\infty} \xi_n e^{in\omega_R t} \right\rangle = \sum_{n=-\infty}^{\infty} \bar{\xi}_n e^{in\omega_R t} \tag{2.61}$$

where the sidebands intensity is given as an average of the integrals over one rotor period of the oscillating signal arising from the respective anisotropic interaction.

$$\bar{\xi}_n = \frac{1}{\tau_R} \left\langle \int_0^{\tau_R} S_{MAS}(t) e^{-in\omega_R t}\, dt \right\rangle \tag{2.62}$$

In the case of CSA, the graphic representations of the calculated intensity ratios $\bar{\xi}_{\pm n} / \bar{\xi}_0$ can be used to determine the tensor parameters δ and η from the sideband patterns in the MAS NMR spectra (one has to take into account also the need for high power proton decoupling necessary to leave CSA the dominating interaction in "real" spectra). In addition, CSA can serve as an example for an interaction where the anisotropic broadening is refocused at the end of each rotor period τ_R, i.e. the corresponding Hamiltonian commutes with itself at all times.

Maricq and Waugh, referring to the effect of MAS on the anisotropic interactions distinguish between "homogeneous" and "inhomogeneous" interactions[18]: under MAS an "inhomogeneously" broadened line (as in the case of CSA or heteronuclear ^1H-^{13}C dipole-dipole coupling) splits spontaneously into a pattern of sharp sidebands, while "homogeneously" broadened lines successively narrow with increasing the MAS frequencies. The reason for the latter observation is that in cases of three or more coupled protons, the perturbing influence of the other dipolar coupled spins upon a finite dipolar coupled pair means that the dipolar Hamiltonian no longer commutes with itself at all times. Respectively, the evolution of a dipolar coupling is no longer refocused at the end of a rotor period.

Thus, spinning speeds in the range of at least 5-10 kHz are needed to observe the initial splitting into spinning sidebands (still with appreciable line width) of the otherwise

broad and featureless static ^{1}H NMR spectrum. To average the coupling effect of the network of strongly coupled ^{1}H spins (where the effect of the multiple couplings significantly exceeds the coupling of an individual spin pair) very high spinning speeds are required. The application of such speeds would contribute to the increase in the spin-pair character of the proton network, i.e. in isolated pairs the interaction is refocusable over a τ_R[19].

Finally, for the case of a heterospin, S, coupled to a multitude of I-spins (and neglecting the homonuclear couplings between these), the time evolution of the S-spin is inhomogeneous, as the heteronuclear couplings commute: $\left[\hat{I}_z^{(i)}\hat{S}_z, \hat{I}_z^{(j)}\hat{S}_z\right] = 0$.

Further in the thesis, the application of spinning sidebands analysis to determine the details of homo- and heteronuclear dipole-dipole couplings under fast or moderate magic angle spinning conditions will be discussed. Based on the values of the experimentally determined (effective) coupling constants the site-specific molecular dynamics will be determined and discussed in terms of angular distributions of mobilities. It should be noted that the mechanism of recording sideband patterns in the case of incrementing the evolution period between two recoupling blocks of pulses is reconversion rotor encoding (RRE), e.g. different from the one (evolution rotor modulation – ERM) described above.

Chapter 3. Recoupling Techniques under MAS

As discussed in the previous chapter any wavefunction describing the state of a spin system can be divided in space and spin part. While the magic angle spinning influences the space part of the wavefunction averaging the anisotropic interactions, RF pulses act on the spin part. Using special pulse sequences, it is possible to selectively reintroduce one of the averaged anisotropic interactions. The technique is termed recoupling and the respective pulse sequences - recoupling pulse sequences.

3.1. Multiple-quantum techniques

Before introducing the concepts of recoupling, it is useful to discuss the so called multiple-quantum techniques. Such experiments are applied for the excitation of multiple-quantum coherences. As presented in the previous chapter an m-quantum coherence is related to a transition between states with a difference in the total z-angular momentum ± m, i.e. the overall magnetic spin quantum number M is changed by m. In the spherical tensor notation a MQ coherence of order m, involving L spin-½ nuclei (L≥m), can be presented as a tensor operator of rank L and order m, $\hat{T}_{L\pm m}$. In unperturbed system, transitions with ΔM>1 are forbidden. Under the influence of a perturbing interaction like the dipole-dipole coupling, these transitions become weakly allowed. Since MQ coherences are not directly detected, they have to be converted to single-quantum coherence prior to detection. Therefore, experiments that monitor the evolution of a MQ coherence are inherently at least two dimensional. A typical MQ experiment consists of four stages (Figure 3.1). During the excitation period a suitable pulse sequence is applied to excite the desired MQ coherence; the whole period being described by an average Hamiltonian $\bar{\hat{H}}_{exc}$. The excited MQ coherence evolves during the period t_1. During the reconversion period, described by the average Hamiltonian $\bar{\hat{H}}_{rec}$, the MQ coherence is converted again to z-magnetization, which is finally detected (after a possible z-filter with a duration t_z) by a 90° “read” pulse. In most of the experiments conducted on different columnar systems discussed in this thesis, the aim was to excite and reconvert double-quantum coherences. Appropriate phase cycling scheme is used to select the latter.

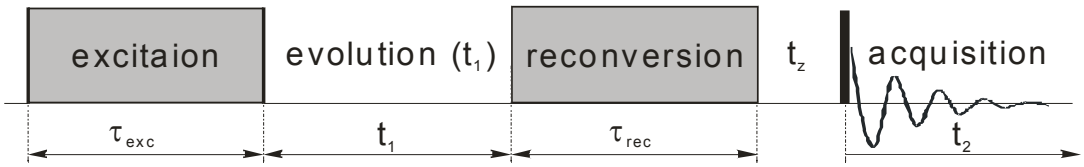

Figure 3.1 Basic structure of a multiple-quantum experiment

If sign discrimination in the indirect dimension is desired, a phase cycling of a part of the pulse sequence with respect to the indirect dimension has to be implemented in such a way that for subsequent time increments (slices) in t_1, the amplitude modulation is only due to the sine- or cosine-component of the indirectly detected signal. The methods used in the experiments described herein are TPPI[20] (time proportional phase incrementation) and States-TPPI[21]. Both methods use 45° phase incrementation of the excitation pulses after recording each t_1 point in the indirect dimension. In TPPI, the cosine- and sine-signal components (representing respectively the real and imaginary parts of a data point) are detected alternating from slice to slice. Thus, two slices are needed to record one data point in the indirect dimension. Therefore, the spectral width in the indirect dimension is divided by two – SW (F_1)=1/(2Δt), (where Δt is the time, between two consecutive increments).

Limiting the MQ order, or respectively the number of coupled spin-½ nuclei to two, results in the so-called double-quantum (DQ) spectroscopy and allows the site-specific (in terms of chemical shift) analysis of dipolar couplings.

3.2. The principle of recoupling

The need for spectral resolution turns the MAS technique into an extremely useful mean to gain such. However, the significantly improved resolution comes at the price of a loss of the information inherent to the anisotropic interactions. Therefore, the development of methods allowing to selectively regain the information about tensor orientation (CSA and DD couplings) and distances between the coupled nuclei (DD couplings), needed for the structure elucidation, is obvious and justified.

Initially, the approaches applied to tackle with this problem, relied either on a fine balance between spinning speed and spectral resolution (slow MAS), or the precise setting (even better to say precise mis-setting) of the 54.7° angle (off-magic angle spinning - OMAS). The former approaches sacrificed part of the resolution gained by the MAS on account of preserving the anisotropic information. In addition, they benefit from the relatively

high sample amounts measured, as the slow ($0<\omega_R<\omega_{CSA}$) spinning speeds in the range of 3-6 kHz allow the use of 4 mm or even 7 mm rotors. At these conditions, the isotropic shift is flanked by rotational sidebands at multiples of the spinning frequency ω_R. The analysis of the intensities of the MAS sidebands provides information about the CSA tensor[22]. The latter approach, the so called OMAS, utilizes fast sample spinning at an angle slightly different from the magic angle to scale down the anisotropic part of the interaction, so that the broad anisotropic line shape is decreased[23,24].

The concept of recoupling preserving the spectral resolution and at the same time regaining information about the anisotropic tensor was introduced by Gullion[25] and developed further by Carravetta[26]. The idea is to apply RF pulses to induce a rotation in the spin part contrary to the rotation in the space part achieved by the MAS. Depending on the length of the applied pulses, the recoupling experiments can be divided in two types: laboratory frame pulse sequences, using short rotor-synchronized high power pulses (the pulses are assumed to be δ-pulses to calculate the average Hamiltonian of the sequence) and the other type, applying long continuous pulses. The latter are also called tilted rotating frame sequences[27,28], as the B_1 field makes the irradiated spins precess with a frequency, which is matched to multiples of the MAS frequency. These experiments are very sensitive towards imperfections in terms of stable power levels and thus technically more demanding compared to the laboratory frame sequences.

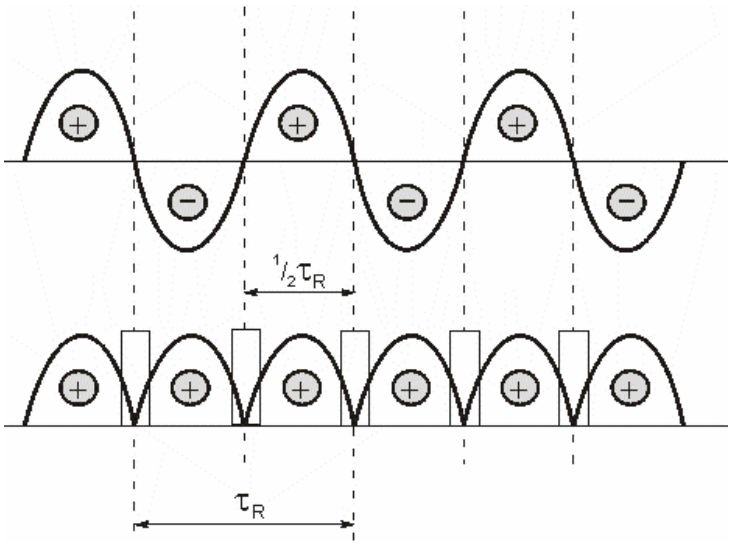

Figure 3.2 Principles of recoupling by rotor-synchronized π-pulse trains

The REDOR (rotational echo double resonance) experiment introduced by Schaefer and Gullion[6,29] belongs to the laboratory recoupling sequences and provides the basis for the recoupling experiments described in the following. It utilizes rotor-synchronized pulse trains with pulses spaced by exactly half a rotor period (the so-called REDOR π-pulse trains) to recouple the anisotropic part of any interaction linear in the irradiated spin. The schematic representation of the effect of the magic angle spinning and the recoupling procedure by π-pulse train is depicted in Figure 3.1.

The average Hamiltonian of the interaction λ (only dipole-dipole couplings are discussed in the thesis, however this is valid for CSA as well) under MAS is given by the sum of first (isotropic) and second (anisotropic) terms contributions.

$$\hat{\bar{H}}_{\lambda,MAS} = \hat{T}_{00} A_{00}^{\lambda,LAB} + \hat{T}_{20} \frac{1}{t}\sqrt{\frac{3}{2}}\Phi_{\lambda} \qquad (3.1)$$

The magic angle spinning modulates the anisotropic term of the Hamiltonian, which process is expressed in the acquired phase, $\Phi_{\lambda}(t)$, whose time-dependence is given in Figure 3.1. Over a full rotor period, the phase $\Phi_{\lambda}(t)$ is equal to zero, and respectively, the anisotropic term of the interaction Hamiltonian under fast MAS is equal to zero. This is the origin of the averaging effect of the magic angle spinning, which is illustrated graphically in the upper part of the figure. The sine-modulation of the anisotropic term of the interaction is schematically presented by the positive and negative lobes of the function, where the half rotor period contributions cancel each other for a full rotor period. The recoupling is effectively achieved by inverting the sign of the anisotropic part of the interaction every second $\tau_R/2$ interval by the application of 180° RF-pulses. This rotation affects the isotropic (spin) part $\hat{T}_{20}$ of the interaction Hamiltonian and is practically a "counter-rotation" to the MAS rotation. Thus, the contributions from every half-rotor period sum up (schematically depicted by the positive lobes in the lower part of the figure) and lead to recoupling/reintroduction of the anisotropic interaction. The sign inversion by π pulses is possible in the cases of CSA and heteronuclear dipole-dipole couplings, as those are interactions linear in the irradiated spin. However, for recoupling the homonuclear dipolar couplings (bilinear in the same type of spin) another approach is applied, namely the back-to-back (BaBa) sequence[30], described in more details in section 3.4.

In the BaBa sequence the 180° REDOR pulse train is replaced by a pair of 90° pulses with orthogonal phases. In this way, a time reversal of the anisotropic (spin) term in the homonuclear dipolar Hamiltonian is achieved every second half of each rotor period, leading to recoupling of the homonuclear dipolar couplings.

3.3. Heteronuclear dipolar recoupling based on the REDOR pulse sequence

The REDOR pulse sequence serves as basis for the heteronuclear (^{13}C-^{1}H) recoupling techniques used in this thesis. Such approaches, with detection on the carbon channel, benefits from the *ca.* 10 times higher spectral width and respectively better chemical shift resolution of the ^{13}C nuclei (as well as in the cases of most of the heteronuclei) compared to the ^{1}H methods. The significantly higher resolution is of prime importance in the solid state NMR experiments on complex supramolecular systems (where solid state effects are also to be considered) for the unambiguous assignment of the resonances of interest. An additional obligatory requirement for successfully conducting the experiments (in rigid samples) is the efficient homonuclear decoupling, which is achieved by very fast (> 25 kHz) magic angle spinning. In mobile systems, where molecular motion reduces the couplings, this requirement is not crucial.

Initially introduced as a triple resonance technique for recoupling the heteronuclear dipolar couplings between low natural abundance,[6] low gamma-nuclei, REDOR can also be used to recouple heteronuclear couplings including a nucleus with spin > ½[31] or ^{1}H-X (where X is a heteronucleus) couplings. Before discussing the particular experiments, the average Hamiltonian under a REDOR type π-pulse train needs to be considered. Starting from initial proton transverse magnetization, the evolution over one rotor period of the recoupling π pulse train reads as

$$\hat{I}_x \xrightarrow{\Phi 2\hat{I}_z\hat{S}_z} \hat{I}_x \cos\Phi + 2\hat{I}_y\hat{S}_z \sin\Phi \tag{3.2}$$

$$\xrightarrow{\pi\hat{S}_x} \hat{I}_x \cos\Phi - 2\hat{I}_y\hat{S}_z \sin\Phi \tag{3.3}$$

$$\xrightarrow{\Phi_1 2\hat{I}_x\hat{S}_z} \hat{I}_x(\cos\Phi\cos\Phi_1 + \sin\Phi\sin\Phi_1) - 2\hat{I}_y\hat{S}_z(\sin\Phi\cos\Phi_1 - \cos\Phi\sin\Phi_1)$$

$$\overset{\Phi=-\Phi_1}{=} \hat{I}_x \cos 2\Phi - 2\hat{I}_y\hat{S}_z \sin 2\Phi \tag{3.4}$$

$$\xrightarrow{\pi\hat{S}_y} \hat{I}_x \cos 2\Phi + 2\hat{I}_y\hat{S}_z \sin 2\Phi \tag{3.5}$$

The second π pulse in equation (3.5) needs to be included in order to describe a full cycle, i.e. one rotor period of the recoupling π pulse train. In equation (3.4) with $\Phi = -\Phi_{D_{IS}}(0;\tau_R/2)$ and respectively $\Phi = -\Phi_{D_{IS}}(\tau_R/2;\tau_R)$ are denoted the phases acquired during the first and second half of a rotor period and the equality $\Phi_1 = -\Phi$ corresponds to the effective inversion of the space part of the Hamiltonian by MAS.

Comparing the equations (3.2) and (3.5) shows that dipolar evolution over one rotor period of the recoupling π pulse train can be described by an average Hamiltonian,

$$\bar{\hat{\mathrm{H}}}_{IS} = \Phi 2\hat{I}_z\hat{S}_z\frac{1}{\tau_R}, \text{ where} \tag{3.6}$$

$$\bar{\Phi} = 2\Phi = -2\Phi_{D_{IS}}(0;\tau_R/2) = \frac{D_{IS}}{\omega_R}2\sqrt{2}\sin 2\beta\sin\gamma \tag{3.7}$$

Thus the evolution over a pulse train of N rotor periods length is given by

$$\hat{I}_x \xrightarrow{\bar{\hat{\mathrm{H}}}_{IS}N\tau_R} \hat{I}_x\cos(N\bar{\Phi}) + 2\hat{I}_y\hat{S}_z\sin(N\bar{\Phi}) \tag{3.8}$$

The REDOR recoupling technique is very robust in respect to pulse imperfections, chemical-shift anisotropy and offsets. The reason is that applying π pulses with arbitrary phases on any of the channels does not influence the average Hamiltonian. Although different phase cycling schemes have been proposed for the sequence[32], the (xy-4) is particularly useful and therefore is applied in all experiments presented here.

The heteronuclear recoupling experiments presented in the following possess the characteristic four stages of a multiple quantum experiment. In all experiments, the spectral resolution in the direct dimension is achieved on account of the *ca.* 200 ppm chemical shift width of the ^{13}C spectrum. Experiments with inverse detection, i.e. on the proton channel, have not been performed. The excitation and reconversion of the dipolar interaction here is achieved by π pulse trains, typically intersected by the evolution time t_1. The first π pulse train (according to equation 3.8) results in a cosine-modulated evolution of the initial coherence and a sine-modulated antiphase coherence. To investigate the evolution of the coherence state, created at the end of the excitation period, the t_1 period in the indirect (F_1) dimension of the 2D experiment is subjected to incrementation. In the F_1 dimension, the ^{13}C

signal intensity, which is directly related to the underlying dipolar interaction, is modulated depending on the rotor position (determined by the length of the increment taken). By applying the π pulse train during the reconversion period, the antiphase coherence is converted back into transverse coherence state.

Different laboratory frame recoupling experiments have been proposed (Table 3.1), most of them originating from the group of Prof. Spiess at MPIP-Mainz. They can be classified according to:

(i) the nucleus from which the recoupling procedure starts,

(ii) the nucleus detected,

(iii) the coherence state probed in the indirect dimension.

Excluding the TEDOR experiment, which lacks the possibility to create sidebands by reconversion rotor encoding, as the t_1 period is placed in front of the π pulse train, all other experiments can be distinguished further by the symmetry or asymmetry of the coherence transfer pathways. The DIP (dipolar) experiments are symmetric in respect to the recoupling procedure, i.e. the recoupling starts and ends at the same nucleus (channel). The REPT (recoupled polarization transfer) techniques are the solid state analogues of the well-known solution INEPT (insensitive nuclei enhanced by polarization transfer) method. Both INEPT and REPT follow the concept of using the initial I (proton) magnetization to generate antiphase coherences, which are later on used for a polarization transfer to the S (^{13}C) nuclei.

The obvious difference is that in solution J-couplings are mediating the polarization transfer, while in the solid state dipolar couplings are used for the process. In addition, the REPT techniques are asymmetric in respect to the recoupling procedure.

Relevant for this work are the REREDOR and REPT-HDOR methods; therefore, they are discussed in more details.

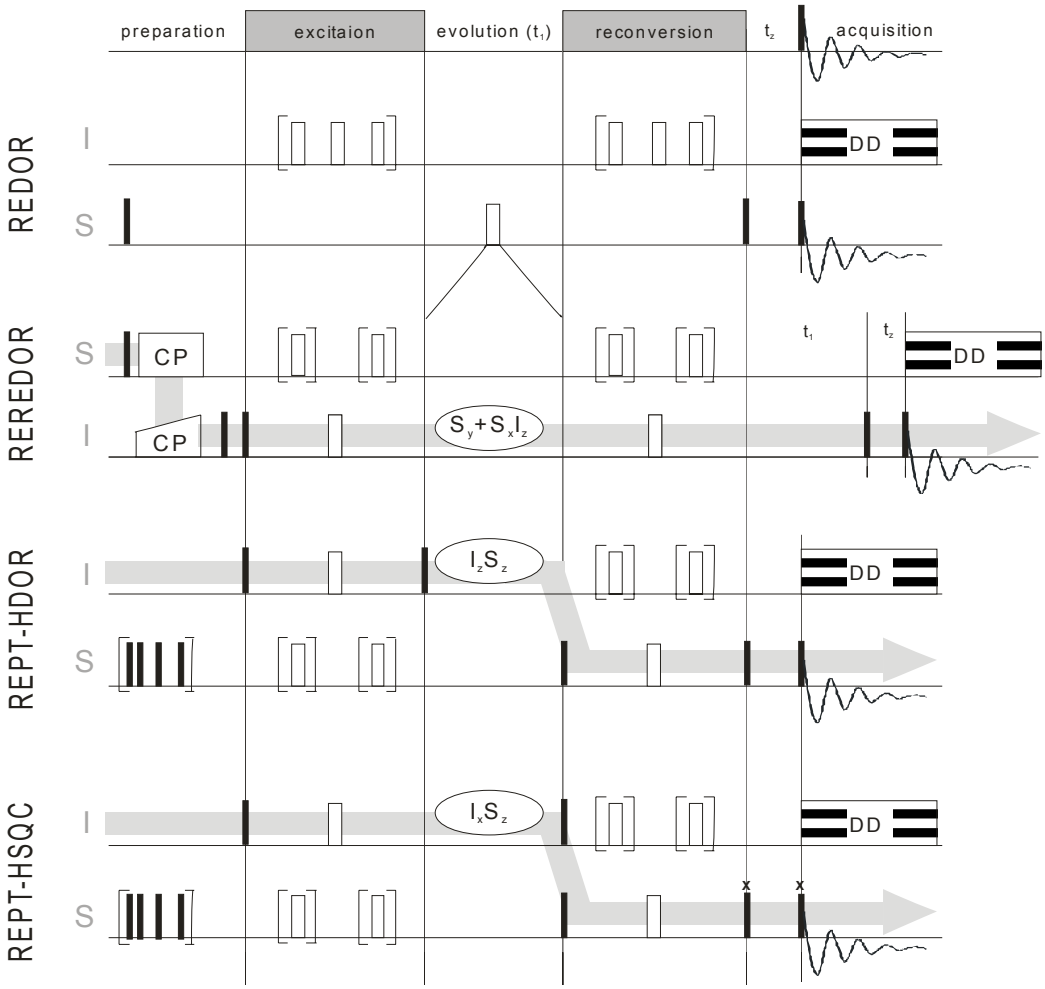

Figure 3.3 Pulse sequences for some REDOR-based heteronuclear correlation NMR techniques. The grey arrows indicate the desired pathway for the transverse components of the coherence states in the indirect dimension.

3.3.1. REPT-HDOR (Recoupled Polarization Transfer Heteronuclear Dipolar Order Rotor Encoding)

The pulse sequence of the REPT-HDOR experiment is depicted on Figure 3.3.1. The experiment is based on creating a state of dipolar longitudinal order, $\hat{I}_z\hat{S}_z$, during t_1. After the initial saturation pulse train on the S channel, a build-up of antiphase coherence $\hat{I}_x\hat{S}_z$ is achieved during the excitation time. A 90° pulse, applied on the I channel, converts this antiphase coherence into a state of longitudinal dipolar order, $\hat{I}_z\hat{S}_z$. This spin state does not

evolve during t_1, which is a significant advantage as incrementing the evolution period results in signal amplitude modulations, which arise solely due to the reconversion rotor encoding (RRE) mechanism. After the t_1 evolution period this state is converted back into antiphase coherence, $\hat{I}_z\hat{S}_y$, by a 90° pulse on the S spins. During the subsequent reconvertion period, this antiphase coherence evolves back into observable SQ coherence. The S-detected signal of the HDOR experiment for a simple coupled ^{1}H-^{13}C spin pair reads:

$$S_x(t_1) = \left\langle \sin(N_{exc}\overline{\Phi}_0)\sin(N_{rec}\overline{\Phi}_{t_1}) \right\rangle \tag{3.9}$$

$$S_y(t_1) = \left\langle \sin(N_{exc}\overline{\Phi}_0)\sin(N_{rec}\overline{\Phi}_{t_1}) \right\rangle \tag{3.10}$$

and the brackets denote the respective powder average

For multispin systems, e.g. CH_2 and CH_3 pairs, equations (3.9) and (3.10) should be replaced by the appropriate multispin formulas.[33]

Incrementing t_1 results in spinning sidebands, which are only odd-ordered, centered at the zero offset frequency in the indirect dimension. As the I spin chemical shift evolution is not present during t_1, there is no need to record a second (sine) data set for the needs of a phase-sensitive detection. Instead, a second cosine dataset is recorded for a second rotor period of t_1 evolution and concatenated with the first one prior to Fourier transformation. Thus, no Gaussian broadening is needed to suppress the *sinc* cut-off wiggles as could be the case in a directly 2D-Fourier-transformed spectrum and the spinning sidebands can be artificially narrowed. Additional advantage, which however is characteristic for all experiments where the applied recoupling procedure is shorter than several rotor periods under fast magic angle spinning conditions, is that no signal decay is observed due to the carbon T_1 relaxation, as the latter relaxation times are longer than the recoupling procedure itself. Also, like any other recoupling experiment, where the sidebands generation mechanism is RRE, the number of the spinning sidebands can be deliberately adjusted by the length of the recoupling time, which itself is a function of the spinning frequency. Practically, the recoupling time is chosen such that the product $D_{IS}\tau_{rcpl} \approx 1.6$. Figure 3.4 presents simulated sideband patterns for various values of $D_{IS}\tau_{rcpl}$. Theoretically, varying the spinning frequency or recoupling time would allow for fulfilling the condition stated above. In rigid solids this is difficult to achieve as fast spinning is needed (which automatically imposes a limitation) to decouple better the net of ^{1}H homonuclear coupling.

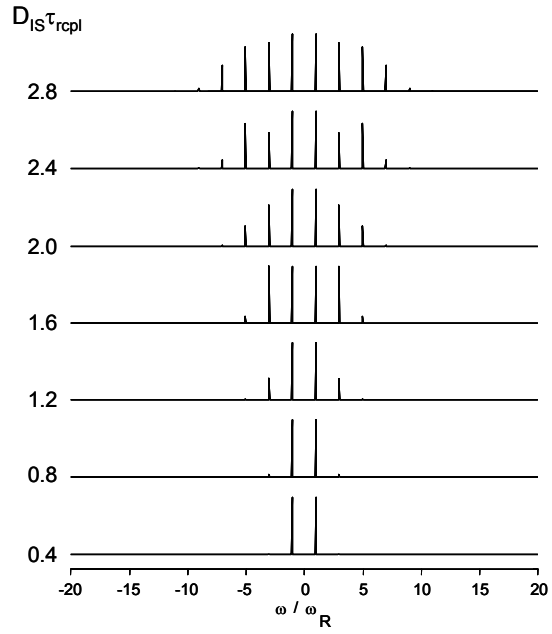

Figure 3.4 Simulated sideband patterns for different values of the $D_{IS}\tau_{rcpl}$.

In addition, it should be mentioned that in the REPT-HDOR experiment the rigid (on kHz frequency scale) CH_2 groups exhibit zero signal for recoupling times of about 80 μs length. In this case, the use of the REREDOR method is advantageous, as this limitation is invalid. However, the lack of REPT-HDOR signal is also information, though not quantitative, about the respective rigid CH_2 moiety, whose signal is missing at a given experimental temperature range.

3.3.2. REREDOR (Rotor Encoded Rotational Echo Double Resonance)

The pulse sequence of REREDOR[34] (rotor encoded rotational echo double resonance) is presented on Figure 3.3. Like in the REPT-HDOR sequence, REREDOR uses the RRE mechanism to create spinning sideband patterns, from which the ^{1}H-^{13}C dipolar couplings are extracted. However, a difference is that the evolution t_1 period is inserted twice in the sequence - not only after the excitation (first recoupling) pulse block, but also after the reconversion (second recoupling) block. The second t_1 inserted at the end of the sequence in combination with the π pulse placed on the S channel in the middle of the first and second recoupling periods serve to refocus the S chemical shift evolution.

The time evolution of the spin system is calculated using the sum of the phases, acquired under the influence of the pulse sequence and averaged over the Euler angles β and γ (performing isotropic "powder average" for the unoriented samples).

$$S \propto \left\langle \prod_i \cos\left(N_{exc}\overline{\Phi}_0^{(i)} - \Phi^{(i)}(0,t_1) - N_{rec}\overline{\Phi}_{t_1}^{(i)} + \Phi^{(i)}(t_1,2t_1) \right) \right\rangle_{\beta,\gamma} \tag{3.11}$$

The product represents the coupling of the spin S to more than one spin I. As the strongest dipole-dipole couplings dominate the spinning sideband patterns, generated by the experiment, in cases of weak couplings or very fast MAS, the two terms $\Phi^{(i)}(0, t_1)$ and $\Phi^{(i)}(t_1, 2t_1)$ become small or even negligible, and thus can be excluded. Therefore, the equation describing a single coupling could be written as:

$$S \propto \left\langle \cos\left(N_{exc}\overline{\Phi}_0 - N_{rec}\overline{\Phi}_{t_1} \right) \right\rangle \tag{3.12}$$

$$\propto \left\langle \sin N_{exc}\overline{\Phi}_0 \sin N_{rec}\overline{\Phi}_{t_1} \right\rangle + \left\langle \cos N_{exc}\overline{\Phi}_0 \cos N_{rec}\overline{\Phi}_{t_1} \right\rangle \tag{3.13}$$

For $\tau_R/2$

$$\overline{\Phi}_0^{(i)} = \frac{\sqrt{2}N_{exc}D_{i,j}}{\pi\omega_R}\sin 2\beta \sin\gamma \tag{3.14}$$

$$\overline{\Phi}_{t_1}^{(i)} = \frac{-\sqrt{2}N_{rec}D_{i,j}}{\pi\omega_R}\sin 2\beta \sin\left(\omega_R t + \gamma\right) \tag{3.15}$$

where t take values in the range:

$$t = 0 \div \frac{n-1}{n} \cdot \frac{1}{2\pi\omega_R}$$

and n is the number of the increments in the indirect dimension.

As can be seen from equation (3.13) when incrementing the evolution period both sin-sin and cos-cos terms are present, leading to sideband of both even and odd order.

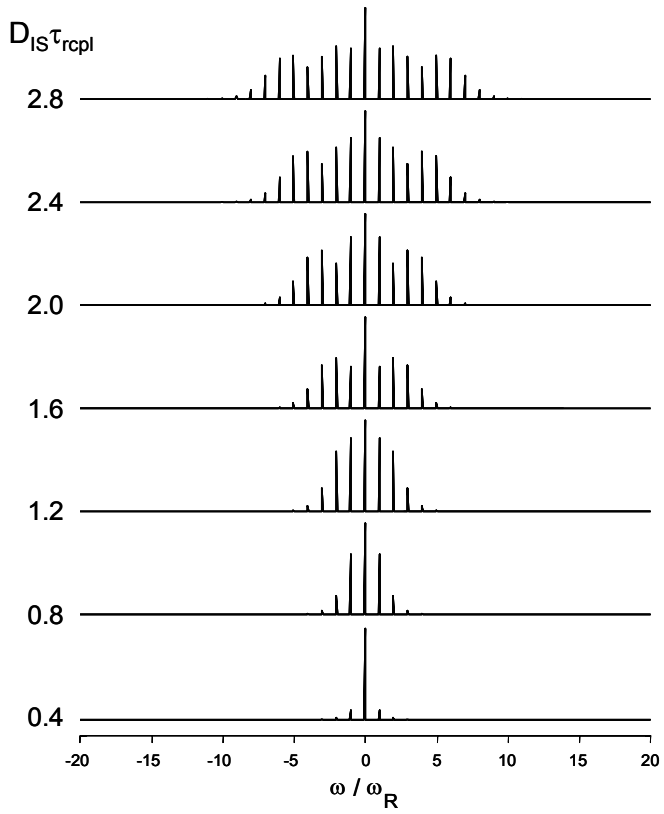

Figure 3.5 Simulated REREDOR sidebands as a function of $D_{IS}\tau_{rcpl}$.

Thus, the REREDOR experiment generates more sidebands compared to the REPT-HDOR pulse sequence at the same spinning speed. This is particularly useful at short recoupling times and fast MAS as the REREDOR method generates sufficient number of sidebands to have a reliable fit (contrary to HDOR) and thus determine the ^{1}H-^{13}C dipole-dipole couplings. The simulated REREDOR sidebands as a function of $D_{IS}\tau_{rcpl}$ are presented on Figure 3.5.

In addition, the dipolar couplings of rigid CH_2 groups can be determined at recoupling times longer than 60 μs, while the HDOR technique fails to accomplish such task due to CH_2 signal cancellation effect. Moreover, the REREDOR method can benefit from an initial cross-polarization step, which results in better signal-to-noise ratio. In relatively mobile systems where the cross-polarization efficiency is low, direct ^{13}C excitation has been successfully applied. Some of the characteristic features of both methods are presented in Table 3.1. Concluding, in theory REREDOR is clearly superior compared to REPT-HDOR. However, in some practical applications (for determination of the dipolar coupling of CH_2 and CH_3

groups, especially in very mobile systems) the simplicity of HDOR have been proven more useful.

	REREDOR	REPT-HDOR
Starting from	$\hat{S}_{x/y}$	$\hat{I}_{x/y}$
Detected on	S	S
Coherence state during t_1	$\hat{S}_y + 2\hat{S}_y\hat{S}_z$	$2\hat{S}_z\hat{I}_z$
Sidebands generation mechanism	RRE	RRE
Modulation during the evolution period	sin-sin + cos-cos terms	cos-cos terms
Detecting mobile CH_2 groups	yes	no
Sideband patterns at low $D_{IS}.\tau_R$	meaningful	first order sidebands
Experimental time*	~ 23 h 1 min	~ 25 h 11 min
Signal-to-noise	initial CP step	-

* Calculated for 2 k scans, 20 increments in the indirect dimension and 2 s recycle delay

Table 3.1 Comparison between REREDOR and REPT-HDOR recoupling techniques

3.3.3. TEDOR (Transferred-Echo Double Resonance)

The magic angle spinning experiment TEDOR (Transferred-Echo Double Resonance) was introduced in 1992 by Hing[35,36] to measure I-S dipolar coupling of heteronuclear I-S pairs of spin-½ nuclei while eliminating unwanted background signals from uncoupled I and S spins via a coherence transfer process. In the first step of the TEDOR experiment (Figure 3.6), a dephasing π pulse prevents the MAS refocusing of the I-S dipolar interaction. Thus, an effective dipolar coupling has been created (averaged over a full rotor cycle). Then, a coherence transfer is performed (*via* simultaneous irradiation on both channels) to select the S spins dipolar-coupled to I spins from the measured spin system, containing also uncoupled S spins. An observable signal arising from the selected S spins is then created and modulated by a refocusing π pulse.

The method just like the HDOR, has the same limitations to obtain information about the mobility of rigid CH_2 groups because the ^{13}C signal of rigid methylene moieties

disappears for recoupling times longer than 80 μs, which under fast MAS (25 kHz) corresponds to two rotor periods. The reason are interfering effects of the two C-H couplings of the CH_2 group. At longer recoupling times less signal intensity is recovered, which practically means that for spinning at 25 kHz and faster, no CH_2 signal is detected. At the same time, the signal intensity for CH moiety oscillates at *ca.* 70% of the maximum signal intensity for relatively long time.

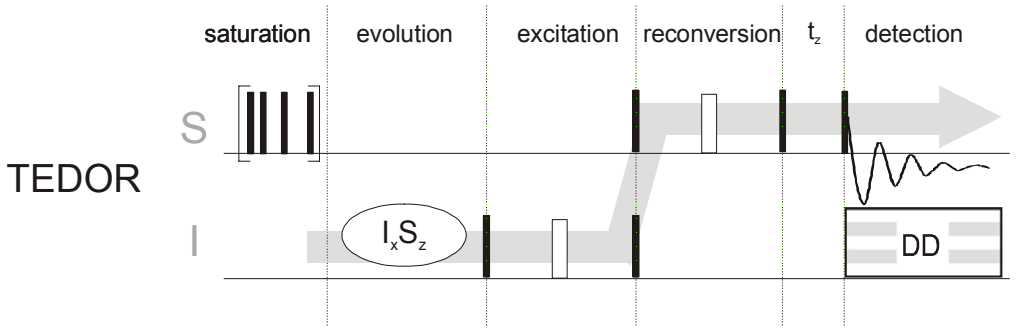

Figure 3.6 Pulse sequence of TEDOR (Transferred-Echo Double Resonance). The evolution period in this case is inserted immediately after the saturation pulses on the S (^{13}C) channel. Thus, recording spinning sidebands, respectively to quantitatively determine heteronuclear dipolar couplings, is not possible.

Similar to REPT-HSQC (recoupled polarization transfer heteronuclear single quantum correlation) or BaBa (Back-to-back), the TEDOR sequence can be used in its two-dimensional version to record correlation spectra. Typically, the carbon chemical shift in the direct spectral dimension is correlated to the proton chemical shift in the indirect dimension. It is important to note, that in cases of proton resonances with close frequencies, sufficient number of experiments have to be recorded in the indirect dimension to achieve the required resolution.

3.4. Homonuclear dipolar recoupling - Back-to-back (BaBa) pulse sequence

Feike et al[11] introduced the Back-to-Back (BaBa) sequence as a multiple-quantum technique based on recoupling the homonuclear dipole-dipole couplings under fast magic angle spinning conditions. Today, the sequence is routinely used in its variant for double-quantum generation for the determination of ^1H-^1H internuclear distances or in cases of known internuclear distances to evaluate molecular or segmental mobility. The BaBa pulse scheme is presented in Figure 3.7.

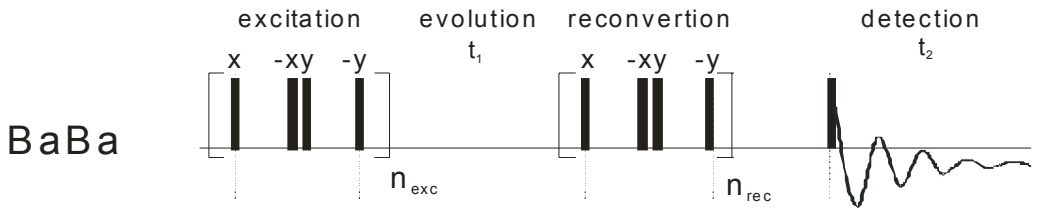

Figure 3.7 Schematic representation of the back-to-back pulse sequence

The basic segment of the sequence is ($90_x - \tau_R/2 - 90_{-x}90_y - \tau_R/2 - 90_{-y}$), as for longer excitation times the phases of the pulses can be set in a way that the sequence is compensated with respect to offset effects and pulse imperfections. The pulse scheme recouples the homonuclear dipole-dipole coupling, which is described as:

$$\hat{\bar{H}}_{dip,\mathrm{hom}} = \hat{T}_{20}^{ij} \cdot \frac{1}{t} \cdot \int_0^t A_{20}^{LAB} = \hat{T}_{20}^{ij} \cdot \frac{1}{t} \cdot \sqrt{\frac{3}{2}} \Phi_{dip,\mathrm{hom}} \tag{3.16}$$

where

$$\Phi_{dip,\mathrm{hom}} = -\sqrt{2} D_{ij} \frac{\sin 2\beta}{\omega_R} \cdot (\sin(\gamma + \omega_R t) - \sin\gamma) + D_{ij} \frac{\sin^2 \beta}{2\omega_R} \cdot (\sin(2\gamma + 2\omega_R t) - \sin 2\gamma) \tag{3.17}$$

For a DQ coherence generation the average Hamiltonian for a BaBa segment is given[37] by:

$$\hat{\bar{H}}_{BaBa} = \frac{1}{\tau_R} \cdot 3 \cdot \Phi_{dip,\mathrm{hom}} \Big|_0^{\tau_R/2} \left(\hat{T}_{2,+2}^{ij} + \hat{T}_{2,-2}^{ij} \right) = \frac{\Omega^{ij}\left(0, \frac{\tau_R}{2}\right)}{\tau_R} \cdot \left(\hat{T}_{2,+2}^{ij} + \hat{T}_{2,-2}^{ij} \right) \tag{3.18}$$

where the notation $\Omega^{ij}\left(0, \frac{\tau_R}{2}\right) = 3 \cdot \Phi_{dip,\mathrm{hom}} \Big|_0^{\tau_R/2}$ is introduced to use the same notation as mostly found in literature. Calculating $\Omega^{ij}(0, \tau_R/2)$ yields

$$\Omega^{ij}\left(0, \frac{\tau_R}{2}\right) = \frac{3\sqrt{2} D_{ij}}{\omega_R} \sin 2\beta_{ij} \sin \gamma_{ij} \,. \tag{3.19}$$

Applying the BaBa Hamiltonian to a spin-pair system in thermal equilibrium, results in a DQ coherence, whose amplitude is modulated by $\sin\left(\Omega_{exc}^{ij}\right)$. During reconversion, a corresponding amplitude modulation by $\sin\left(\Omega_{rec}^{ij}\right)$ is introduced. For N rotor periods

excitation and reconversion time, the relative double-quantum signal intensity can be described by multiplying the modulations from excitation and reconversion time

$$S_{DQ}^{(ij)}(t_1) \propto \left\langle \sin N\Omega_{exc}^{ij} \cdot \sin N\Omega_{rec}^{ij} \right\rangle_{\beta,\gamma} \tag{3.20}$$

where the brackets imply the need of performining the orientational averaging procedure needed for powdered samples. As indicated in equation 3.17 the DQ signal depends on the t_1 evolution time. So in the one-dimensional experiment ($t_1 = 0$) the BaBa sequence serves as a double-quantum filter. In its 2D version, depending on setting the t_1 or the t_1 increment, Δt, the sequence can be performed respectively either as a rotor-synchronized experiment (chemical shifts correlation spectrum is recorded) or to record ^{1}H-^{1}H DQ MAS spinning sideband patterns by incrementing the t_1 in steps smaller than the rotor period (to evaluate the dipole-dipole coupling).

3.4.1 DQ Build-up curves based on the BaBa sequence

Double-quantum filtered spectra are recorded using the BaBa sequence, with t_1 set equal to zero. Monitoring the DQ filtered signal as a function of the excitation times leads to DQ build-up curves, from which the underlying dipole-dipole coupling strength can be determined. In spectra, where short excitation times are selected, only the strongest ^{1}H dipolar couplings contribute to the observed signal intensity, whereas for longer excitation times, respectively the signal of weaker couplings is observed. It should be mentioned that a rigid system, where a dense network of proton couplings is present, does not follow the behavior of an isolated spin pair. The reason is that the network of couplings leads to the presence of multispin coherences, which are (in part) also excited by the BaBA sequence. Thus, increasing the recoupling time such a system develops its multispin character, which is expressed in cancellation of the characteristic oscillations, as several couplings with different strength are destructively superimposed. The reason is that the excited higher spin correlations and higher order coherences relax faster, and thus, reduce the overall DQ intensity at longer recoupling times.

In some cases, it is possible to extract the dipole-dipole coupling directly from the build-up curves, if the DQ signal is generated from a well-separated spin pair. However, if

the characteristic oscillations are not observed, a complicated procedure has to be applied. It is based on equation 3.21, where the DQ intensity is presented as the product:

$$S_{DQ} = A \cdot D_{ij}^2 \tau_{exc}^2 \cdot e^{-\tau_{exc}/\tau_{DQ}} \qquad (3.21)$$

The factor A, which contains several constants, is fixed for a series of experiments. As usually A is unknown, only relative strengths of the homonuclear couplings are obtained. The exponential term is introduced to describe the decay of the DQ coherence with the time constant τ_{DQ}. Taking into account that strong dipole-dipole couplings lead to pronounced decay effects and thus require very high spinning speeds, which often cannot be routinely applied, as well as set high requirements on the recoupling procedure, only weak dipolar couplings are determined by the build-up approach. Examples of such studies are mobile systems such as polymer melts[38] or non-protonated systems with weak dipole-dipole couplings, e.g. ^{31}P-^{31}P in crystalline phosphates.

For the determination of strong dipole-dipole couplings analysis of spinning sideband patterns have proven to be much more useful. The approach (discussed in chapter 3.4.3) is practically applied for measurements of all types of homonuclear couplings of abundant nuclei (in cases of isolated spin-pairs), with the consequent conclusions on either dynamics (in cases of known distances) or distances (between nuclei involved in a coherence) determination.

3.4.2 Rotor-synchronized 2D BaBa experiments under fast MAS

In the 2D BaBa spectra setting t_1 equal to integer multiples of the rotor period results in rotor-synchronized signal acquisition, respectively rotor-synchronized spectra. In the spectra the evolution of the selected DQ coherence during the t_1 period (monitored in the indirect spectral dimension) is correlated with the SQ signal (observed in the direct dimension) detected during the acquisition period. The chemical shift and the dipole-dipole couplings (between more than two spins) influence the DQ coherence evolution during t_1. The former induces a modulation in the form $\exp\{i(\omega_{CS}^{(i)} + \omega_{CS}^{j})t_1\}$, if no evolution due to dipolar coupling interaction occurs during t_1. However, a spin outside but coupled to those involved in the coherence might give rise to an evolution of the DQ coherence of such contributions are not refocused during the reconversion period. The result usually is a signal

loss. Thus, the signal position in the indirect spectral dimension is governed by the isotropic chemical shift evolution of the DQ coherence with a frequency being the sum of the individual isotropic chemical shifts of the spins involved in the coherence. Therefore, it is convenient to display the two-dimensional rotor-synchronized experiment with the t_1 (the indirect) dimension being scaled by a factor of two compared to the t_2 (the directly detected) spectral dimension.

A schematic rotor-synchronized DQ spectrum is depicted in Figure 3.8. The peak positions in ppm are denoted as (CS_2, CS_1) or in Hz, respectively (ω_2, ω_1), where the ω_2 is the SQ frequency and ω_1 the DQ frequency of the spectral peak. Thus, two types of signal patterns are present in the DQ spectrum, namely diagonal peaks (CS_C, $2CS_C$) due to coherence between spins with like chemical shifts and cross-peaks (CS_A, CS_{A+B}) and (CS_B, CS_{A+B}), symmetrically situated on both sides of the diagonal. Ideally, the two cross-peaks have equal intensity, as the intensity of the cross-peak corresponds to the number of the involved spins (typically identical for both cross-peaks).

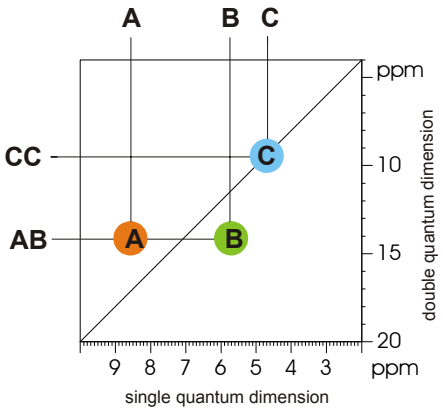

Figure 3.8 Schematic rotor synchronized two-dimensional BaBa spectrum with a diagonal peak arising due to double quantum coherence between spins with the same chemical shift and two cross peaks due to coupled spins involved in a coherence having different chemical shifts

It should be noted that even though the homonuclear dipole-dipole coupling term does not contribute to the rotor-synchronized amplitude modulation with respect to t_1, it still governs the overall intensity of a peak in the 2D DQ MAS spectrum. Thus, to detect the peak due to a specific DQ coherence, the recoupling time should be set properly in respect to the rotor period.

3.4.3 ^{1}H-^{1}H DQ spinning sideband patterns under fast MAS

The 2D BaBa sequence can be performed either in the rotor-synchronized fashion discussed in the previous section (with the increment of the evolution period set equal to integer multiples of the rotor period τ_R), or incrementing t_1 in steps smaller than τ_R, which leads to spinning sideband patterns along the indirect dimension. The sidebands intensity is a function of two parameters, namely the excitation (recoupling) time and the strength of the dipole-dipole couplings. The mechanism responsible for the sidebands appearance in this case is the reconversion rotor encoding (RRE) and has to be distinguished from the evolution rotor modulation (ERM) mechanism. The latter gives rise to the sidebands observed in the 1D slow magic angle spinning SQ spectra, due to the evolution of the anistropic interaction (CSA, dipole-dipole couplings) under MAS. The former, e.g. RRE, arises from the rotor phase dependence of the average Hamiltonian describing the excitation and reconversion periods (Figure 3.9). It should be noted that RRE does not necessarily require spin evolution (in particular the chemical shift evolution) in t_1 and so terms arising from such evolution are left out.

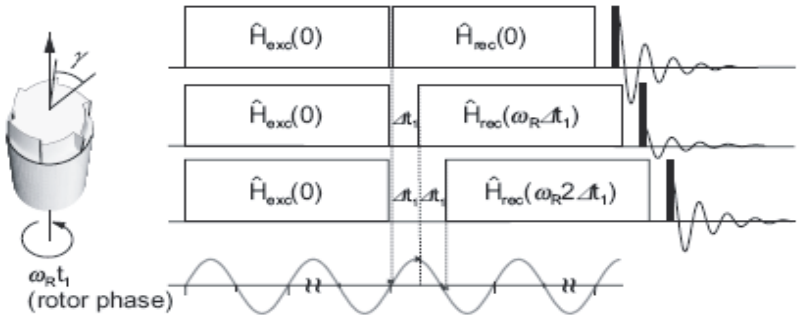

Figure 3.9 Schematic illustration of the principle of the Reconversion Rotor Encoding (RRE)

Comparing the experiment performed with t_1 set to zero and t_1 being incremented in steps smaller than the rotor period, it is obvious that in the former case the excitation and reconversion periods have inherently the same initial rotor phase, which is manifested in the integrated phase Ω^{ij} (equation 3.19). As seen from Figure 3.9, if t_1 is incremented, the integrated phases for the excitation and reconversion differ with respect to their initial phases, as the chemical shift evolves in t_1 from increment to increment. Thus

$$\Omega_{exc}^{ij}(0,\tau_R) = \frac{3\sqrt{2}D_{ij}}{\omega_R}\sin 2\beta_{ij}\sin\gamma_{ij} \tag{3.22}$$

is not equal to

$$\Omega_{rec}^{ij}\left(\frac{\tau_R}{2}+t_1,\tau_R+t_1\right) = -\frac{3\sqrt{2}D_{ij}}{\omega_R}\sin 2\beta_{ij}\sin\left(\omega_R t_1+\gamma_{ij}\right) \tag{3.23}$$

Obviously, the integrated phase of the reconversion period is shifted or "rotor-encoded" by the term $\omega_R t_1$ in the argument of the sine function, compared to the one of the excitation period. Consequently, signal acquisition is performed at times equal to $n\Delta t_1$, where n is the number of increments in the t_1 evolution period and Δt_1 is the length of an individual increment. Thus, it is clear that the RRE mechanism requires inherently 2D experiments at least. In addition, the DQ signal can be given as:

$$S_{DQ}^{(ij)}(t_1) \propto \sin(N\Omega^{ij}(0,\frac{\tau_R}{2}))\cdot\sin(N\Omega^{ij}(\frac{\tau_R}{2}+t_1,\tau_R+t_1)) \tag{3.24}$$

which taking into account equation 3.22 and replacing all terms, which do not depend on t_1 by the coefficients C_{ij}, can be written as:

$$S_{DQ}^{(ij)}(t_1) \propto \sin(C_{ij}\cdot\sin(\omega_R t_1+\gamma)) \tag{3.25}$$

Using the mathematical relation:

$$\sin(x\sin(\omega_R t_1+\gamma)) = 2\sum_{n=0}^{\infty}J_{2n+1}(C_{ij})\sin((2n-1)\omega_R t_1+(2n+1)\gamma) \tag{3.26}$$

the DQ signal intensity can be expressed as a Fourier series, whose terms contain Bessel functions $J_n(C_{ij})$ of n^{th} order

$$S_{DQ}^{(ij)}(t_1) \propto 2\sum_{n=1}^{\infty}J_{2n+1}(C_{ij})\sin((2n-1)\omega_R t_1+(2n+1)\gamma) \tag{3.27}$$

So, after Fourier transformation in t_1 the sideband pattern consist of only odd-order sidebands, as the DQ signal is modulated only by odd multiples of the ω_R. In addition, the intensity distribution over the sidebands is determined by the Bessel functions and the coefficients C_{ij}, which depend on the orientation of the dipole-dipole coupling tensor (β, γ) and on the product $D_{ij}\tau_R$ (Simulated ^1H-^1H spinning sideband pattrns for various $D_{ij}\tau_R$ are presented on Figure 3.10).

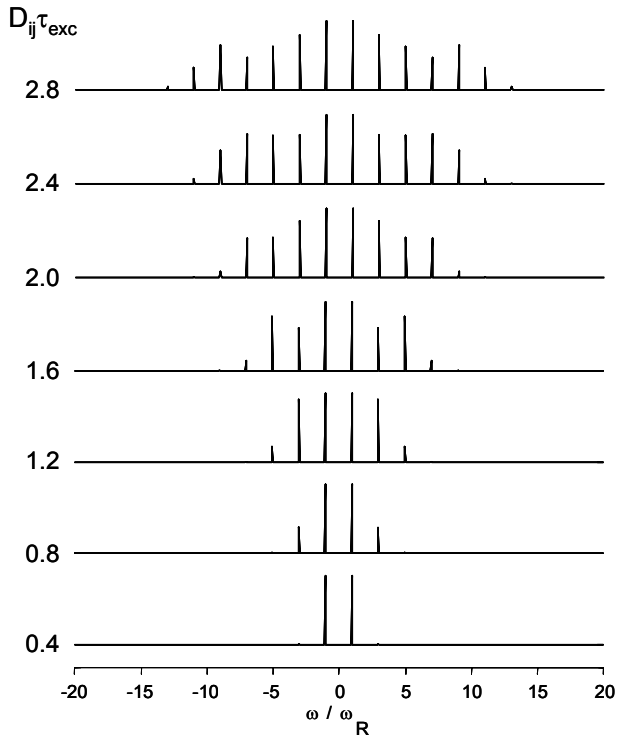

Figure 3.10 Simulated spinning sideband patterns for various $D_{ij}\tau_{exc}$.

Therefore, the sidebands bear information about the sample orientation and dipole-dipole coupling strength. The latter constants can be extracted for samples with known orientation (for example powder samples, if the respective powder averaging procedure is performed) by comparison with simulated sideband patterns. This analytical procedure relies on the assumption of having an isolated spin pair, which is seldom the case in organic solids. Typically, remote, and thus weakly coupled, protons contribute to the intensity increase in the sideband patterns, as a rule of thumb, in the first order sidebands. For this reason, the first order sidebands do not present a reliable fit in the simulation procedure and are often ignored. Another observation in multispin systems is the presence of even order sidebands, which

arise due to evolution of the DQ coherence under coupling to third spins outside the coherence. Here the mechanism for sidebands generation is clearly ERM, which is actually suppressed by increasing the spinning speeds.

It should be mentioned in addition, that each sideband presents intensity weighted full "rotor-synchronized" spectrum (Figure 3.11) and therefore the sidebands arising from various couplings can be distinguished.

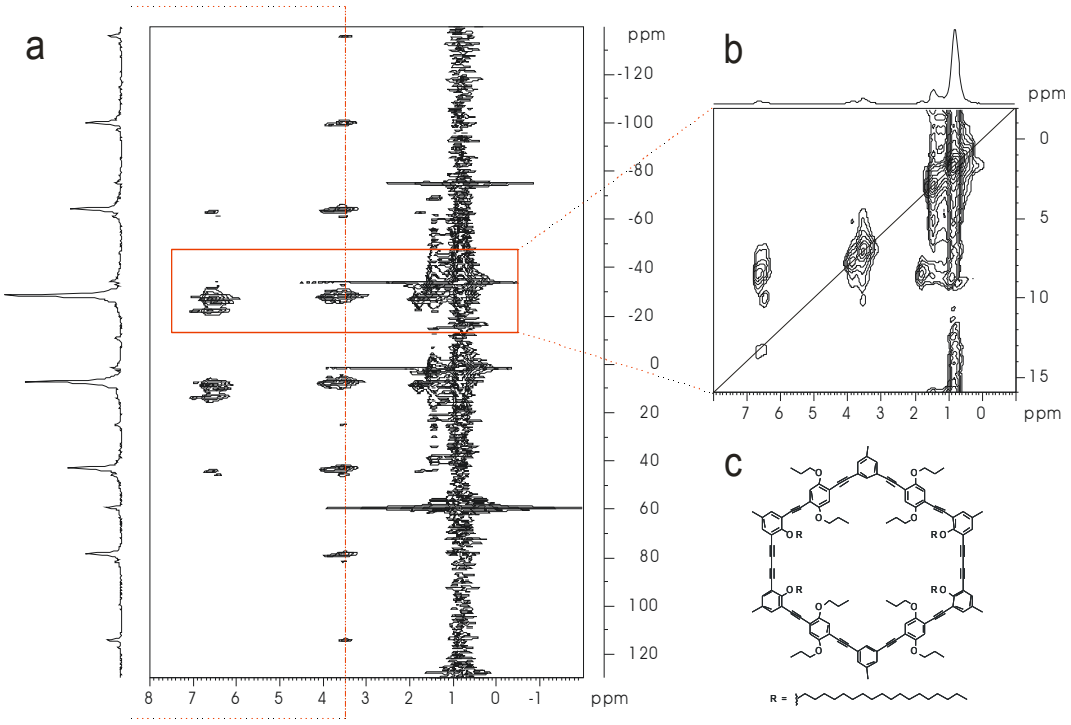

Figure 3.11 Two-dimensional ^{1}H BaBa experiment recorded at 410 K effective sample temperature, 12.5 kHz MAS and 640 μs recoupling time with the t_1 period incremented to observe 7th order sidebands **a)** for the macrocycle **c)**[39]**.** The slice at 3.5 ppm represents the spinning sideband pattern for the OCH_2 propyl groups. The magnification represents a rotor synchronized 2D BaBa spectrum **b)**.

Chapter 4. Molecular Motion

4.1. Timescales of Molecular Motion

A characteristic feature of the solid state NMR spectroscopy is its ability to study molecular motions over a wide range of timescales, ranging from picoseconds to several seconds. To detect the different types of motion by means of NMR requires a change in the nuclear spin Hamiltonian. Generally, the molecular motions can be described as:

1. vibrations – All nuclei oscilate rapidly (typically on the timescale of picoseconds or shorter) about their mean position. In cases where many atoms are involved, the vibrational motion is slower, esp. if these atoms are massive. Lighter atoms as hydrogens undergo rapid local oscilations (librations) perpendicular to the axis of the C-H bond with amplitudes of about ±15°.

2. local rotation of molecular groups – A prerequisite for this rotational motion and jumps (in the picosecond timescale) is the presence of local (typically threefold) site symmetry. Such motion is characteristic for the methyl group, as well as the protonated amino (NH_3^+) group in the N-terminal peptide or protein position or side groups.

3. molecular flexibility – this type of motion is characteristic for large molecules like polymers

4. chemical exchange – This type of processes occur over a very wide range of timescales, from nanoseconds to several seconds, or even longer. As chemical exchange are considered the processes of making and breaking chemical bonds (for example an internal cyclization reaction) or the change in the conformation of the molecule about a more rigid region or entity such as a double bond or a conjugated system.

5. molecular rotations – This motion is characteristic for the molecules in solution (where the process is random) or for liquid crystalline molecules in the mesophase. In the first case, the anisotropic interactions as chemical shift anisotropy, dipole-dipole couplings and quadrupole couplings, are completely averaged out due to the fast isotropic molecular tumbling, which includes both molecular rotations and diffusion. In the second case, a typical reduction of the dipolar couplings by 50% is observed on the onset of molecular rotation (esp. considering disc-like molecules) when the compound enters the liquid-crystalline phase. It should be noted that in cases of columnar discotic compounds, where the predominant motion in the mesophase is a rapid axial rotation in respect to the columnar, resp. director axis, only

tensors or their projections, which are parallel to the disc plain, are averaged out. Tensors, which are parallel to the director remain unaffected by the axial rotation, i.e. they are only influenced by out-of-plain excursions of the discotic molecules.

Another quite interesting example for molecular rotations is observed in a type of molecular solids called plastic crystals. In these systems, the molecular centers of gravity are fixed with respect to the crystal lattice, but the molecules themselves rotate rapidly about their lattice sites. In these systems a subject of averaging are the intramolecular interactions, while the weaker intermolecular interactions remain unaffected.

It is also important to note that the timescale of molecular rotations depends on the molecular size (bigger molecules exhibit slower rotations), viscosity (higher viscosity leads to increases the rotational time) and temperature (higher temperature leads to lower rotational correlation time).

6. translational motions – There are two types of translational motion – diffusion (the translation is random) and flow (the translation is concerted and directed). In solids, the diffusional motion is usually insignificant on the NMR timescale. However, in liquid crystals (such compounds are predominantly discussed in this thesis) the diffusion, esp. in nematic and smectic LCs, is a well-known phenomenon. In columnar discotic or lath-like compounds this type of translational motion is not typical, though the process of a translational diffusion of a discotic mesogen from column to column is not completely excluded.[40] In addition, the probability a lath-like perylene molecule to go out of a column, perform a 180° flip and enter the same or a neighboring column has been calculated to be 10^{-13}.

4.2. The effect of molecular motions on the NMR interactions

In general, depending on the rate of the motion and the type of the interaction being investigated by the solid state NMR recoupling techniques discussed in the thesis, three types of motional regimes can be distinguished, namely: slow, intermediate and fast (Figure 4.1).

In the slow motional regime, on average no reorientation of the molecule takes place during the NMR experiment. Therefore, the spectral intensity as well as the strength of the recoupled interaction (dipole-dipole couplings) derived from the recorded sideband patterns, remains unaffected by the molecular motion in this regime. However, to characterize the slow molecular reorientations again the recoupling approach turns out to be useful. The CODEX (centerband-only detection of exchange) experiment, which is performed under slow magic

angle spinning, employs recoupling of the chemical shift anisotropy before and after a long mixing time during which molecular reorientations may occur. By analyzing differences in the chemical shift tensor before and after the mixing time, the dependence on the reorientational angles is obtained analytically for unaxial interactions, and a relation to a two-dimensional exchange NMR pattern is established.[41-43]

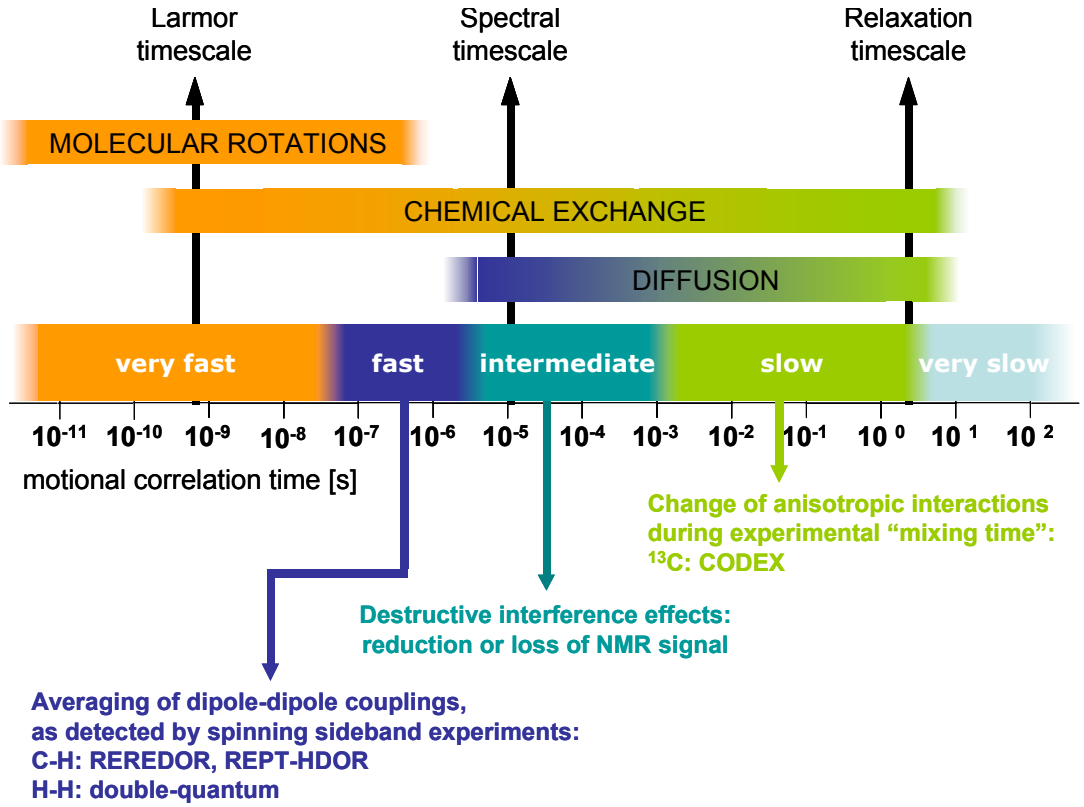

Figure 4.1 Schematic presentation of the motional timescales of some physical processes relative to the timescales of the most important phenomena in an NMR experiment (up) and the effects of these motions on the anisotropic interactions under investigation by the NMR experiments described in this thesis (see below).

As already discussed in the methods section, the main approach of the NMR experiments conducted in such cases (for example CODEX) is to introduce long mixing time between two identical pulse blocks to recouple the chemical shift anisotropy (instead of dipole-dipole couplings). During this

In the NMR spectra of molecules in the intermediate motional regime a typical signal intensity reduction[44] or even loss[45] is observed either for the whole molecule or for definite molecular segments. This regime is met when the rate of the motion k is proportional to $\delta/2\pi$, where δ is the strength of the underlying anisotropic interaction. In most cases, the reason is

that the dynamics in the sample occur on the timescales of the MAS frequency, the frequency of the RF-pulses[46,47] or the applied pulse sequences. Other possible factors leading to signal cancellation can be interference of the heteronuclear decoupling and motions of the C-H dipolar tensor[4,48] or recoupling effects of finite pulses[49].

If the molecules undergo rapid motions the interaction terms (i.e. CSA, dipole-dipole coupling, quadrupolar coupling) are motionally averaged. If the motion is fast enough, i.e. on the ps or less timescale (vibrations, librations), the averaging is done before the secular approximation (introduced due to the strong external magnetic field). In cases where the molecular motions are in the μs timescale, the motional averaging is done after the secular approximation. Thus, the Hamiltonian $\hat{H}_{int}$ describing the internal interactions (see chapter 2) is twice a subject to simplification – due to the secular approximation ($\hat{H}^0_{int}$) and due to molecular motion - motional averaging ($\overline{\hat{H}}^0_{int}$).

4.3. Dynamic Order Parameter and Orientation Distribution from Recoupling NMR Experiments

As discussed in chapter 3, the sideband pattern analysis provide effective (scaled, averaged, experimental) homonuclear ^{1}H-^{1}H and heteronuclear ^{1}H-^{13}C dipolar coupling constants, which are interpreted in terms of local dynamic order parameters, S, given in the form of the second order Legendre polynomial[50]. A common way to determine the local order parameter, S, is to relate the motional averaged effective dipolar coupling constant D_{eff} obtained experimentally to the static dipolar coupling constant D_{rigid} depending only on the spin species involved and on their internuclear distance. In the case of ^{1}H-^{13}C dipolar couplings of CH_n groups, where the distance is not averaged by molecular motions and the geometry of the spin system is known, D_{rigid} can be computed from the distance between the spins involved. The same is valid for ^{1}H-^{1}H dipolar couplings, where the internuclear distances are known, for example the coupling between the protons of the H-C-C-H segment of an aromatic system. From the definition:

$$S = \frac{D_{IS}^{eff}}{D_{IS}^{rigid}} \tag{4.1}$$

it is obious, that S = 1 stands for segments which are totally rigid, whereas S = 0 indicates fast isotropic molecular reorientations on the kHz time scale. All discussed so far is valid for

isolated pairs, where no other perturbing couplings are present. In reality, this is seldom the case, as almost all organic compounds are abundant in protons, thus additional weak couplings from remote protons contribute to the intensity of the recorded sideband patterns.

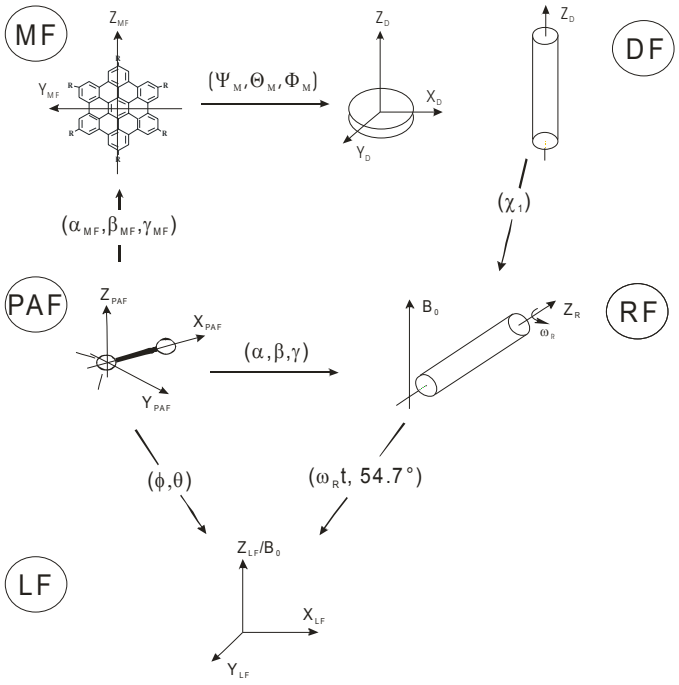

Figure 4.2 Definitions of the angles used to transform different coordinate systems into one another

Therefore, these additional dipolar interactions (taking into account the distance as well as the geometry) influence the effective dipolar coupling constants and respectively the determined local dynamic order parameters. It should be mentioned that such influence is often comparable with the error of the sidebands analysis procedure and expressed predominantly in the lowest (typically first) order sidebands. However, in cases of ordered systems, such as those discussed in the thesis, it is the distribution of molecular orientations about the director axis that may influence more the dipolar coupling constants, as determined from the sideband pattern analysis.

The methodology for extracting orientation distributions from the frequency dependent NMR spectra is well-developed[51]. The sample orientation in ordered systems (columnar discotic structures are uniaxial) in an NMR experiment is described via succesive transformations involving different coordinate systems. Figure 4.2 shows the different coordinate systems and the respective angles used for the transformation of one coordinate system into another. As seen from the Figure 4.2, the respective interaction tensor is defined in its principal axis frame (PAF). In the case of dipole-dipole couplings, which are mainly

investigated in the following, the interaction tensors are directly related to the positions of the atoms, respectively the nuclei, in the molecule. The transformation from the PAF to the molecular frame (MF) is specified by the Euler angles α_{MF}, β_{MF}, γ_{MF}. As all studied molecular systems, no matter if discotic with tetragonal (phthalocyanines) or hexagonal (hexa-peri-hexabenzocoronenes) symmetry or lath-like (perylene derivatives) with bigonal symmetry, form stacks due to π-interactions, a director can be defined, specifying the direction of primary order of the system. The transformation from the MF to the director frame (DF) is achieved taking into account the Euler angles Ψ_D, θ_D, Φ_D. It should be noted, that in cases of discotic molecules forming columnar stacks, only two angle are needed for this transformation. A single rotation about the χ_l angle is needed to transform the director frame into the rotor frame (RF), as both frames are uniaxial. It should be noted that such a step is needed only when the initial sample (director) alignment in respect to the rotor axis is achieved by different sample processing techniques as extrusion or slow cooling of a melt of the LC compound in an external eletric or magnetic field. Otherwise, the columns of stacked discotic molecules, respectively the director axises, are isotropically distributed in the sample, resulting in a pseudopowder spectrum. In such a situation, respectively spectrum, the effects of the neighbouring aromatic systems in a column are still present, as these effects are inherent for the stack itself but are not affected by the orientaion of the columns, e.g. the macroscopic order in the system. The transformation from the rotor frame to the laboratory frame is already included in the equations used for the descriptions of the MAS NMR experiments (chapter 2.9). In the description of the recoupling NMR experiments the relevent orientation for the outcome of the experiment is the orientation of the PAF in the RF, which is specified by the Euler angles α, β, γ. If more than one interaction is considered, the transformation to the molecular frame is needed.

Solid state NMR recoupling techniques can probe the molecular orientaion in respect to the director axis. On average for the sample studied, this means the distribution of molecular orientations in the director frame, provided an initial director orientation in respect to the rotor frame by processing. Under these circumstances, the orientation distribution of the PAF in the rotor frame can be converted to the distribution of molecular orientations in the director frame. Since the systems are uniaxial the α angle is not taken into account, as well as the γ angle, which indicates the initial rotor phase. Thus, an orientation distribution P as a function of the β angle is extracted from recoupling NMR MAS experiments. There are

three ways to obtain the orientation distribution P(β) from an NMR spectrum, which presents a frequency dependent intensity distribution:

(i) direct reconstruction

(ii) direct expansion (best fit of delta-function subspectra)

(iii) moment expansion (best fit of Legendre-polynomial-weighted spectra).

The direct reconstruction approach (i) requires spectra, which directly reflect the angle distributions, i.e. a single spectral peak for each angular peak. Then, the distribution can be directly reconstructed according to the principle of conservation of the area of the corresponding intervals, $S(\omega)d\omega=P(\beta)d\beta$. Recoupling NMR experiments do not meet this condition, thus the approach is not applicable to those.

The direct expansion approach (ii) relies on dividing the experimental spectrum $S^{exp}(\omega)$ into subspectra $S^{th}(\omega,\beta)$ for individual β:

$$S^{\exp}(\omega)=\int_{0^\circ}^{90^\circ} S^{th}(\omega,\beta)P(\beta)d\beta=\sum_{\beta} S^{th}(\omega,\beta)P(\beta) \qquad (4.2)$$

Considering the discrete formulation of the dependence of the experimental signal (equation 4.2), the orientaion distribution can be obtained from a best fit of δ-function subspectra.

The moment expansion approach (iii) is applied in the analysis of orientational distributions of ordered materials. It involves the expansion of the angular distribution in terms of Legendre polynomials $P_L(cos\beta)$.

$$\widetilde{R}(\beta)=\sum_{L}(2L+1)\langle P_L\rangle P_L(\cos\beta) \qquad (4.3)$$

where $P_L(cos\beta)$ is L^{th} order Legendre polynomial and $\langle P_L\rangle$ can be considered an order parameter. Each order parameter characterizes the weight with which the corresponding Legendre polynomial contributes to the probability density $\widetilde{R}(\beta)$ to find a distribution at a given angle β. Thus, the experimental spectrum is considered to consist of contributions from various moments:

$$S^{\exp}(\omega)=\sum_{L}(2L+1)\langle P_L\rangle\int_{0^\circ}^{90^\circ} S^{th}(\omega,\beta)P_L(\cos\beta)d\beta \qquad (4.4)$$

A best fit procedure with the $\langle P_L \rangle$ as coefficients yields the contributins from various moments. Generally, the approach is useful for broad orientation distribuions and yields order parameters which can be directly related to order parameters as obtained from other methods like X-ray scattering.

Recently, another approach has been proposed by Schnell et al[52] to determine the orientational distribution on the basis of recoupling NMR experiments, as well as to distinguish orientational effects and motional averaging of the couplings, which both influence the local dynamic order parameters S. On one hand, distinguishing between orientational effects and motional averaging relies on the sideband pattern sensitivity on $2\omega_R$ recoupling. On the other, an orientation distribution function *P(β)* is incorporated in the simulations as a weighting factor for a given director orientation β and a Gaussian distribution of orientations about this angle is assumed as a convenient approximation.

$$P(\beta) = \exp\left[-\frac{\sin^2(\beta - \beta_0)}{k}\right] \tag{4.5}$$

with

$$k = -\frac{\sin^2\left(\frac{\Delta\beta}{2}\right)}{\ln 1/2} \tag{4.6}$$

where β_0 represents the angle around which the distribution is centered. In the exponential function, $\sin^2\beta$ is used instead of β^2 to render the orientation distribution symmetric, i.e. to fulfil *P(β) = P(180°-β)*. Δβ is the full width of the orientation distribution at the half-maximum amplitude (FWHM). Often the FWHM of a distribution is presented by the standart deviation σ, as $\Delta\beta = 2.35\sigma$. The advantage of a Gaussian orientation distribution is that the probability of a given angle is determined only by the width of the distribution Δβ, which is varied until the calculated sideband pattern fits the experimental pattern best.

Knowing Δβ it is possible to calculate the orientational order parameter S_{or} for the distribution of tensor orientations β with respect to the rotor frame.

$$S_{or} = \langle P_2(\cos\beta) \rangle = \frac{\int_0^1 \frac{1}{2}(3\cos^2\beta - 1)P(\beta)d(\cos\beta)}{\int_0^1 P(\beta)d(\cos\beta)} \tag{4.7}$$

thus S_{or} is zero for an isotropic distribution $P(\beta)$, whereas it becomes 1 or -0.5 for perfect parallel or perpendicular alignment with respect to the rotor axis.

4.4. Molecular dynamics studied by different spectroscopic techniques

Molecular motions can be and are studied by different spectroscopic techniques, like stimulated UV/VIS light absorption[53], FTIR and Raman scattering[54,55], fluorescence spectroscopy[56], solid state homo- and heteronuclear recoupling spin-1/2 NMR techniques[57], ^{2}H NMR spectroscopy[51], NMR relaxation studies[58], line shape analysis in the EPR spectroscopy[59], neutron scattering[60], dielectric spectroscopy[61,62] (the present list is far from being complete, as well as the cited references are just exemplary). In this respect, it is important to realize, that the contribution of any technique to investigate the molecular dynamics is determined by its intrinsic timescale, which, in addition, depends on the phenomena investigated.

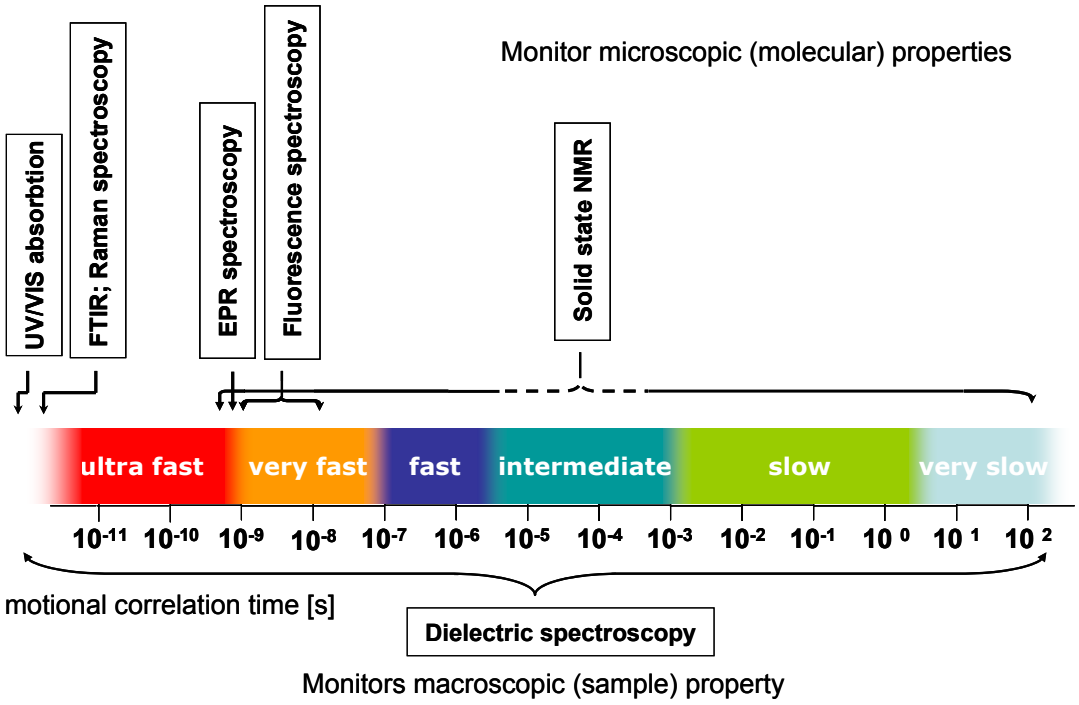

Figure 4.3 Intrinsic timescales of selected spectroscopy methods

In Figure 4.3 a brief summary of the intrinsic timescale of selected spectroscopic techniques, and thus their applicability to investigation of the molecular dynamics, is presented.

The fast and very fast molecular motions can be investigated by experiments, whose intrinsic timescale is even faster. A typical example is the stimulated absorption experiment utilising UV/VIS light, where the method's intrinsic timescale is determined by a photon absorption from the radiation field ($\tau_{int} = 10^{-14}$s). This process occurs before the molecules can change their position or orientation; even local processes like vibrations or proton librations being slower by *ca*. 2 orders of magnitude. Similar is the situation with the FTIR and Raman scattering experiments which have an intrinsic timescale of $\tau_{int} \approx 10^{-12}$s, however, in this case the fast components of molecular motions modulating the shape of the vibrational molecular spectra. Fluorescence experiments are, on the other hand, characterized by a longer time window ($\tau_{int} \approx 10^{-9} \div 10^{-8}$s). This scale is determined by the longer time needed for the photon absorption, followed by a fast non-radiative relaxation to the lowest singlet state and a photon emission to the ground state. However, the experimentalists have the freedom to adjust the sensitivity of the method to a selected timescale as the fluorescence effect depends strongly on the individual photophysical properties of the molecules used. In EPR experiments where nitroxide labels are used (which is a common approach regarding this method) the intrinsic timescale is in the range of $\tau_{int} \approx 10^{-9}$s. So the spectroscopic lineshapes are sensitive to molecular rotations and thus the method is applicable for dynamic studies of liquid-crystalline compounds. However, one should not forget the complications, which arise due to the necessity of synthetic labelling of the samples, which often is hardly feasible.

The same limitation is present in the ^{2}H NMR experiments, which despite this demanding condition, have proven to be quite useful in molecular dynamics studies. In general, the NMR dynamics investigations depend to a great extent on the anisotropic nature of the interaction tensors and respectively the type and electronic environment of the observed spins. Here, the quadrupolar couplings, which in general are in the MHz range, determine an intrinsic timescale of 10^{-6} s, with the relatively small deutron quadrupole coupling being an exception - 10^{-5} s. Considering the most common dipolar couplings between spin-1/2 nuclei - ^{1}H-^{1}H and ^{1}H-^{13}C in CH, CH_2 and CH_3 groups (where the spin geometry is known) and respectively the values are *ca.* 15 and 21 kHz, the timescale of the interaction is again 10^{-5} s. If the dominating interaction is the chemical shift then timescales in the order of μs should be considered.

All methods discussed so far deal with microscopic properties of the system under investigation, i.e. either molecular or segmental motions. These are also the dominant processes for dielectric spectroscopy. The range of correlation times covered by the method is significant – practically, depending on the applied AC field the whole range of molecular motions can be investigated (excluding only a narrow frequency range close to the field frequency, which modulates the dielectric constant).

Chapter 5. Packing and dynamics of liquid-crystalline hexasubsituted hexa-*peri*-hexabenzocoronenes (HBCs)

5.1. Introduction to discotic liquid crystals

The liquid-crystalline state is defined as a mesomorphic state exhibiting long-range orientational order and either no or only partial positional order. Hence, it is an intermediate state of order between a liquid (completely disordered) and a crystal (having both long-range orientational and positional order). The liquid-crystalline state is formed by either heating a solid or cooling an isotropic liquid (thermotropic LC state), or by dissolving an amphiphilic solid in an appropriate solvent and conditions (lyotropic LC state). The thermotropic liquid-crystals typically have a stiff aromatic core with flexible side-chains attached, though examples are known of mesogens with stiff periphery and flexible core, consisting of intraanually oriented chains[63,64]. Depending on their shape, the mesogens can be divided into calamitic (rod-like shape) and discotic (disc-like shape).

Since the discovery of discotic liquid crystals (DLCs) and their columnar phases by Chandrasekhar[65] in 1977, a lot of scientific interest has been focused on this class of LC materials. The molecules of discotic mesogens typically have six side chains covalently linked directly or via ether, ester, benzoate or thio bridges, to the central aromatic core. The chemical structures of selected discotic mesogen molecules are presented on Figure 5.1.

The mesophase discotic molecules are typically organized into columns that in turn are arranged in characteristic two dimensional arrays. These phases (usually labeled by capital D) are classified according to the symmetry of the 2-dimensional unit cell of the mesophase, and according to the way the molecules are stacked within the columns (Figure 5.2). Thus the indices *h*, *r* and *ob*, refer respectively to hexagonal, rectangular and oblique arrangements of columns, while the letters *o* and *d* refer to phases in which the molecules are ordered or disordered within the columns. Phases, in which the molecular symmetry axis is on average tilted with respect to the columnar axis, are referred to tilted discotics (D_t)[66]. In addition to the columnar phases, a discotic nematic, N_D, phase is known, as well as discotic cholesteric phase N_D*. In the latter case, the side chains contain asymmetric carbon atoms. Clearly, the N_D and D_h phases are uniaxial, while D_r and D_t are biaxial. For determination of the type of LC phase of the mesogens typically optical microscopy and X-ray diffractometry are used.

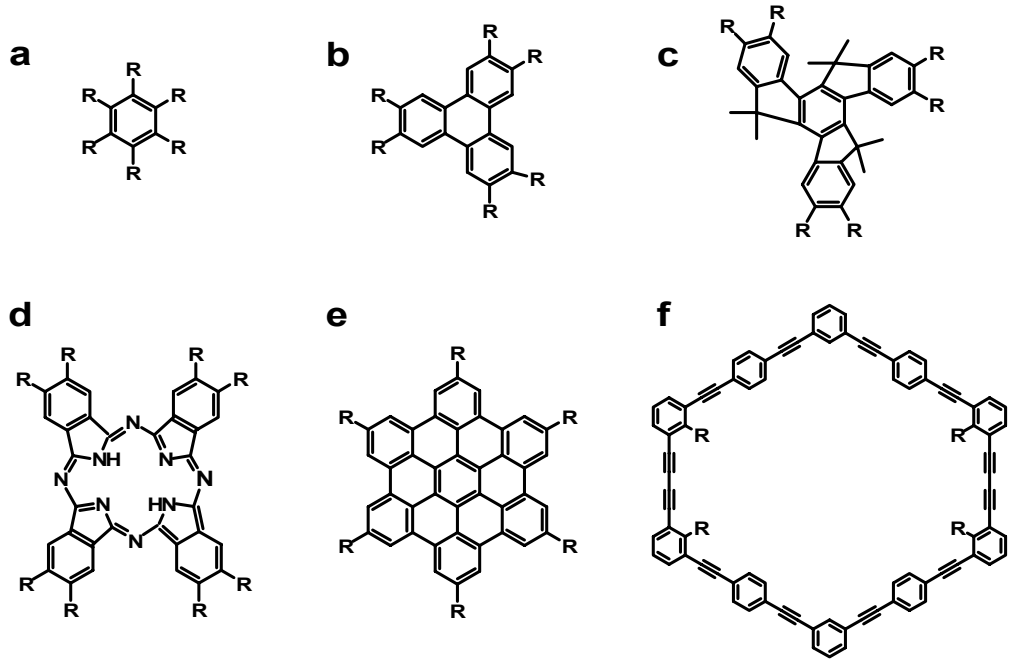

Figure 5.1 Core structures of discotic mesogen molecules – benzene (a), triphenylene (b), truxene (c), phthalocyanine (d), hexa-peri-hexabenzocoronene (e) and phenylacetylene macrocycles (f)

Discotic liquid crystals are considered potential candidates for a variety of device applications, including photovoltaics (solar cells, field effect transistors), light emitting diodes (LEDs) and xerography. In search of the most favorable physical and optoelectronic properties investigations have been performed on different classes of DLCs such as triphenylenes, phthalocyanines, and hexa-*peri*-hexabenzocoronenes (HBCs)[67, 68]. Other stacked liquid-crystalline compounds as dibenzopyrenes, perylenes[69], oligo(p-phenylenevinylenes)[70,71] have also been considered promising candidates for devices.

The HBCs (Figure 5.1 e) belong to the class of large polyaromatic hydrocarbons and are recognized for their stable mesophases over large temperature ranges, high thermal and photochemical stability and high charge carrier mobilities along the columnular axis (1.13 $cm^2V^{-1}s^{-1}$)[72]. Modifying or fine-tuning these properties is achieved by making slight changes in the structures of the liquid crystalline discotic molecules, i.e. varying the length of the alkyl chains or introducing branches[73,74], introducing groups capable of hydrogen bonding or enlarging the aromatic system[75]. Thus, the natural forces existing between the molecules, namely π-π stacking, hydrogen bonding, ionic interactions[76], van der Waals forces, take effect and cause self-assembly.

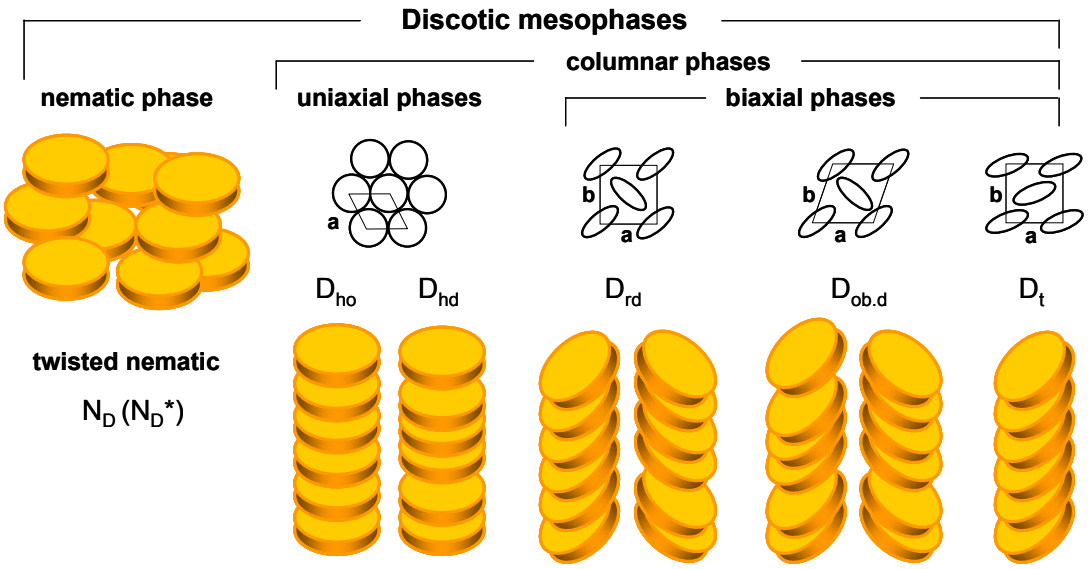

Figure 5.2 Schematic diagrams, and structures of the two dimensional unit cells, of some discotic mesophases

5.2. Overview of the solid state NMR studies on HBC derivatives

In the solid (crystalline) state, the HBC discotic molecules stack one above the other forming columns. In the columns, the discs are tilted with respect to the columnar axis (and displaced one relative to its neighbours), this arrangement being referred to as the "herringbone" packing arrangement (Figure 5.3). It should be noted that such type of packing is observed only in HBC molecules with symmetrically substituted cores, where the alkyl chains contain more than four carbon atoms and no additional functional groups. The enlargement of the aromatic system (introducing as substituents phenyl rings – e.g. HBC-Ph-C12) or having an asymmetric substitution (four or five alkyl chains and electron-donor moiety(s)) results in disc planarity[10] or respectively helical disc arrangement[77] in the columns.

The "herringbone" packing arrangement of the HBC discs leads to a different shielding of the aromatic "bay" protons, due to the different degrees to which they experience the ring currents of the neighboring aromatic systems, and respectively to different ^{1}H chemical shifts[78] of the chemically equivalent aromatic protons (Figure 5.3). Thus, in the ^{1}H solid state NMR spectra three characteristic resonances in the range of 5.5 - 8.5 ppm are observed[79]. In a solution or melt, these packing effects are not present and the HBC molecules tumble isotropically (or in concentrated solutions still stack together forming

columns, but rotate fast about the molecular axis of symmetry) so the three resonances merge into one. The same is also valid for liquid-crystalline HBC derivatives in the mesophase, where though the discs are still organized in columns only one resonance of the aromatic protons is observed due to the averaging of the anisotropic shielding interactions resulting from the fast uniaxial rotation around the columnar axis[80].

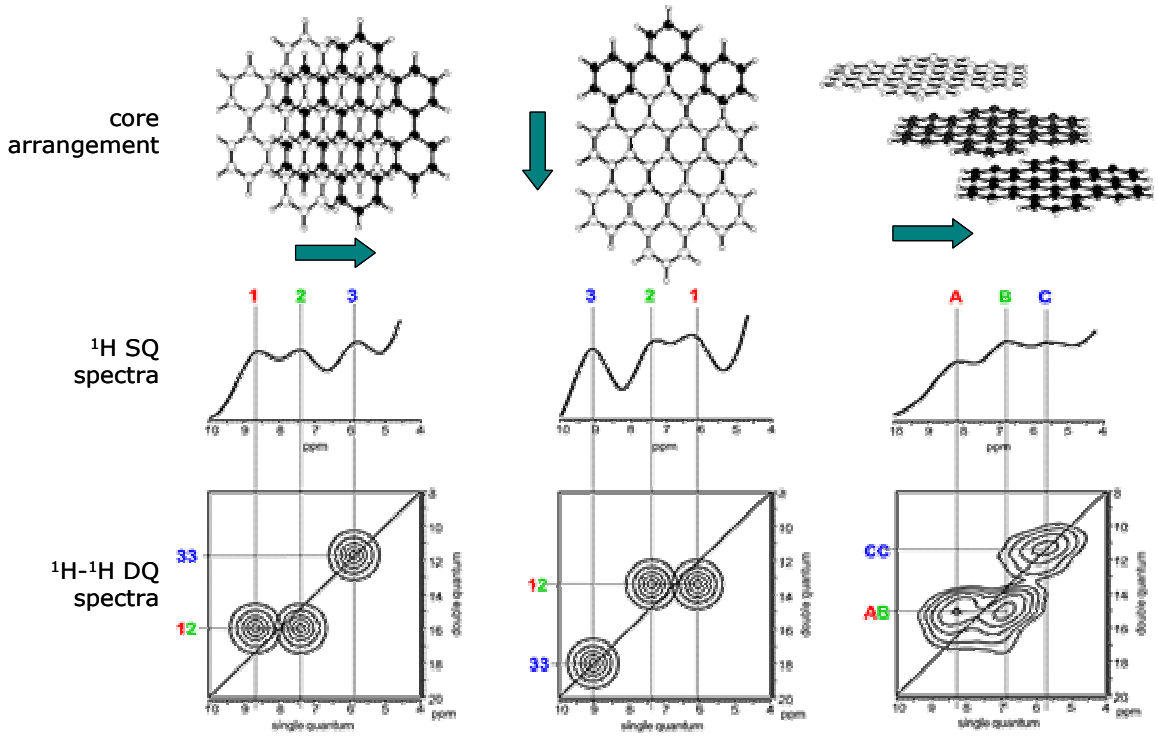

Figure 5.3 Packing of the HBC cores from the ^{1}H SQ and DQ spectra. Adapted from [Ochsenfeld et al][81]

^{1}H DQ solid state NMR under MAS conditions has been successfully applied as a tool to investigate the packing arrangement of HBC mesogens in their crystalline state[82]. The basic principle underlying the DQ NMR approach is exploitation of proton dipolar couplings for the generation of DQ coherences. The observation of such coherences implies sufficient dipolar coupling and provides detailed information about the internuclear proximities between the respective protons involved in the generation of the coherence. The same DQ technique has also been used to study hydrogen bonds and hydrogen bonded aggregates in HBC derivatives[83]. In the cases, where the fast molecular motions of long alkyl chains, esp. in the liquid-crystalline state, caused spectral distortions and signal loss, WATERGATE peak suppression technique has been applied to unravel the influence of the hydrogen bonding on

the aromatic π-π interactions[84]. Additional information concerning the segmental mobilities of the investigated systems can be acquired by recording spinning-sidebands patterns, where through the measured homonuclear dipolar couplings, it is possible to get valuable information about segmental dynamics and the distances between dipolar coupled protons[85].

Furthermore, heteronuclear ^{13}C-^{1}H recoupling NMR experiments, like REREDOR[86], REPT-HDOR[87] or REPT-HSQC[88], that significantly benefit from the better resolution of the ^{13}C spectra, have been developed, by means of which internuclear distances or angles are accessible with high accuracy[89]. Such methods have successfully been applied to the HBC systems either to correlate proton-carbon chemical shifts of the respective nuclei situated in close proximity or to evaluate the strength of the dipolar coupling constant of the pairs via recording and analyzing spinning sideband patterns. The measured effective dipolar coupling constants are then interpreted in terms of local dynamic order parameters, S, given in the form of the second order Legendre polynomial[51] and commonly expressed as the ratio of the measured value of the dipolar coupling constant to the coupling of a rigid pair. These are used to evaluate the site-specific fast molecular dynamics of the investigated HBC derivatives.

The slow molecular dynamics of HBC-C_{12} and HBC-Ph-C_{12} derivatives[90] has also been a subject of investigation by applying the solid state NMR CODEX experiment[91]. Reorientations (60° (or 120°) jumps about the molecular axis of symmetry) in the ms timescale have been observed for the liquid-crystalline HBC-Ph-C_{12} in its room-temperature phase. At the same time the HBC-C_{12} derivative does not experience these reorientational jumps, which is attributed to the high degree of order in the crystalline state. The conclusion that the reported slow molecular dynamics of the investigated HBC-Ph-C_{12} derivative might improve the self-healing of the columnar packing crucial in the long term device performance is somewhat tantalizing as the same is equally valid in the opposite case (especially if an alignment processing technique as a part of the technological process of device preparation is carried out).

Such solid state NMR techniques in combination with other characterization methods, like DSC, optical microscopy, X-ray scattering and dielectric spectroscopy provide concise information about the structure, order and dynamics of the investigated HBC compounds.

5.3. Solid state NMR studies on the effect of chain branching

As already discussed above, the hexa-peri-hexabenzocoronenes (HBCs) are known to form thermotropic columnar liquid crystalline mesophases over exceptionally broad temperature ranges depending on the type, number and functionality of the side chains attached. The HBC disc-shaped molecules stack one above the other mostly due to π–interactions. The columns thus formed, as the aromatic cores, being a hole-transporting media (if not further modified), with the flexible side-chains, being practically insulators, may serve as a good example of the so-called organic nano-wires. In addition, the very high one-dimensional charge carrier mobility, reaching values of 1.13 $cm^2V^{-1}s^{-1}$ for some representatives of the hexa-*peri*-hexabenzocoronenes[92], combined with good processability, are of particular interest for potential applications in field-effect transistors (FETs) and photovoltaics (solar cells). The influence of the length, respectively the spatial requirements of three HBC derivatives with branched side-chains ($C_{6,2}$, $C_{10,6}$ and $C_{14,10}$) on the columnar stacking and core dynamics (Figure 5.1), was investigated by applying different solid state NMR recoupling techniques.

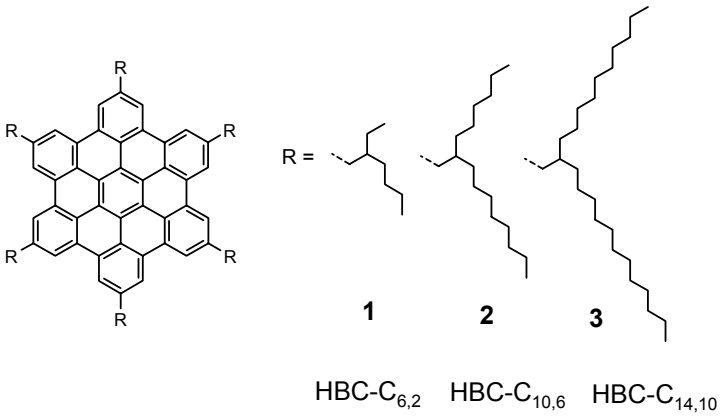

Figure 5.4 Chemical structures of HBC-$C_{6,2}$ **1**, HBC-$C_{10,6}$ **2** and HBC-$C_{14,10}$ **3**

The interest in these compounds was determined by their high ability for self-organization and the remarkably good solubility in organic solvents, which is a prerequisite for improved purification and solution processing. In addition, the low melting temperatures of the HBC derivatives allow the zone casting being an alternative processing technique to achieve long-range homeotropic alignment.

5.3.1. Thermal behaviour

The thermal behavior was determined for all three compounds HBC-$C_{6,2}$ **1**, HBC-$C_{10,6}$ **2** and HBC-$C_{14,10}$ **3** by using differential scanning calorimetry (DSC) in the temperature range from -150 °C to 220°C (10 °C/min) (Figure 5.5), whereby the phase characterization was based on results from polarized optical microscopy (POM), solid-state NMR and X-ray diffraction. As expected, a strong influence of the alkyl substituents on the thermal behavior (Table 5.1) and molecular dynamics (to be discussed in the solid state NMR part) was observed.

HBC-$C_{10,6}$ **2** and HBC-$C_{14,10}$ **3** were considered as "plastic crystalline" due to their plastic deformation and increased molecular dynamics at room temperature in comparison to crystalline materials such as HBC-$C_{6,2}$ **1**. Additionally HBC-$C_{14,10}$ exhibited increased side chain dynamics, confirming this consideration. HBC-$C_{6,2}$ **1** and HBC-$C_{10,6}$ **2** entered the liquid crystalline (LC) state at 97 °C and 24 °C, respectively, whereas HBC-$C_{14,10}$ **3** showed a phase transition directly from the plastic crystalline phase to the isotropic state.

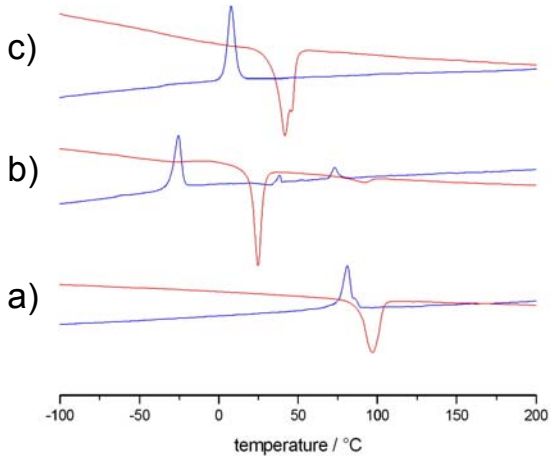

Figure 5.5 DSC traces for a) HBC-$C_{6,2}$, b) HBC-$C_{10,6}$, c) HBC-$C_{14,10,}$, (blue - first cooling, red - second heating curve)

The observed peak splitting prior the isotropization temperature of **3** might be an indication for a relatively narrow liquid crystalline range. By polarized optical microscopy (POM), HBC-$C_{6,2}$ **1** was entering its isotropic state at *ca*. 420 °C. During heating, HBC-$C_{10,6}$

2 showed only a single transition to the isotropic phase at 93 °C, which was in contrast to the cooling cycle, where two exothermic peaks appeared at 73 °C and 45 °C.

Sample	Temperature / °C	Enthalpy / Jg^{-1}	Phase transition
HBC-$C_{6,2}$ **1**	97 (81)	21.4 (17.3)	C_r – Col_d
	420 (380)*	–	Col_d – I
HBC-$C_{10,6}$ **2**	24 (-26)	26.1 (16.4)	Col_p – Col_d
	93 (73, 45)	2.3 (2.6, 1.0)	Col_d – I
HBC-$C_{14,10}$ **3**	46 (7)	33.4 (32.2)	Col_p – I

Table 5.1 Thermal characterization for the investigated dove-tailed HBC derivatives **1** – **3**. Abbreviations: C_r = crystalline phase, Col_p = plastic crystalline, Col_d = columnar disordered liquid crystalline, I = isotropic phase. Brackets indicate values during cooling (*above thermal decomposition, assigned under the POM by rapid heating).

5.3.2. Solid state NMR

Based on the thermal behaviour of the dove-tailed HBC derivatives solid state NMR and WAXS spectroscopy have been performed in parallel to unravel the packing of the compounds in the solid and liquid-crystalline phases. Additionally, site-specific molecular dynamics study was conducted in the respective thermal phases for all the compounds and the results presented and discussed below.

5.3.2.1. Solid (crystalline) state - packing

One-dimensional ^{1}H MAS NMR spectra

Figure 5.6 shows the ^{1}H MAS NMR spectra of the three branched chain HBC derivatives, recorded at 25 kHz magic angle spinning and ^{1}H Larmor frequency of 700.1 MHz. All spectra were recorded using the standard MAS bearing gas set-up – however, it is important to note that the large frictional heating effects associated with the fast MAS lead to significant sample heating. The effective sample temperatures have been corrected by a known procedure for these frictional heating effects[93]. As presented above, the different length of the branched alkyl chains results in different mesophase transition temperatures – the molecules with longer side-chains have lower LC transition temperature and *vice versa*.

To investigate the packing and dynamics of the three HBC derivatives in the solid state sample cooling was needed in the cases of the derivatives with longer chains, i.e. HBC-$C_{10,6}$ and HBC-$C_{14,10}$. Thus, the effective sample temperatures for the compounds were respectively – 85°C (HBC-$_{C6,2}$ **1**), 10°C (HBC-$C_{10,6}$ **2**) and 16°C (HBC-$C_{14,10}$ **3**). At these conditions, the compounds were in their solid states (as stated earlier – crystalline for **1** and plastic-crystalline for **2** and **3**). Comparing the spectral widths, in particular for the dominant ^{1}H high-field aliphatic peaks (1247 Hz for HBC-$C_{6,2}$; 1309 Hz for HBC-$C_{10,6}$; 1152 Hz for HBC-$C_{14,10}$), all proton resonances look similarly broad. The fast MAS successfully averages out the CSA interactions in all the cases, however, the network of strong proton dipole-dipole couplings governs the peak full widths at half maximum (FWHM) in the solid state. In addition, inhomogeneous broadening due to the different ^{1}H chemical shifts of the CH, CH_2 and CH_3 protons also contributes to the increased width of the aliphatic peaks.

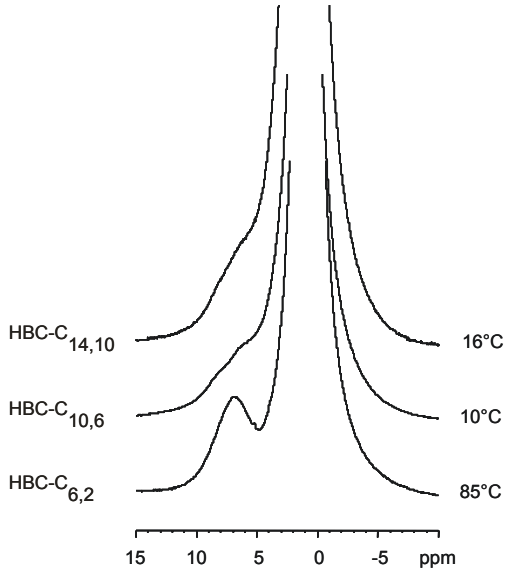

Figure 5.6 ^{1}H NMR spectra of the HBC derivatives recorded at spinning frequency of 25 kHz

The chemical structures (Figure 5.4) of the HBC analogues suggest the existence of one type chemically equivalent aromatic protons. However, in the aromatic regions of the solid state ^{1}H NMR spectra of **2** and **3**, at least two aromatic resonances are clearly resolved, and the resonance of the aromatic protons in the case of compound 1 are characterized by a significant inhomogeneous broadening. Such signal splitting is known to arise from the packing effects of the HBC discotic molecules (see above). To explore the packing of the

HBC derivatives two spectroscopic techniques have been applied in parallel, namely wide angle X-ray scattering (WAXS) and ^{1}H double quantum filtered (DQF) MAS NMR.

One- and Two-Dimensional ^{1}H rotor synchronized DQ MAS NMR spectra of the HBC derivatives

The proton double-quantum filtered spectroscopy has been proven an indispensable tool for investigating the packing in columnar structures like HBCs, triphenylenes[94] and dendrimers[95]. The pulse sequence used to generate proton DQ coherences under magic angle spinning conditions was in this case the BaBa sequence (the one-dimensional proton DFQ BaBa spectra of the HBC analogues are presented on Figure 5.7) due to its simplicity and robustness to power level imperfections.

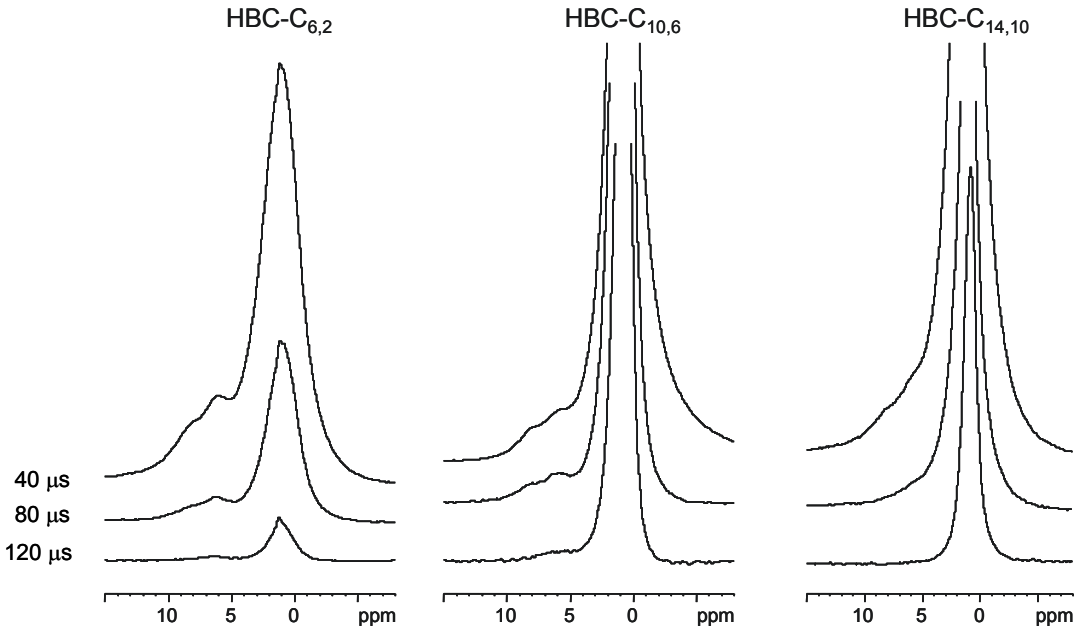

Figure 5.7 ^{1}H-^{1}H DQF BaBa NMR spectra of HBC-$C_{6,2}$ (**1**), HBC-$C_{10,6}$ (**2**) and HBC-$C_{14,10}$ (**3**) in the solid state, recorded at 25 kHz magic angle spinning, recoupling times of 40 μs (1 τ_R), 80 μs (2 τ_R) and 120 μs (4 τ_R) and sample temperatures of 40°C (**1**), 10°C (**2**) and 16°C (**3**).

A requirement for generating coherence between two proton spins is the existence of a sufficient dipolar coupling, which, as discussed in the theory chapter, is a function of the internuclear distance. Therefore, the signal intensity in the DQF spectra is directly proportional to the dipolar coupling strength (reflected in the dipolar coupling constant D^{ij}

between two proton spins i and j) and the recoupling time used in the rotor synchronized experiment (given in integer multiples of the rotor period). In the limit of short excitation/reconversion times, i.e. $D^{ij}.\tau_R<1$, the signal intensity is proportional to $(D^{ij}.\tau_{exc}).(D^{ij}.\tau_{rec})$[37]. Thus, DQ signals can be used as a qualitative, even as semi-quantitative measure for internuclear distances and molecular motion. As seen from the figure, very short recoupling times are needed to excite coherences between the ^{1}H spins, thus the respective dipolar pairs are strongly coupled in the solid state. This implies restricted chain dynamics (excluding the chain ends). Increased recoupling time results in a drop of the signal intensity in all spectra. The dominating peaks in the right-hand corner of the spectra correspond to DQCs among the aliphatic protons – it is evident that in the solid state the CH_2 and CH_3 proton resonances cannot be resolved. The lack of spectral resolution in this case is not crucial, as the aliphatic spectral region does not provide information of the packing of the HBC discs and only a rough estimation of the chain dynamics is possible.

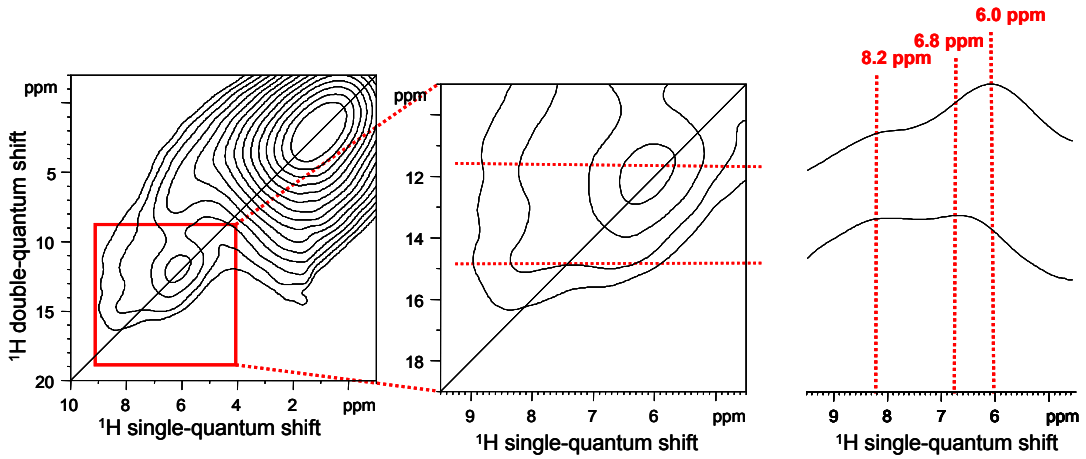

Figure 5.8 2D solid-state ^{1}H-^{1}H double-quantum MAS NMR spectrum of HBC-$C_{6,2}$ (left) with the aromatic region magnified (middle) and two 1D slices cut at 12.0 and 14.8 ppm (right). The experimental conditions were T = 313 K, MAS at 25 kHz, and dipolar recoupling (BaBa sequence) for one rotor period to excite and reconvert the DQ coherences.

Of more interest are the peaks in the left side of the spectra due to DQCs among the aromatic protons. Signal intensity with maxima at *ca.* 6 and 8 ppm is observed (as in the ^{1}H MAS NMR spectra), however, significant peak overlap and insufficient rotor spinning frequency hamper the spectral resolution. The need for better resolution and information about the proximities between ^{1}H dipolar coupled pairs determines the need for introducing

the second dimension in the experiment. So 2D ^{1}H DQ BaBa NMR spectra of compounds **1**, **2** and **3** under 25 kHz spinning were recorded (2D ^{1}H DQ BaBa NMR spectrum of HBC-$C_{6,2}$ is presented on Figure 5.8).

In the DQ dimension, the chemical shift of the signals is correlated with the sum of the shifts of the two nuclei involved in the DQC. Thus, if we consider the DQ signal pattern related with the "herringbone" packing arrangement[81] (Figure 5.3), three resonances in the aromatic spectral region are observed with frequencies (corresponding to the respective chemical shifts) denoted symbolically ω_A, ω_B and ω_C. The presence of two off-diagonal peaks (cross-peaks) provides evidence for a close proximity of two aromatic protons with different chemical shifts (an AB coupled pair) and the respective peaks in the DQ spectrum appear at (ω_A, ω_A+ ω_B) and (ω_A+ ω_B, ω_B). The diagonal peak is an autocorrelation peak due to a coupling between protons with identical chemical shifts (ω_C, $2\omega_C$) - a coupled CC pair. The ratio between the signal intensities of the AB and CC pairs is determined to be 2:1.

The 2D ^{1}H-^{1}H DQ BaBa NMR spectrum (Figure 5.8) of the HBC-C6,2 derivative in its crystalline state shows a close resemblance to the theoretical pattern. One diagonal auto-peak due to a DQC of a coupled pair of protons with the same chemical shift is observed at (6.0, 12.0 ppm) in the aromatic spectral region. Additionally, two cross-peaks, at (6.8, 15.0 ppm) and (8.2, 15.0 ppm) due DQCs between a pair of protons with shifts in the single quantum dimension 6.8 and 8.2 ppm, are present in the same spectral region. Taking into account the very short recoupling time used in the experiment (40 μs), DQ signal intensity would arise from strongly coupled proton pairs in a close proximity. The distance between the aromatic protons situated in the "bays" of the HBC-$C_{6,2}$ is *ca.* 0.2 nm, while the nearest interpair distance (the distance between protons from neighboring discs) is twice as much (0.41 nm). This, indeed, is a confirmation that the observed coherences are between neighboring "bay" protons. The fact that three aromatic resonances are observed when only chemically equivalent protons are present in the structures is an indication of the packing effects of the neighboring aromatic systems. Taking into account that symmetrically substituted HBCs with alkyl chains having no further functionalization, in the crystalline state tend to adopt the "herringbone" columnar arrangement, this particular packing was further considered. A confirmation that indeed the branched chains HBC derivatives adopt tilted disc arrangement in columns was found in the 2D WAXS spectra of extruded fibers of the compounds. Representative WAXS spectra of HBC-$C_{6,2}$ and HBC-$C_{10,6}$ in their crystalline states are shown on Figure 5.9 (**a** and **c**).

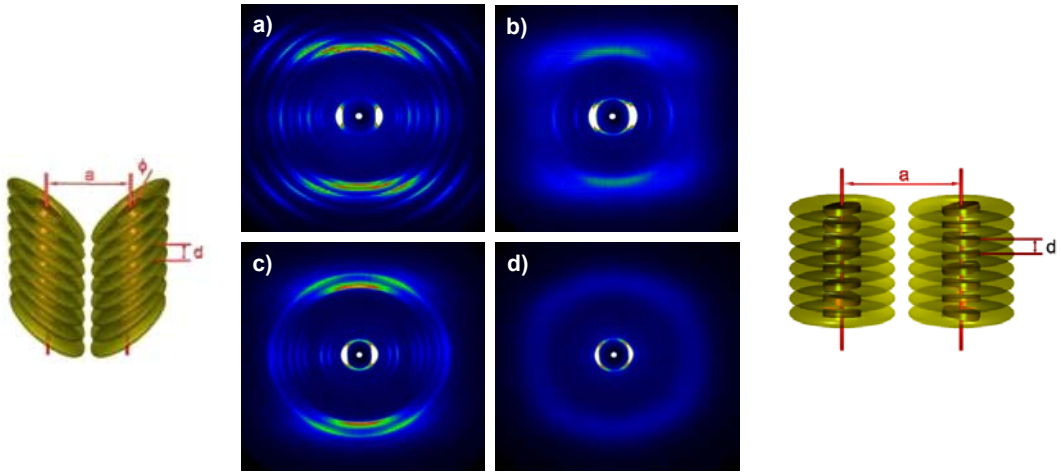

Figure 5.9 2D-WAXS pattern of filament extruded of HBC-$C_{6,2}$ **1 a)** in the crystalline and **b)** in the liquid crystalline phase, and HBC-$C_{10,6}$ **2 c)** in the plastic crystalline and **d)** in the liquid crystalline phase at 60 °C. The 2D-WAXS experiments were conducted by Dr. W. Pisula.

The distinct equatorial reflections in the 2D-WAXS pattern of the compounds suggest a well-ordered supramolecular structure of the macroscopically oriented filaments with columns aligned in the extrusion direction. The large number of higher order reflections implies a high degree of order for the compounds in the crystalline state. The distinct off-meridional reflections indicate an identical tilt of the discotic cores with respect to the columnar axis with an intracolumnar period of 0.48 nm leading to a "herringbone" structure. The tilting disc angles for the HBC derivatives determined from the patterns is *ca.* 40° for the HBC-$C_{6,2}$ and *ca.* 25° for HBC-$C_{10,6}$ and HBC-$C_{14,10}$.

Thus, both ^{1}H DQ NMR and WAXS confirm the formation of the "herringbone" packing disc arrangement of the compounds under investigation in the crystalline state.

5.3.2.2. Solid (crystalline) state – dynamics

The molecular dynamics has been investigated further by analyzing spinning sideband patterns recorded in the ^{13}C-^{1}H REREDOR NMR experiments performed under fast MAS conditions.

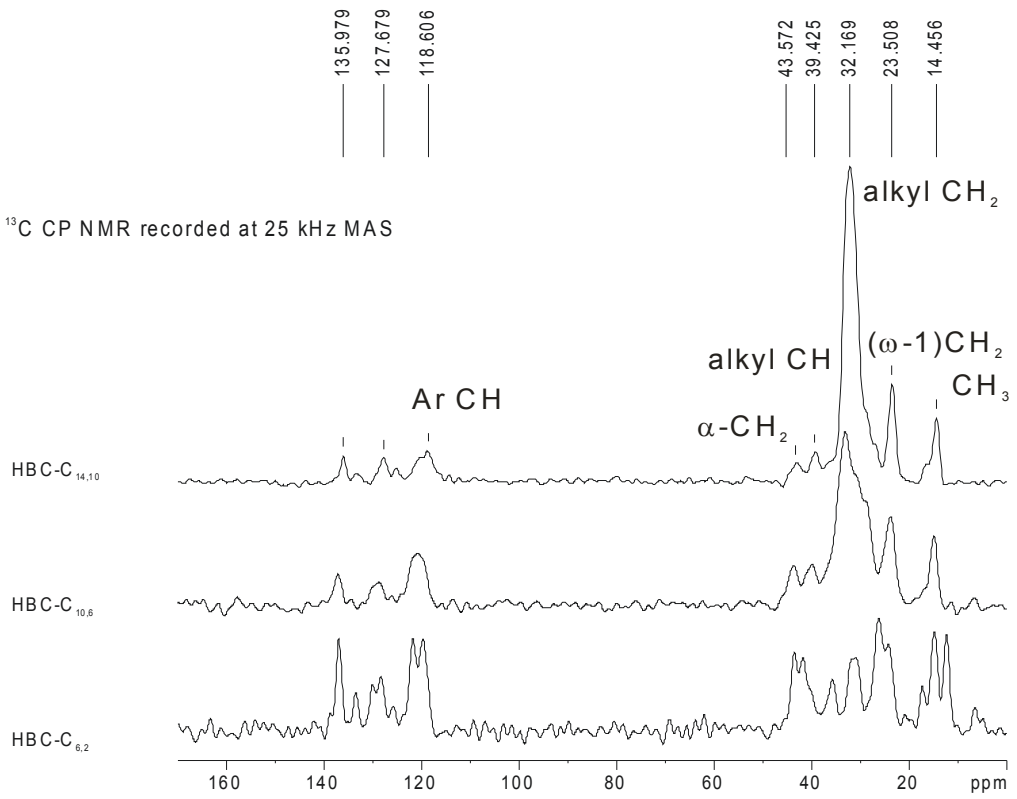

Figure 5.10 **a)** ^{13}C CP spectra of the HBC derivatives recorded at 25 kHz MAS at 40°C (HBC-$C_{6,2}$ **1**), 16°C (HBC-$C_{10,6}$ **2**) and 10°C (HBC-$C_{14,10}$ **3**) in the compounds` crystalline state with the respective signal assignment

Prior to recording spinning sideband patterns, the cross-polarization (CP) ^{1}H-^{13}C NMR experiments under fast MAS conditions were conducted for all the compounds studied, and the ^{13}C resonances were assigned in the respective spectra. In addition, ^{1}H-^{13}C TEDOR recoupling technique was used to estimate semi-quantitatively the ^{1}H-^{13}C dipolar couplings of the CH_n moieties in the HBCs as a function of the recouping time. Additionally, the inexpensive in terms of experimental time 1D technique was used to determine and set correctly the recoupling times needed to generate coherences between the ^{1}H-^{13}C dipolar coupled pairs in the much longer REREDOR experiments. The ^{13}C CP and ^{1}H-^{13}C TEDOR NMR spectra recorded under 25 kHz MAS are presented in Figure 5.10.

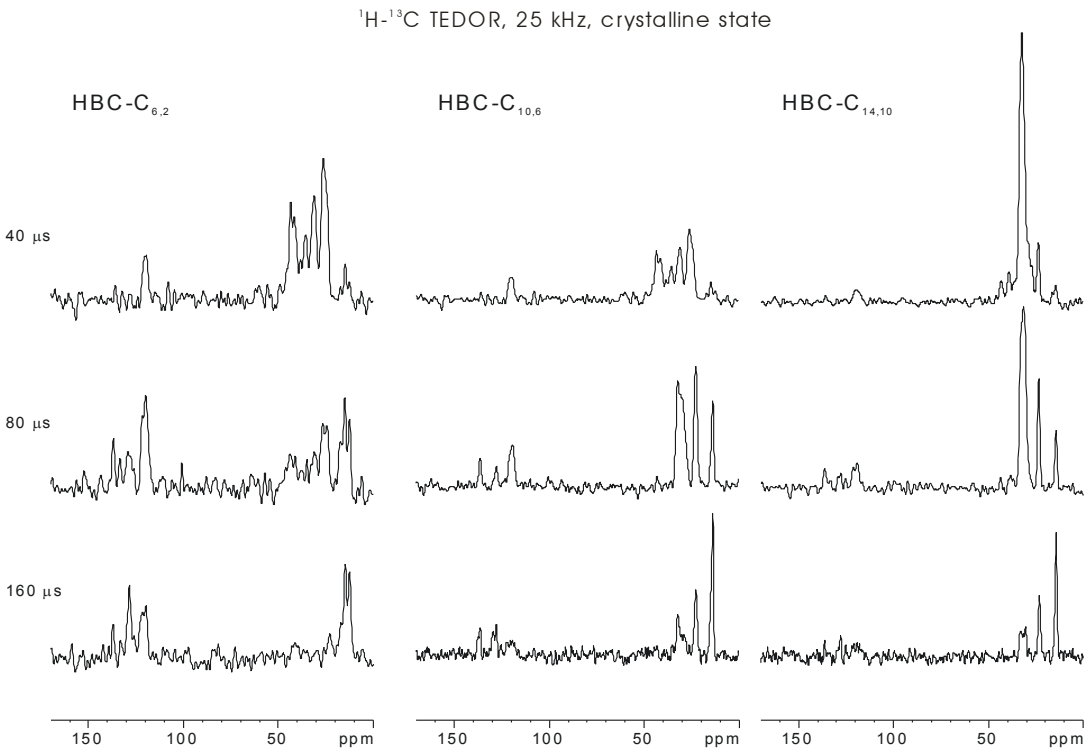

Figure 5.10 **b)** ^{1}H-^{13}C TEDOR (at 40 μs, 80 μs and 120 μs recoupling time) spectra of the HBC-$C_{6,2}$ **1** (T = 40°C), HBC-$C_{10,6}$ **2** (T = 16°C) and HBC-$C_{14,10}$ **3** (T = 10°C), recorded at 25 kHz MAS.

The ^{13}C CP spectra of the HBCs were recorded at 25 kHz sample spinning at the magic angle. A ramped cross-polarization (80-100%) pulse, transferring the polarization from the abundant protons to the low-gamma carbon nuclei, with a contact time duration of 1 ms, was used. The high field peaks (at *ca.* 14 ppm, shaded in yellow) in the ^{13}C CP spectra correspond to the resonance signal due to the terminal methyl groups. Going to lower fields (higher frequencies) consequently are observed the signals of the (ω-1) CH_2 moiety (at *ca.* 23 ppm, shaded in light green) and the dominating signal of the alkyl chain (at *ca.* 30-32 ppm). The resonance of the methyne group, being the branching point of the dove-tailed alkyl chains, is detected at ca. 40 ppm. The signal of the anchoring α-CH_2 group is observed at *ca.* 43 ppm (all aliphatic, excluding the terminal ω– and (ω-1), groups are shaded in dark green).

In the aliphatic spectral region of the ^{13}C spectrum of HBC-$C_{6,2}$ two methyl resonances at 12.4 ppm and 14.8 ppm and a shoulder of the latter peak are observed, contrary to the spectra of the other two homologues. These two resonances arise from the two types of methyl moieties present in the structure of the compound (one of those is at a β-position regarding the branching CH point).

The shoulder of the 14.8 ppm resonance is most probably due to residual solvent present in the sample. In the other HBC compounds, the influence of the branching position is less pronounced, though a broadening of the terminal CH_3 resonance in the ^{13}C spectrum of the HBC-$C_{10,6}$ derivative is observed. In the spectrum of the HBC-$C_{14,10}$ the CH_3 peak is sharp and symmetric due to the pronounced chain mobility (this point will be discussed below).

Two resonance peaks with chemical shifts of 119.7 ppm and 121.7 ppm are observed in the spectral region where the aromatic CH moiety of the HBC-$C_{6,2}$ is expected to appear. Those most probably arise from the packing (it is known that the ring currents influence similarly all nuclei irrespective of their nature (spin type). To address this question ^{1}H-^{13}C transferred echo double resonance (TEDOR) correlation NMR spectroscopic technique was applied.

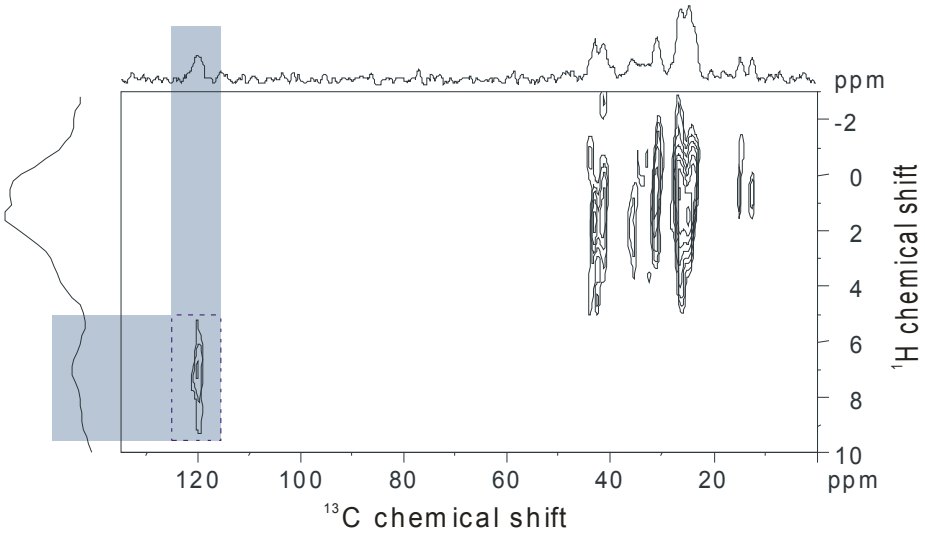

Figure 5.11 ^{1}H-^{13}C 2D TEDOR NMR spectrum of HBC-$C_{6,2}$, recorded at 40 μs recoupling time and 25 kHz spinning at the magic angle – the ^{13}C chemical shift in the direct dimension is correlated with the ^{1}H shift in the indirect dimension.

The 2D TEDOR NMR spectrum was recorded with a short recoupling time (40 μs) to detect only the directly bonded ^{1}H-^{13}C pairs. The ^{13}C signal of the aromatic CH moiety under discussion is observed at 120.7 ppm. Although splitting is not detected, the signal looks broadened, suggesting influence on the chemical shift due to the ring currents of the neighboring aromatic systems. This implies a contact of the 120 ppm carbon with protons with a different chemical shift, arising from the “herringbone” packing.

As already discussed in the theory part, the TEDOR experiment is used not only for assignment purposes in its 2D correlation version, but also for a semi-quantitative estimation of the molecular dynamics in the 1D variant. Particularly useful is the feature that a rigid CH_2 group is detected in the TEDOR spectrum only if less than 60 μs recoupling time is used. Thus, an indirect measure of the mobility of the methylene moieties is possible, following the signal build-up or disappearance of the respective peaks in the spectrum as a function of the recoupling time. The TEDOR spectra of the HBC homologues presented in Figure 5.10 are a nice demonstration of this useful feature. In the aliphatic regions of the spectra of compounds **1**, **2** and **3** the signals of the (ω-1) CH_2 groups (at *ca.* 23-24 ppm), the alkyl chains (signals in the range 28 to 39 ppm) and the anchoring α-CH_2 methylenes (*ca.* 40-42 ppm) are clearly resolved.

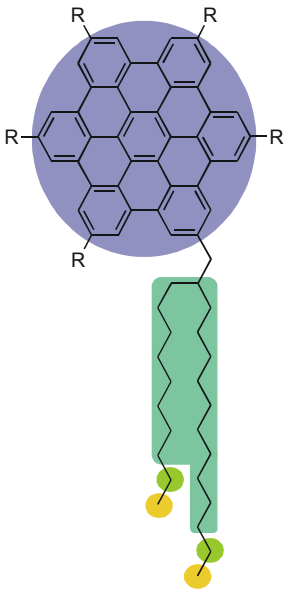

Figure 5.12. Degree of mobility as found by NMR experiments in different parts of the dove-tailed HBC derivatives (the blue colour displays the rigid HBC-core with increasing mobility along the chain to the most mobile regions displayed in yellow). R: dove tail, n: number of carbons in the main chain, m: number of carbons in the β-chain.

In all HBC derivatives under study the signals of the CH_2 moiety directly bonded to the aromatic system disappear for two rotor periods recoupling of the experiment (Figure 5.10), which leads to the conclusion that the anchoring methylene groups, having less degrees of freedom, are rigid. Considering the alkyl chains, where the superposition of the chemical shifts of all CH_2 groups contributing to the signal, hampers the site-specific resolution and thus the site-specific mobility evaluation, an estimation of the average chain mobility is performed. Obviously, the short $C_{6,2}$ chain is the least mobile as after 2 rotor periods recoupling (80 μs) in the rotor synchronized experiment its signal disappears.

The same is not valid for the longer $C_{10,6}$ and $C_{14,10}$ chains, where even after 120 μs recoupling a signal, originating from mobile CH_2 groups, is observed in the spectrum. The same phenomenon occurs at the highly mobile chain ends. Situated closer to the branching point, the (ω-1) CH_2 group in the HBC-$C_{6,2}$ is less mobile compared to the same moiety in the other two HBCs. Thus, a mobility gradient starting from the rigid core towards the chain end is expected for all the compounds.

Quantitative evaluation of the HBC molecular dynamics is achieved by means of recording and analyzing REREDOR spinning sideband patterns, from which the ^1H-^{13}C effective dipolar coupling constants are extracted. The latter are related to the coupling of a rigid pair to yield local dynamic order parameters, S, which are expressed in the form of the second order Legendre polynomial, i.e. $S \sim (3\cos^2\theta-1)$.

Here, S (equation 5.1) represents the residual motional anisotropy of a given molecular segment.

$$S = D_{exp} / D_{rigid}, \qquad (5.1)$$

where D_{exp} is the experimentally measured ^1H-^{13}C dipolar coupling constant of a CH_n group, and D_{rigid} is the reference ^1H-^{13}C coupling constant of the same moiety but in a totally rigid state. Hence, S = 1.0 stands for segments which are rigid on the timescale of the NMR experiment (i.e., ~ 1 ms), excluding the fast rotation of methyl groups around their threefold symmetry axis.

For alkyl sidechains attached to rigid cores or backbones, in general, a mobility gradient is expected with the α-CH_2 group being almost as rigid as the core, and the ω-CH_3 group being most mobile. Since the exact geometry of the motion of the side-chains is not known, it is instructive to relate the local dynamic order parameter S, i.e., the degree of segmental mobility, with a Gaussian distribution of orientations (i.e., angles) which the segment is assumed to adopt in the course of its motion.

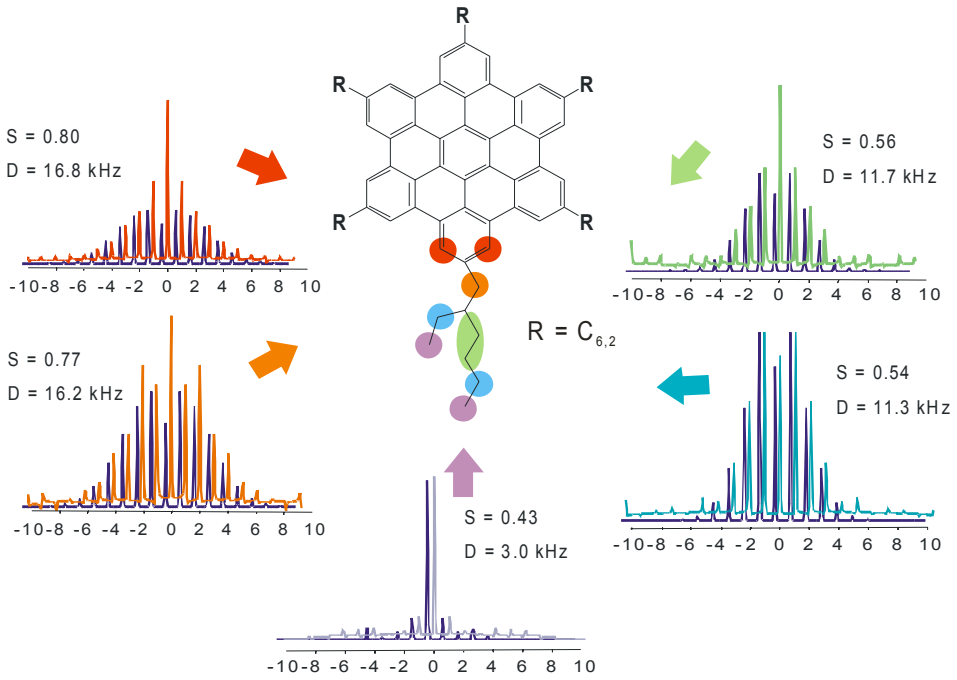

Figure 5.13 HBC-$C_{6,2}$, REREDOR sideband patterns, recorded at 25 kHz MAS, 80 µs recoupling time and 57°C effective sample temperature. The corresponding ^{1}H-^{13}C dipolar coupling constants with the related dynamic order parameters for the color-coded chemical sites are also presented.

The higher its mobility (i.e., $S \rightarrow 0$), the broader is the dynamic orientation distribution (i.e., $\Delta\theta \rightarrow 90°$); conversely, the lower its mobility (i.e., $S \rightarrow 1$), the narrower is the orientation distribution (i.e., $\Delta\theta \rightarrow 0°$).

HBC-derivative	D_{HC} [kHz] → core rigidity S	D_{HC} [kHz] → alkyl chain rigidity S		
		alkyl chain	ω-1 CH_2	ω-CH_3
HBC-$C_{6,2}$	16.5 → 0.80	14.5 → 0.70	13.0 → 0.60	3.2 → 0.50
HBC-$C_{10,6}$	19.5 → 0.93	14.0 → 0.67	13.9 → 0.66	4.5 → 0.65
HBC-$C_{14,10}$	18.5 → 0.88	9.5 → 0.45	4.0 → 0.20	1.2 → 0.15

Table 5.2 Solid-state ^{1}H-^{13}C dipolar coupling constants D_{HC} and dynamic order parameters S of individual molecular segments of the HBC derivatives, as determined from ^{1}H-^{13}C NMR REREDOR sidebands patterns. The experimental conditions were T = 6 ÷ 16°C, MAS at 25 kHz (for HBC-$C_{6,2}$ and HBC-$C_{14,10}$) and 17.5 kHz (for HBC-$C_{10,6}$), and an overall of two rotor periods dipolar recoupling.

For the corresponding molecular segments of HBC-$C_{6,2}$ and HBC-$C_{10,6}$, similar dynamic order parameters are found in solid state (see Table 5.2), which confirms the

expectations of a relatively rigid aromatic core and more mobile side-chains. In the case of HBC-$C_{6,2}$, the alkyl chain segment mobility gradually increases from the anchoring point ($S \sim 0.7$) at the core towards the chain ends ($S \sim 0.5$, see also Figure 5.12), while a more uniform chain mobility is determined for HBC-$C_{10,6}$ with a similar local dynamic order parameter $S \sim 0.65$ along the chain. For HBC-$C_{14,10}$, again a pronounced mobility gradient is found, but the chain mobility ($S \sim 0.5 \rightarrow 0.15$ at 16°C), as a whole, is significantly higher than in HBC-$C_{10,6}$ and HBC-$C_{6,2}$. This lack of order in the solid state can be related to the absence of a well-defined and stable mesophase in this material and is attributed to the spatial requirements of the bulky $C_{14,10}$ chains.

5.3.3.3. Liquid-crystalline state – packing and dynamics

When heating the samples to the respective transition temperatures into the mesophase, the HBC molecules undergo a reorientation from the tilted to a planar arrangement and start a rapid rotation around their columnar axis. In the ^{1}H MAS spectra, this transition manifests itself in the narrowing of the resonance lines. Moreover, the three distinct aromatic peaks observed in the solid state merge into a single aromatic ^{1}H resonance. This is also clearly observed in the ^{1}H-^{1}H 2D DQ BaBa spectrum recorded with 80 μs excitation time and 25 kHz spinning at the magic angle (Figure 5.13). The only aromatic peak detected is at (7.0 ppm, 14.0 pm) and its chemical shift in the direct spectral dimension has the average value of the shifts found in the crystalline state. Additionally, the off-diagonal peaks at (1 ppm, 8 ppm) and (7 ppm, 8 ppm) reveal the contact/coupling between the alkyl and aromatic protons.

When turning to the liquid-crystalline state, the fast disc rotation decreases the ^{1}H-^{13}C dipole-dipole couplings in the aromatic CH groups by a factor of two, as long as the rotation axis coinsides the columnar axis and both are perpendicular to the HBC core plane[96]. In addition, out-of-plane disc motions are also possible, which further reduce the dynamic order parameters of the core CH segments.

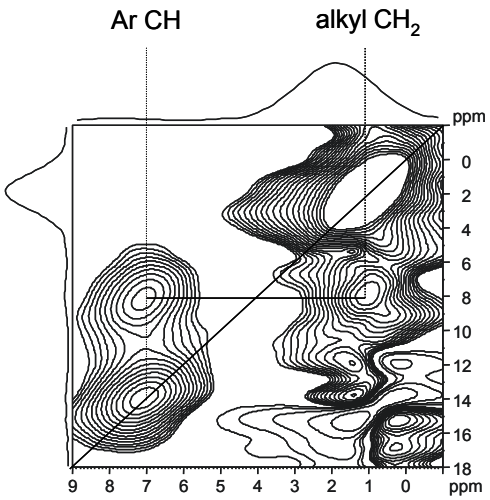

Figure 5.13 ^{1}H-^{1}H 2D DQ BaBa NMR spectrum recorded using 80 ms recoupling time and 25 kHz spinning at the magic angle

By relating the determined core order parameters S to the "ideal" value S = 0.5, representing a perfect in-plane rotation, the mean out-of-plane excursion of the cores can be estimated. In Table 5.3, these excursion angles are given for the liquid-crystalline phases of HBC-$C_{6,2}$ and HBC-$C_{10,6}$, together with the dynamic order parameters of the segments. As the mobility of the system increases, dipolar recoupling needs to be applied for longer periods in order to generate meaningful REREDOR sideband patterns.

Comparing the dynamic order parameter of the cores in the LC phase, HBC-$C_{10,6}$ exhibits the most stable disc rotation with a maximum out-of-plane excursion of ~ 24°. Thus, the π-π stacking of the HBC-$C_{10,6}$ columns is affected, but not disrupted by the steric requirements of the quickly moving alkyl chains (otherwise the compound should have be in the molten state). Hence, despite the fast rotation of the discs with their dove-tailed sidechains, the columnar order is preserved. This makes HBC-$C_{10,6}$ the most promising candidate among the investigated compounds in terms of charge carrier mobility for applications in devices. At the same time, HBC-$C_{6,2}$ exhibits a less stable rotation, as reflected by ~ 42° out-of-plane excursion, while HBC-$C_{14,10}$ undergoes a practically direct transition from solid phase into the isotropic melt, such that there is no well-defined liquid-crystalline phase to be studied.

HBC-derivative	D_{HC} [kHz] → core rigidity S	D_{HC} [kHz] → alkyl chain rigidity S			out-of-plane excursion
		Alkyl chain	ω-1 CH_2	ω-CH_3	
HBC-$C_{6,2}$	4.8 → 0.32	4.2 → 0.20	2.8 → 0.15	0.7 → 0.8	42°
HBC-$C_{10,6}$	6.8 → 0.45	1 … 2.5 → 0.05 … 0.10			24°
HBC-$C_{14,10}$	melt				→ 90°

Table 5.3 Liquid-crystalline state ^{1}H-^{13}C dipolar coupling constants D_{HC} and dynamic order parameters S of individual molecular segments of the HBC derivatives, as determined from ^{1}H-^{13}C NMR REREDOR sidebands patterns. The experimental conditions were T = 361 K and four rotor periods recoupling for HBC-$C_{10,6}$ and T = 410 K and eight rotor periods recoupling for HBC-$C_{6,2}$, with MAS at 12.5 kHz.

5.4. Conclusions

1. The introduction of the bulky branched alkyl chains of different length attached to the hexa-*peri*-hexabenzocoronene core allows tuning the compounds thermal behavior and solubility over a broad range. The key to modulate the intermolecular interactions is actually the position of the branching point being in close proximity to the aromatic core. 2. In terms of packing the influence of the length of the branched chains is expressed by the change in the "planarity" order parameter for the core (as detected by solid state NMR) to higher values – from 64% for the HBC-$C_{6,2}$ to 90% for the HBC-$C_{10,6}$ analogue. In the mesophase the fast dynamics of the molten alkyl chains result in increased columnar disorder, and thus to hindrance of the one-dimensional migration of the charge carriers along the columnar structures.

3. The HBC-$C_{10,6}$ derivative seems most promising for applications in devices, as the disorder introduced by the spatial requirements of the $C_{10,6}$ chains to enable processing, is insufficient to break the π-π interactions responsible for the columnar packing. In addition, the compound exhibits the best charge carrier mobility observed in a non-crystalline HBC derivative. Characteristic features of the HBC analogue both in the solid and LC state are uniform chain dynamics as determined by solid state NMR recoupling methods as well as stable disc rotation in the mesophase. So, NMR techniques can be used to evaluate the supramolecular order and dynamics, and thus help to direct the synthetic efforts for novel columnar derivatives with improved properties.

Chapter 6. Supramolecular Order and Dynamics of Phthalocyanine Octaesters

6.1. Introduction

As discussed in chapter 5 the high values of intrinsic charge carrier mobility of stacked discotic hexa-*peri*-hexabenzocoronenes were prerequisites for their successful implementation in photovoltaic devices[97] and field-effect transistors[98,99]. However, difficulties in the synthesis (larger batch quantities than a hundred milligrams are not synthetically feasible) and especially the purification of these promising materials, limit the interest in HBCs more to scientific, rather than industrial purposes and application.

Thus, the class of phthalocyanines (Pcs), having significant industrial application in different areas, was the natural continuation of the studies on functional columnar materials in terms of supramolecular organization by means of solid state NMR. Phthalocyanines (actually metal containing phthalocyanines) are a leading class of colorants (dyes and pigments) due to their strong absorption of light combined with extraordinary thermal and photostability[100]. In addition, they have been investigated for potential use in many other fields including catalysis[101], chemical sensors[102], non-linear optical materials, membranes[103], ink-jet printing[104], electrophotography[105], and photodynamic therapy.

The chemical structure of the phthalocyanine molecule with two protons situated inside in a plain of a large aromatic system, thus experiencing strong ring current effects, has attracted the attention of NMR spectroscopists. Although this class of compounds has been known for nearly a century[104], and numerous X-ray studies on different metal-free or metal substituted, and differently functionalized Pc derivatives have been performed[106], to the best of our knowledge no solid state NMR investigation on the packing effects in these systems by recoupling techniques has been reported so far.

However, interesting solid state NMR studies on the rate of proton migration in porphyrin and related derivatives by ^{13}C CP MAS NMR spectroscopy have been performed by Freedman et al[107], as well as profound investigations of the solid state kinetic isotope effect in deuterated samples have been reported by Limbach and coworkers[108,109]. In addition, ^{15}N NMR spectroscopy on Pc derivatives at low temperatures and magic angle spinning conditions has been conducted[110], aiming (indirectly) to understand the dynamic behavior of the inner core protons.

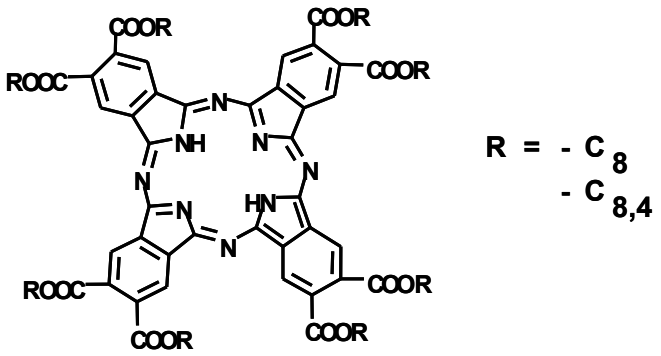

Figure 6.1 Chemical structures of phthalocyanine octaester (C_8 linear and $C_{8,4}$ branched chain) derivatives.

This chapter reports on a study of the columnar packing and molecular dynamics of two liquid-crystalline metal-free phthalocyanine octaester (a linear chain C_8 and a branched chain $C_{8,4}$) derivatives (chemical structures presented on Figure 6.1). The two Pc octaesters, possessing eight electron withdrawing carboxylic groups directly attached to the Pc core, have been designed as *n*-type semiconducting discotic mesogens.[111]

6.2. Thermal Behaviuor

Prior to the NMR experiments, a differential scanning calorimetric study at a heating/cooling rate of 10°C/min has been carried out, providing the thermotropic properties of the Pc octaesters. The phase transitions are presented on Figure 8.2.

As reported in literature[112],octa-substituted phthalocyanines with linear *n*-alkyl substituents form columnar liquid crystalline phases, in an exceptionally wide temperature range (above -40°C, no isotropization until 300°C). For the linear C8 chain derivative the previously reported phase behavior is incorrect most probably due to insufficient purity of the compound. The DSC trace of this phthalocyanine analogue (Figure 6.2 **a**) shows a clear transition at heating at 82°C (transition enthalpy 87.1 kJ/mol). The transition is from crystalline to liquid-crystalline phase, as both phases are further characterized by ^{1}H, ^{13}C CP, ^{1}H-^{13}C TEDOR and ^{1}H-^{13}C REPT-HDOR solid-state MAS NMR and 2D WAXS experiments. The results presented are in agreement with recent reports[111] on polarized optical microscopy and X-ray diffraction studies on the phase behavior of PcH2-$(COOC_8)_8$. On cooling from the mesophase the phthalocyanine molecules crystallize at 0°C. The large hysteresis (ΔT = 82°C) indicates that the bulky phthalocyanine cores are involved in the

transition. Unlike other discotic molecules like HBCs, where such hysteresis was attributed to the slow core reorientation process[113-115], here the seizing of the fast disc rotation is related with the transition. At the same time, the terminal groups of the alkyl chains remain mobile, as determined by the solid state NMR dynamics investigations, at the experimental temperatures.

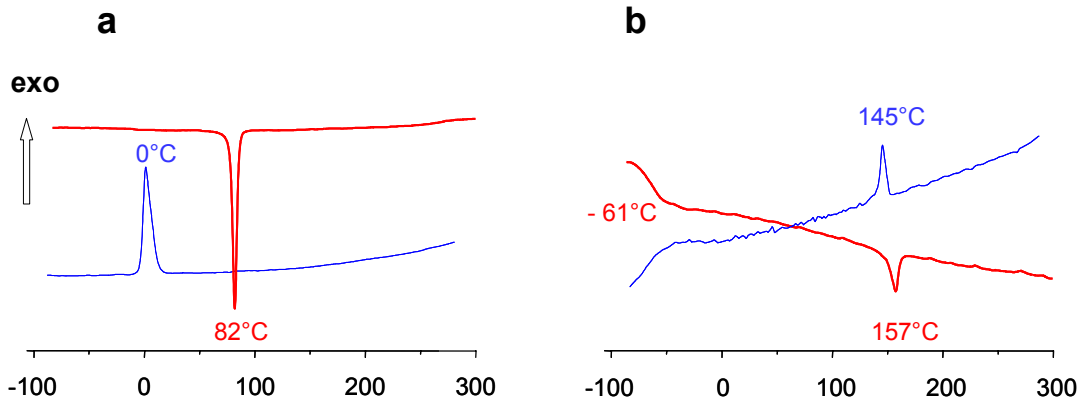

Figure 6.2 DSC traces of **a)** Pch2-$(COOC_8)_8$ and **b)** Pch2-$(COOC_{8,4})_8$ measured from -100°C to 300°C at a heating rate of 10°C/min, blue – first cooling, red – second heating

It has been well documented that branched peripheral substituents promote the formation of mesophases and decrease both the temperature of the transition between crystalline and LC phases and isotropization temperature of discotic molecules compared to analogs with linear substituents.[116,117] This is largely due to the increased steric hindrance that reduces the π-π stacking of the flat aromatic cores. Indeed, Pch2-$(COOC_{8,4})_8$ bearing the more sterically demanding 2-butyloctyl peripheral chains is liquid crystalline at ambient conditions and its isotropization temperature is dramatically reduced compared to the linear C_8 chain isomer (transition onset 157°C [8.2 kJ mol^{-1}] on heating, 145°C [8.3 kJ mol^{-1}] on cooling). The Pch2-$(COOC_{8,4})_8$ alkyl chains freeze at - 61°C (transition onset -70°C).

6.3. Solid state NMR

6.3.1. ^{1}H NMR spectroscopy

The variable temperature proton NMR spectra of the phthalocyanine octaesters recorded at 25 kHz MAS and -25°C effective sample temperature (for the Pch2-$(COOC_{8,4})_8$)

and -36°C effective sample temperature (for Pch2-$(COOC_8)_8$). After initial cooling the samples have been then heated up in steps of 5 or 10°C with 10 minutes equilibration time between the consecutive heating steps and proton spectra have been recorded in each step.

The $C_{8,4}$ phthalocyanine derivative is in the liquid-crystalline state in the temperature range -61°C to 157°C as determined from the DSC measurements (see Figure 6.2), as well as previous studies.[111] So, sharp spectral lines for the alkyl resonances due to the significant chain mobility are expected. Furthermore, the chemical structure of the octa-substituted phthalocyanine molecule suggests the presence of eight chemically equivalent protons and thus, only one sharp peak is expected in the aromatic region of the ^{1}H NMR spectrum in the mesophase.

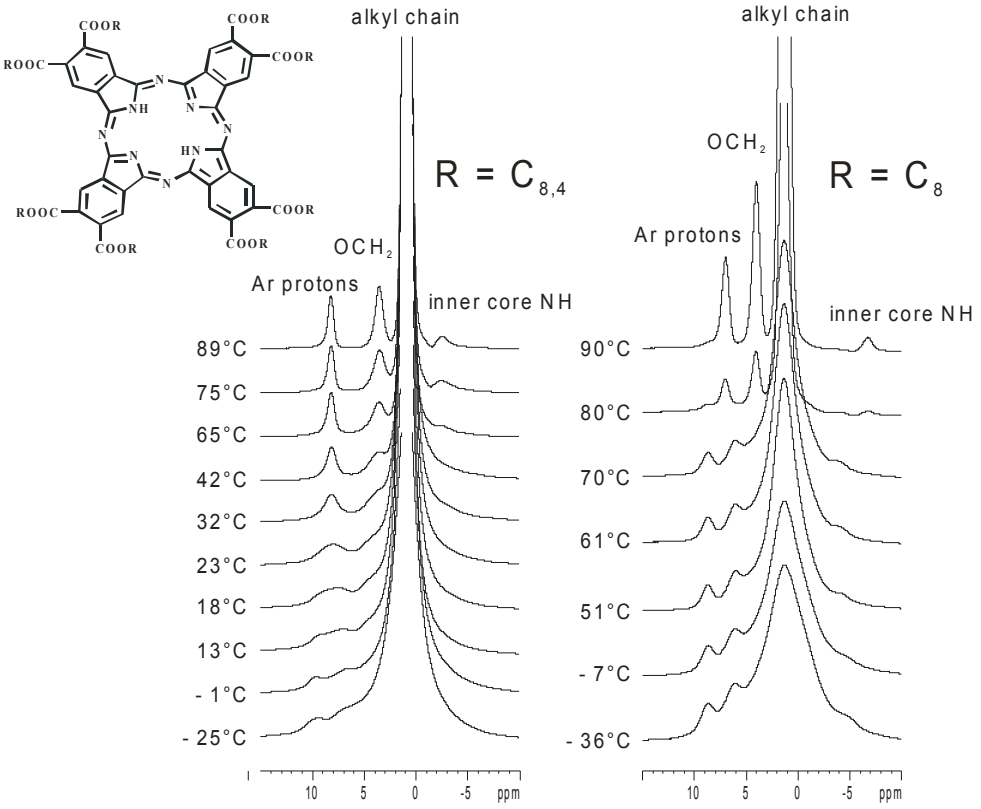

Figure 6.3 Variable temperature (VT) ^{1}H NMR spectra of Pch2-$(COOC_{8,4})_8$ (left) and Pch2-$(COOC_8)_8$ (right) recorded at 25 kHz spinning at the magic angle

In the ^{1}H NMR spectrum recorded at the lowest experimental temperature (-25°C) two spectral lines as well as a shoulder in-between are observed. In the aliphatic region of the ^{1}H MAS NMR spectrum the peak at 1.3 ppm arises due to the resonances of the CH_2 protons. The peak is inhomogeneously broadened covering a range of almost 10 ppm (from -5 ppm to

5 ppm). The sharp top of the peak is due to mobile terminal methylene and methyl groups, where the proton homonuclear dipole-dipole couplings are significantly reduced by segmental motion and/or the fast rotation of the CH_3 protons about the threefold symmetry of the methyl group. Upon heating, the width of the peak is reduced and at *ca.* 30°C a shoulder appears in the 3-4 ppm region. Further temperature increase results in even better resolution expressed in separation of the OCH_2 proton peak at 3.5 ppm from the chain CH_2 resonances.

High temperatures are also beneficial to observe the resonance of the inner core protons at -2.5 ppm, otherwise covered in the foot of the broad CH_2 peak. It should be noted that a chemical shift of -2.5 ppm suggests absence of packing effects at temperatures as high as 65°C. Possible explanation is increased interdisc distance in the columns due to the growing steric demands of the branched mobile chains.

In the aromatic region of the ^{1}H NMR spectrum of Pch2-$(COOC_{8,4})_8$ recorded at -25°C effective sample temperature and 25 kHz MAS frequency a broad, still well resolved, peak at 9.5 ppm as well as a shoulder at *ca.* 7 ppm are detected. Remarkably, it is *two aromatic resonances* observed in the *mesophase* (as discussed above, the mesophase state is detected by DSC and solid state NMR techniques). There are two possible explanations for this phenomenon: the presence of packing effects, related with difference between the symmetry of the phthalocyanine molecule experiencing these effects and the symmetry of the column, in the mesophase (the neighbouring discs are displaced in the columnar stack) or a coexistence of two different thermodynamic phases with different packing (solid and liquid-crystalline). In general, the influence of packing effects on the proton chemical shifts in columnar structures is a well-known phenomenon[79,82] in the crystalline state. However, to the best of our knowledge there have been no related reports about the phenomenon occurring in the liquid-crystalline state. Additionally, the peak and the shoulder in the aromatic region are broadened suggesting an inhomogeneous distribution of the aromatic proton chemical shifts. This point will be discussed in more details below regarding the molecular dynamics studies. Increasing the temperature the peak at 9.5 ppm becomes slightly sharper and shifts to higher field. At the same time, the shoulder detected in the aromatic spectral region separates as a peak, which at 23°C merges with the lower field signal for the aromatic protons. Further temperature increase to 89°C results in spectral line narrowing.

The interpretation of the line broadening in terms of chemical exchange between two aromatic protons with different chemical shifts provides a rough estimation of the segmental (disc) dynamics. At lower temperatures (- 25°C : 0) the phthalocyanine molecules are in the

slow exchange regime. The proton spins in this regime precess at a frequency ν_1 and briefly exchange into another environment with a different frequency ν_2. Returning to their original shift, they will be out of phase in respect to those spins, which do not exchange. The accumulation of these phase errors leads to destructive interference in the FID and signal loss. As a result, the FID decays rapidly, and the Fourier transformation produces broad lines. The decay rate of the FID, assigned as R, is a measure of the lifetime of the spins in a definite state τ. Thus,

$$\tau = 1/R = 1/\pi\Delta\nu\,, \tag{6.1}$$

where $\Delta\nu$ is the difference between the frequencies of the two states in Hz. Considering the difference in Hz in the precession frequencies of the aromatic proton spins as a function of temperature (see Figure 6.3), lifetimes varying from 0.18 ms to 0.30 ms for the temperature range of – 1°C : 13°C were calculated using equation 6.1. Therefore, assuming no additional broadening due to a spread of precession frequencies, the discs slowly tumble at temperatures as low as 13°C.

Increasing the temperature the proton spins under discussion exchange faster, respectively their lifetimes in the two states become shorter. The transition from slow to fast exchange takes place when

$$k_{ex} = \pi\Delta\nu\sqrt{2} = 2.22\Delta\nu\,, \tag{6.2}$$

and k_{ex} is the exchange rate. The temperature at which the transition from slow to fast exchange takes place is called *coalescence temperature*. The broadening in the fast exchange regime (if still present) is also a function of the difference in the precession frequencies, however, proportional to ($\Delta\nu^2$).

The VT ^{1}H NMR spectra of Pch2-$(COOR_8)_8$ are presented on Figure 6.3 (right). In the low temperature (- 36°C) ^{1}H NMR spectrum, recorded at 25 kHz MAS, the broad alkyl CH_2 peak is observed at 1.5 ppm. The shoulder at - 4 ppm is attributed to the resonances of the inner core protons. Similarly as the branched chain derivative, the symmetry of the molecule of the linear C_8 one suggests eight equivalent aromatic protons and respectively a single resonance in the aromatic spectral region. Again, two well-resolved peaks in the aromatic spectral region are detected at 6.2 ppm and 8.7 ppm.

As already discussed for the ^{1}H spectra of the $C_{8,4}$ phthalocyanine derivative, heating results in improved resolution. Considering the inner core protons a shift of almost one ppm to higher frequencies (lower fields) is observed when increasing the temperature from – 36°C to 70°C. This phenomenon is attributed mostly to temperature dependent out-of-plane disc vibrations/fluctuations, which slightly change the shielding of the inner protons due to the neighboring aromatic systems. The shape of the aromatic peaks remains unaltered upon heating to 70°C. As the compound enters the mesophase at 82°C, the ^{1}H NMR spectrum changes dramatically.

The significant chain mobility results in a sharp alkyl peak in the proton spectrum recorded at 90°C with a full width at half maximum of 615 Hz, which compared to the same parameter in the crystalline state at -36°C (3500 Hz) is approximately a fivefold reduction. Additionally, the resonance of the OCH_2 group separates as a well-resolved sharp peak at 4.0 ppm. The most dramatic changes are observed in the inner core protons region. The proton signal shifts to higher field with almost 4 ppm from *ca.* -4.0 ppm to - 8.0 ppm. This phenomenon is attributed to a change in the disc packing. The packing in the crystalline state evolves in a rapid core rotation about the columnar (director) axis in the liquid-crystalline state. Thus, the displacement of the discs, leading to different electronic environment for the aromatic protons in the crystalline state, is no longer present, i.e. the rotation of the phthalocyanine molecules is such to preserve the columnar stack and without significant lateral excursions (on average) from the columnar (director) axis. This implies better shielding of the inner protons from the neighboring aromatic systems, which indeed is observed in the ^{1}H solid state NMR spectra. The result is a high field shift for the inner protons.

The change in the columnar packing as the compound enters the mesophase is also observed in the aromatic spectral region. Above 80°C the two proton resonances at 6.2 and 8.7 ppm merge into one with a chemical shift of *ca.* 7 ppm. As seen from the ^{1}H NMR spectrum recorded at 80°C (in the aromatic as well as the inner core protons regions), there are resonances characteristic for both the crystalline and liquid-crystalline states. This leads to the conclusion that the phthalocyanine C_8 derivative enters the mesophase through a transition state, which is characterized by both types of packing, i.e. both rotating discs and static disc packing are present in the columns. As the equilibration time between the consecutive heating steps was 10 minutes, differences in the packing arising from a heat transfer gradient in the sample are not very likely. However, it is not excluded that a pressure

gradient in the sample, arising from the centrifugal forces at high spinning speeds from the rotor center to the walls might contribute to the observed phenomenon[1].

The high temperature ^{1}H NMR spectra of the two phthalocyanine derivatives look quite similar, the only difference observed being the different chemical shift of the inner core protons. The observed 6 ppm high field shift in the case of the $C_{8,4}$ derivative, as already discussed, is well explained with the steric hindrance of the branched peripheral chains that reduces the π-π stacking of the flat aromatic cores resulting in larger interdisc distances and worse intracolumnar order in the mesophase.

6.3.2 ^{1}H-^{1}H DQF NMR spectroscopy

^{1}H double quantum spectroscopy under fast spinning conditions was further used to investigate the packing and dynamic behavior of the phthalocyanine octaesters.

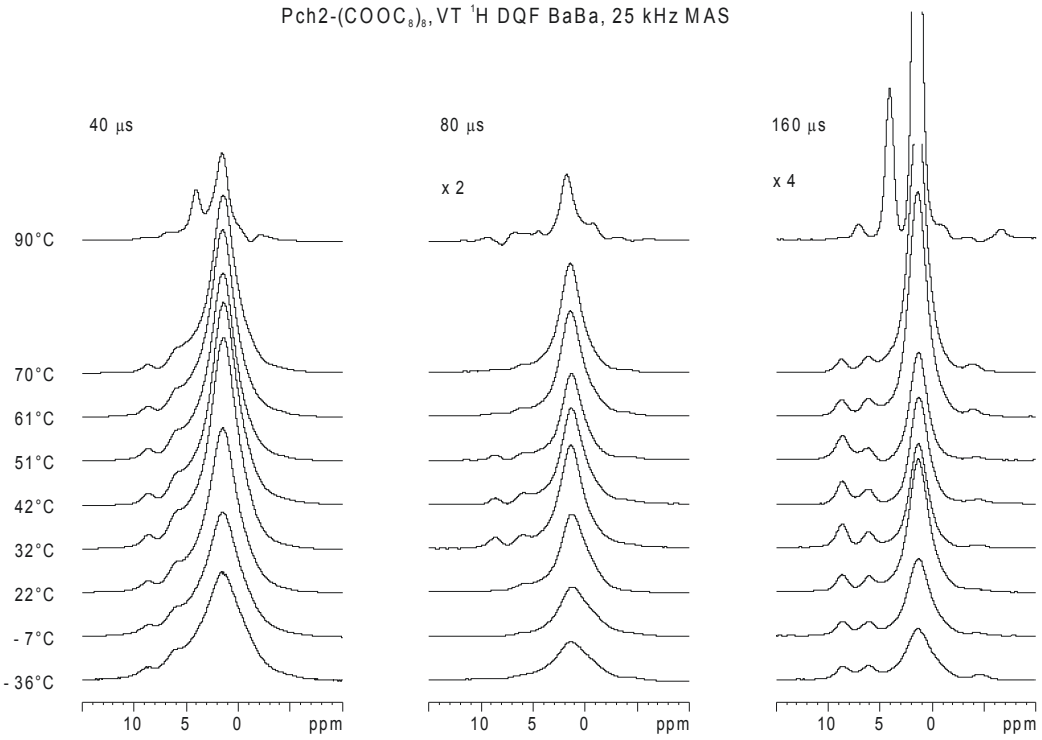

Figure 6.4 VT ^{1}H DQF BaBa spectra of Pch2-$(COOC_8)_8$, recorded at 25 kHz MAS and different excitation times

[1] Due to the fast spinning, the pressure close to the rotor walls is higher compared to the rotor centre. Therefore, taking into account the reverse dependence of the temperature on pressure, part of the sample close to the rotor walls might have entered the mesophase, while the part close to the centre should not have acquired the energy needed to do so.

The variable temperature proton double-quantum filtered BaBa spectra of the linear C_8 phthalocyanine derivative recorded at 25 kHz MAS and different excitation times are presented in Figure 6.4. As already discussed in the methodological part, coherences between strongly coupled spins give rise to signals in the double-quantum filtered spectra recorded using short excitation times. Thus, in the DQF BaBa spectra recorded at 40 μs excitation time (Figure 6.4 left) all detected signals are due to coherences between strongly coupled proton spin pairs.

As seen from the spectra in the crystalline state up to temperatures of 70°C there are not significant changes taking place. Only a narrowing of the alkyl CH_2 protons peak at 1.3 ppm is observed, related to increase in the amorphous chains mobility. Clearly, two types of aromatic protons are present in the system with resonance signals at 6.5 and 9.0 ppm, which merge into one on the onset of the rapid disc rotation when the compound enters the mesophase. In addition, all peaks lose intensity at temperatures above 80°C.

More intriguing are the temperature dependent ^{1}H-^{1}H DQF BaBa MAS spectra recorded at 80 μs excitation time (Figure 6.4 right). Compared to the spectra recorded with shorter (40 μs) excitation time, the peak intensity in general decreases by nearly a factor of two. However, within the 80 μs series peaks gain intensity and become sharper upon heating, which leads to improved resolution (see above).

Surprisingly, in the temperature range of 30-50°C peaks due to double-quantum coherences involving the aromatic protons appear. Thus, an indirect estimation of the mobility, as well as the packing of the phthlocyanine molecules as a function of temperature can be performed.

Obviously, at lower temperatures strong homonuclear ^{1}H-^{1}H dipole-dipole couplings are characteristic for the system (DQ coherences between the strongly coupled ^{1}H spins are not observed in the DQF BaBa spectra, recorded at 80 μs excitation time). Upon heating the couplings are reduced due to increased molecular mobility, which leads to the appearance of the resonances in the aromatic protons region. Further heating results in loss of these coherences as the mobility further increases and more recoupling time is needed to observe DQ coherences between these proton spins.

The ^{1}H DQF BaBa MAS spectra recorded with 160 μs excitation time are presented on Figure 6.4 (right). In the low temperature spectra of the series the signals observed are due to DQ coherences between weakly coupled spin pairs. Obviously, high temperatures promote higher mobility and respectively better resolution, as well as signal intensity increase.

Additionally, at four rotor periods excitation time (160 μs) the peak due to double-quantum coherences between the inner core protons is detected at *ca.* - 4.5 ppm at all experimental temperatures with a slight shift towards higher frequencies upon heating. Also, the relative ratio (9.0 ppm : 6.5 ppm) of the aromatic protons signals changes as a function of temperature from ca. 1:1 at low temperatures to *ca.* 2:1 at temperatures around 30°C. A possible explanation for the observed change in the signal intensity is changes in the packing (see Figure 6.5), related to polymorphism, upon introducing thermal energy in the system.

In all spectra recorded in the mesophase (90°C and above) characteristic dispersive line-shapes are observed which are due to hardware reasons related with the vibration frequency of the detection coil at high bearing pressures.

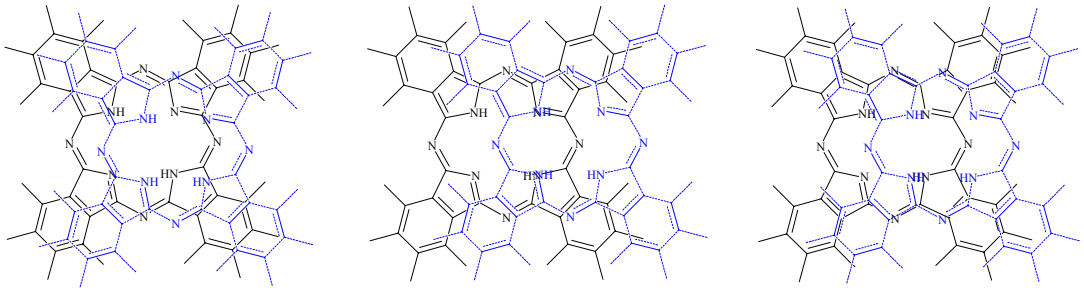

Figure 6.5 The polymorphic structures of the metal-free phthalocyanines, related to the "herringbone" packing arrangement.[122] The side chains are omitted for clarity.

6.3.3 ^{1}H-^{1}H 2D double-quantum NMR spectroscopy

Further investigation of the packing of the columnar phthalocyanines required recording two-dimensional rotor-synchronized proton DQ correlation NMR experiments as described in the Chapter 3. Figure 6.6 shows the ^{1}H-^{1}H 2D DQ BaBa spectrum of Pch2-$(COOC_8)_8$ recorded at 25 kHz MAS, 160 μs time used to excite and reconvert the proton double-quantum coherences and -36°C effective sample temperature.

In the upper right corner of the spectrum a diagonal peak at (- 4.5 ppm, - 9.0 ppm) arising due to a double-quantum coherence between the inner core protons (the interproton distance is 2.04 Å) is observed. The observed homogeneous broadening (more than 2 ppm) of

the resonance signal is attributed to lateral displacement of the neighboring phthalocyanine discs, which results in slightly different proton shielding.

The most intense peak in the spectrum is the one due to coherence between the protons of the alkyl CH_2 groups at (1.3 ppm, 2.6 ppm). However, it hardly provides useful information about the packing of the compound in the crystalline state. Such information can be obtained from the different chemical shifts of the aromatic protons.

The two peaks situated on the diagonal at (6.0 ppm, 12.0 ppm) and at (9.0 ppm, 18.0 ppm) respectively arise due to double-quantum coherences excited between aromatic protons having identical chemical shifts. Additionally, cross-peaks due to coherences between the aromatic and aliphatic (alkyl chain) protons at *ca.* (9.0 ppm, 10.3 ppm) and (1.3 ppm, 10.3 ppm) are detected. It should be noted that the latter peak is barely visible (or in some cases completely absent) in the two-dimensional DQ spectra, which phenomenon has been observed before in systems with mobile alkyl chains[118,119].

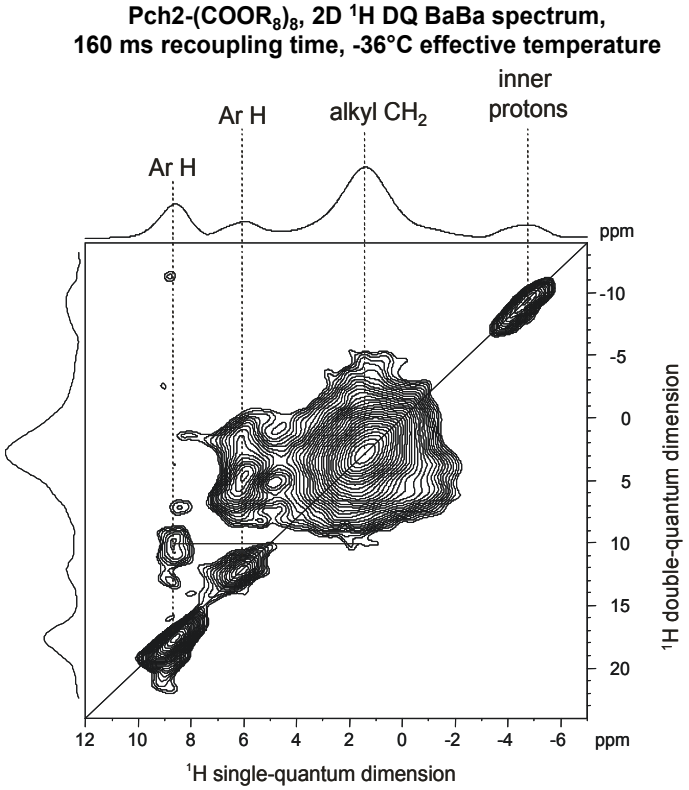

Figure 6.6 ^{1}H two-dimensional double-quantum BaBa spectrum of PcH2-$(COOC_8)_8$ recorded at 25 kHz MAS, 160 μs excitation time and -36°C effective sample temperature. Note the effects of the packing on the aromatic protons chemical shift

Upon heating the Pch2-$(COOC_8)_8$ compound enters the mesophase, which leads to a rotation of the discotic phthalocyanine molecules. On the onset of this process the two aromatic resonances merge into one, i.e. a change in the packing occurs.

The Pch2-$(COOC_{8,4})_8$ derivative is in the liquid-crystalline phase in the instrumentally accessible temperature range. In the mesophase the compounds packing and complex dynamics are significantly influenced by the high steric requirements of the branched alkyl chains – the phthalocyanine discs modified with branched chains are packed significantly worse than those with linear chains (see Figure 6.7 c). In addition, the fast disc rotation in the mesophase results in averaging of the chemical shifts of the aromatic protons at higher temperatures. In the 2D DQ BaBa spectra of the Pch2-$(COOC_{8,4})_8$ (not presented) the strong signal of the mobile CH_2 moieties covers most of the spectral range preventing the acquisition of information about coherences between the inner core protons.

6.4 2D WAXS on oriented samples of Pch2-$(COOC_8)_8$ and Pch2-$(COOC_{8,4})_8$

The relation between the molecular structure and supramolecular organization of the functionalized phthalocyanines has been investigated in addition by two-dimensional wide-angle X-ray scattering (WAXS) experiments of oriented samples in the compounds´ different thermotropic phases. The samples for the 2D WAXS experiments have been prepared by filament extrusion. The temperature dependent 2D WAXS patterns of Pch2-$(COOC_8)_8$ are presented on Figure 6.7.

Planar aromatic molecules usually crystallize in slipped-stacked arrangements, i.e. the overlapping neighboring molecules in a stack are slightly displaced in a direction along the stacking axis when observed perpendicularly.[120,121] A wide variety of stacking geometries exist, as the parameters differentiating between those are stacking distance (centre-to-centre), stacking angle of the macrocycle towards the stacking (columnar) axis and the orientation between the two neighboring phthalocyanines towards each other.[122] The 2D WAXS on oriented samples is used to differentiate between the herringbone and the brickbone packing arrangements of phthalocyanines; in the former, the molecules from neighboring columns make an angle towards each other and in the latter, they are parallel.

In the crystalline state the columns formed by the stacked discotic molecules of Pch2-$(COOC_8)_8$ are oriented along the extrusion direction. The distinct equatorial reflections

suggested a well ordered supramolecular structure. Additionally, the large number of higher order reflections emphasized the high crystallinity of the compound. Furthermore, the distinct off-meridional reflections clearly lead to the conclusion that the discs orientation relative to columnar axis is tilted, i.e. the discs are organized in the so-called herringbone packing. From the 2D WAXS pattern measured in the crystalline state at - 20°C (Figure 6.7 a) a tilting angle of about 40° was obtained. To further distinguish between the different known polymorphs of the metal-free phthalocyanines (to determine the orientation between the two neighboring macromolecules towards each other), i.e. α-, β- or γ-phthalocyanines (Figure 6.5), it is useful to examine the ^{1}H solid state NMR spectra of the compounds under discussion. The reason is that the different polymorphs stack in a different manner leading to different electronic environments for the aromatic protons, which experience to a different degree the ring current effects. A simple deconvolution procedure provides the ratio between the shielded and deshielded aromatic protons in the crystalline state (1 : 1), which ratio is then related to the respective polymorphic structure. Such 1 : 1 ratio of shielded : deshielded protons is characteristic for the β- and γ-polymorphic structures, while the α-phthalocyanines is characterized by only one type of protons (equally shielded).

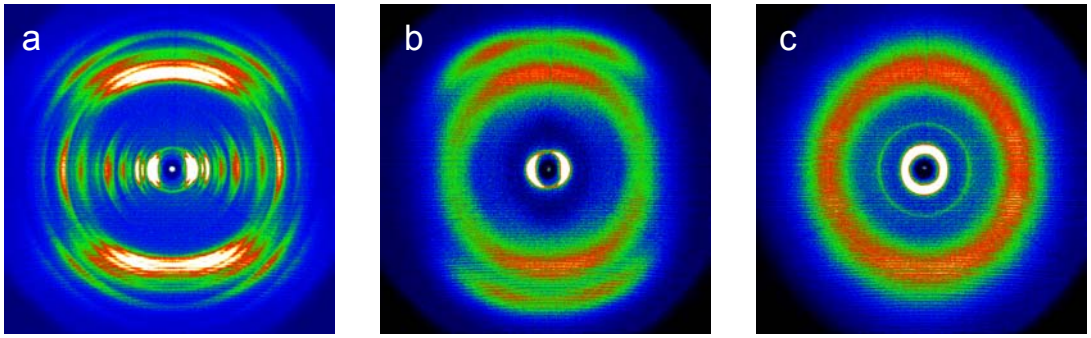

Figure 6.7 2D WAXS patterns of oriented by filament extrusion fibers of Pch2-$(COOC_8)_8$ **(a)** in the crystalline phase at - 20°C and **(b)** in the mesophase at 100°C and **(c)** Pch2-$(COOC_{8,4})_8$ in the mesophase at 100°C

The 2D WAXS spectrum undergoes a significant change when the Pch2-$(COOC_8)_8$ is heated above the mesophase transition (Figure 6.7 b). The distinct high order equatorial reflections are no longer visible, suggesting low long-range order. In addition, in the mesophase the aromatic cores of the phthalocyanine derivative start a rapid rotation about the columnar axis, which motion is detected by the significant decrease (50% or more) of the ^{1}H-^{13}C dipole-dipole coupling constant of the aromatic CH moiety (see below). Unlike other

discotic molecules, the phthalocyanine C_8 octaester does not lose the tilted orientation, though the tilting angle is reduced almost by half, i.e. being 25° at 100°C. To evaluate the orientation of two neighboring discs relative to one another in the mesophase is impossible due to the fast disc rotations. The latter are typically related with additional out-of-plane fluctuations (to be discussed below), which are the reason for the loss of sharpness of the meridional reflections in the WAXS pattern. Additionally, the enhanced mobility in the whole system in the mesophase results in a loss of the reflections, characteristic for the crystalline alkyl chains. Instead, a broad halo, implying amorphous side chains, is observed. The disc fast molecular dynamics in the liquid-crystalline state results also in averaging of the chemical shift differences between the aromatic protons arising from the packing in the crystal lattice.

The WAXS pattern of the branched chain phthalocyanine derivative (Figure 6.7 c) does not change as a function of temperature – it looks quite similar independent on the thermotropic phase of the compound (below the glass transition at a temperature of – 80°C compared to the pattern recorded at ambient conditions in the mesophase). This is due to the significant intracolumnar disorder introduced by the spatial requirements of the bulky $C_{8,4}$ side chains. In addition, the width of the scattered intensity, related with the interdisc distance, suggests a distribution of the latter.

6.5 ^{13}C CP MAS NMR

To characterize further the phthalocyanine derivatives ^{13}C cross-polarization spectra have been recorded at 25 kHz MAS as a function of temperature. As expected upon heating the dipolar couplings were reduced due to increased molecular mobility, which resulted in reduced cross-polarization efficiency, respectively a decrease in the ^{13}C signal intensity and peak narrowing.

As seen from Figure 6.8 the crystalline fraction of the alkyl chains observed at 37°C at 32.4 ppm and related to the energetically stable trans-conformation is almost completely lost increasing the temperature, on account of the gauche-CH_2 groups observed at 30.8 ppm at higher temperatures.

In addition, in the 110 – 130 ppm spectral region of the ^{13}C spectrum recorded in the crystalline state of the linear C_8 chain derivative two resonances are expected to appear – those of the quaternary aromatic carbons, marked in red. However, five peaks

are observed. Two phenomena possibly contribute to the appearance of the five ^{13}C resonances in the cross-polarization spectrum of the Pch2-$(COOC_8)_8$ derivative. Either different shielding of these quaternary carbons due to the neighboring aromatic systems leads to different chemical shifts, or the inner protons are in a slow exchange regime at these temperatures leading indirectly to different electronic environments for the carbons under discussion. Considering the first scenario, shielding effects of neighboring systems is a well-known phenomenon affecting all nuclei in a similar manner, however reported mainly for protons. Chemical exchange of the central protons has also been thoroughly investigated both in the solid state and in solution.[108,109] Here, it is not clear which of these phenomena and to what extent contribute to the observed signal splitting.

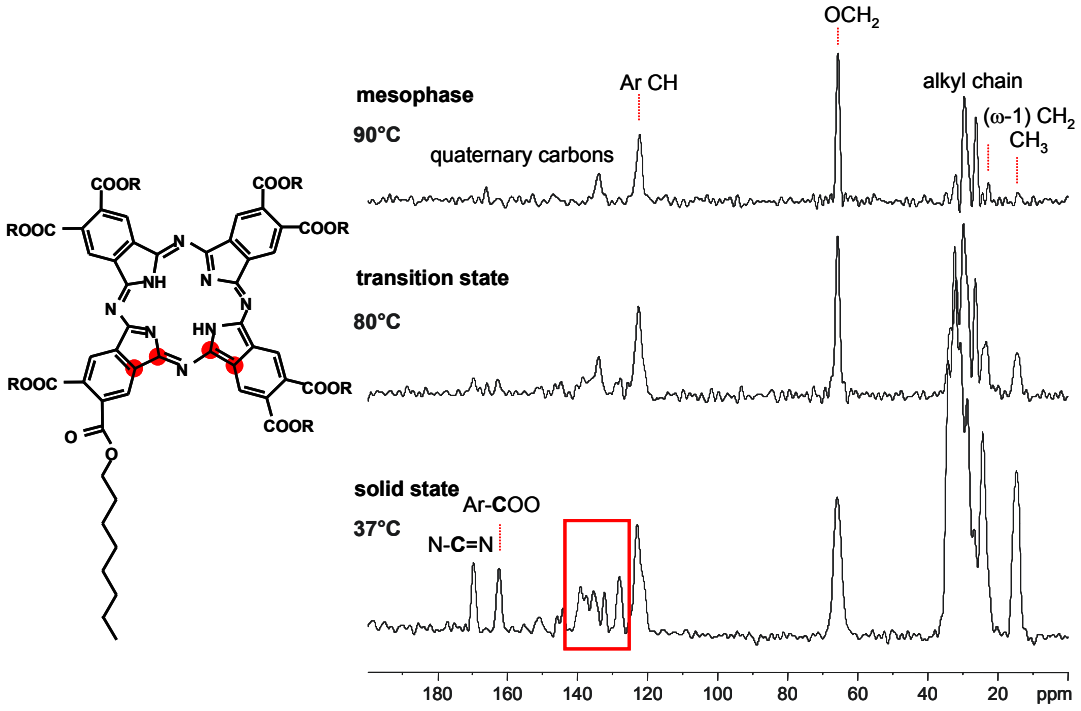

Figure 6.8 VT ^{13}C CP NMR spectra (right) of Pch2-$(COOC_8)_8$ (chemical structure presented left) with a region marked red, where five ^{13}C resonances appear due to packing, while only two such are expected. The spectra were recorded at initial sample cooling below 0°C.

Increasing the temperature the compound enters the mesophase (the ^{13}C CP MAS spectrum in the liquid-crystalline state is presented on Figure 6.8 top) through a transition state (Figure 6.8 middle). The transition state is characterized by significant chain mobility, which leads to reduction of the dipole-dipole coupling constants, respectively to lower cross-polarization efficiency. Thus, the ^{13}C resonances of the quaternary Ar**C**OO- and N=**C**-N

carbons, which do not have a proton directly bonded (nor closely situated) to the respective carbon nuclei, almost completely lose intensity. Similar is the picture for the alkyl chains - all ^{13}C signals decrease in intensity, excluding the OCH_2 peak, which however, becomes sharper. The latter points out that the groups close to the anchoring site remain more rigid than the moieties at the chain ends. Thus, a gradient of mobilities is expected from the aromatic core towards the chain ends.

6.6 Semi-quantitative evaluation of the compounds dynamics - ^{13}C-^{1}H TEDOR

The ^{13}C-^{1}H TEDOR NMR spectra recorded under fast MAS characterize the Pch2-$(COOC_8)_8$ derivative as a function of temperature and recoupling time (Figure 6.9 **a)** 40 μs recoupling time and **b)** 80 μs respectively).

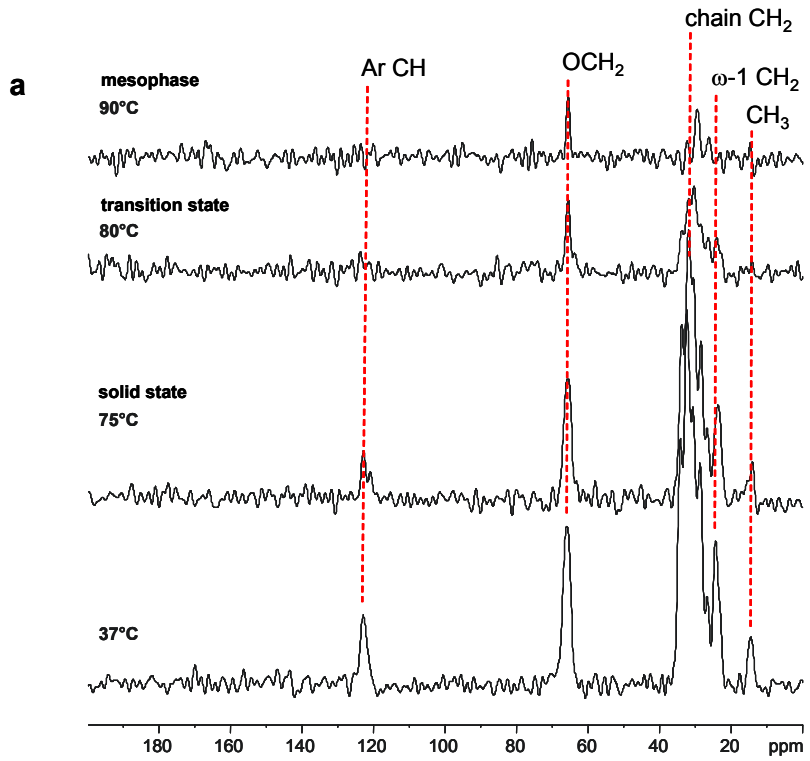

Figure 6.9 **a)** VT ^{13}C-^{1}H TEDOR NMR spectra of Pch2-$(COOC_8)_8$, recorded at 25 kHz MAS and at 40 μs recoupling time. The transition state is clearly observed at 80°C by the behavior the rigid OCH_2 group, as well as the alkyl chains in general, in the spectra – entering the mesophase the chains become mobile and the corresponding ^{13}C resonances suffer a significant intensity loss (40 μs). The spectra were recorded as the sample was initially cooled below 0°C.

The presence of the signal of the OCH_2 moiety in the solid state at 40 μs and its absence at 80 μs recoupling time indicate that the aromatic core and its neighboring groups are rigid. Under heating, the compound enters the mesophase and starts a rotation about the columnar axis. This leads to a reduction of the dipolar coupling constants and consequently reduction of the OCH_2 ^{13}C signal intensity in the 40 μs spectra and, respectively, its appearance in the spectra where more recoupling time is used.

The TEDOR NMR spectra recorded for the Pch2-$(COOC_8)_8$ derivative show that changes in the sample temperature lead to changes in both the compound's mobility and chain conformation. Thus, it is possible to probe/evaluate (by deconvolution) the fractions of a definite chain conformation as a function of both mobility (recoupling time) and temperature and relate those with the intercolumnar distances in both thermothropic phases (the trans-conformation is more elongated than gauche, which respectively results in higher intercolumnar distances). However, the gauche conformation is most often present in discotic compounds modified with alkyl chains for reasons of space filling.

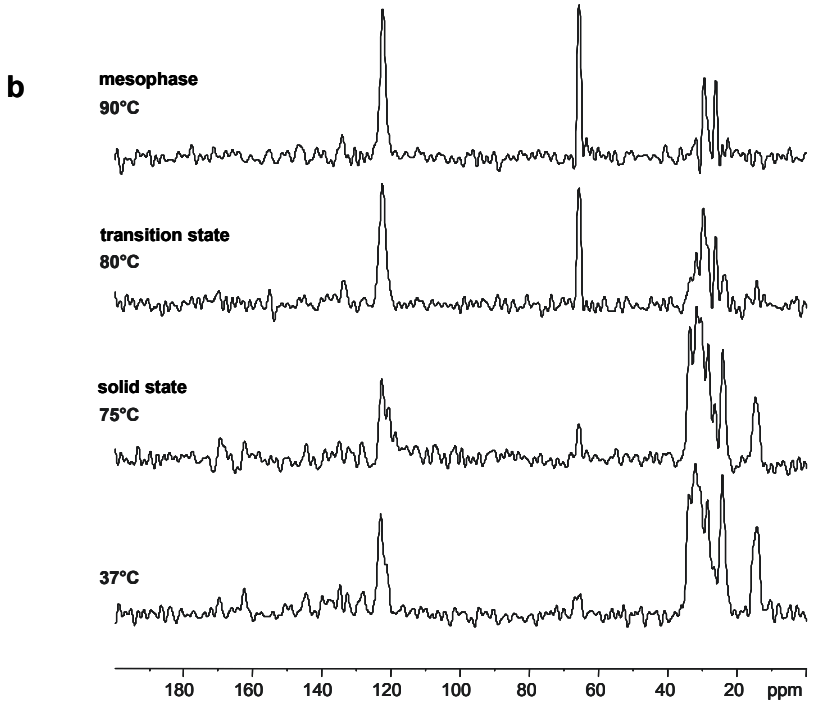

Figure 6.9 **b)** VT ^{13}C-^{1}H TEDOR NMR spectra of Pch2-$(COOC_8)_8$, recorded at 25 kHz MAS and 80 μs recoupling time.

6.7 Quantitative Evaluation of the Molecular Dynamics

6.7.1 ^{13}C-^{1}H REREDOR and REPT-HDOR NMR analysis

As discussed in the theory part both REREDOR and REPT-HDOR are recoupling methods used to record spinning sideband patterns, which after analysis provide the effective heteronuclear (^{13}C-^{1}H) dipole-dipole coupling constants. The motional reduction of the latter is used to evaluate the segmental mobility of a given compound by use of the local dynamic order parameters, S.

The experimentally determined heteronuclear dipolar coupling constants [kHz] measured for the CH_n moiety of the Pch2-$(COOC_8)_8$ phthalocyanine derivative with the related local dynamic order parameters are presented in Table 6.1.

T [°C]	NMR Method	Dipolar coupling constants D [kHz], measured for the CHn moiety; local dynamic order parameter S					
		Ar CH	OCH_2	γ-CH_2	chain CH_2	(ω-1) CH_2	CH_3
		123 ppm	67 ppm	27 ppm	30-32 ppm	24 ppm	14 ppm
37	1	21.5 ~ 1	14.0 0.65	13.0 0.60	11.0 0.51	9.5 0.44	3.0 0.43
	2.1	21.5 ~ 1	15.4 0.72	10.5 0.50	10.5 0.50	9.0 0.42	-
85	2.2	9.0 0.42	3.7 0.17	2.3 0.11	2.0 0.09	-	-
152	2.2	9.0 0.42	-	2.3 0.11	2.3 0.11	-	-

Table 6.1 Dipolar coupling constants D [kHz], measured for the CH_n moiety of Pch2-$(COOC_8)_8$; local dynamic order parameters S; **1** ^{13}C-^{1}H REREDOR, , $t_{rcpl} = 2\ \tau_R$, MAS = 25 kHz; **2.1** ^{13}C-^{1}H REPT-HDOR, $t_{rcpl} = 2\ \tau_R$, MAS = 25 kHz; **2.2** ^{13}C-^{1}H REPT-HDOR, $t_{rcpl} = 8\ \tau_R$, MAS = 25 kHz

In the crystalline state the aromatic core is practically frozen as determined by the dynamic measurements for the CH aromatic moiety ($D_{CH} \approx 21.5$ kHz; S =1), see Table 6.1 and Figure 6.10. At the branching site, the value of the static ^{13}C-^{1}H dipole-dipole coupling for the OCH_2 group is reduced by almost 30% due to rotations and angular fluctuations around the O-CH_2 bond. Along the alkyl chains, the dipole-dipole couplings are reduced gradually towards the mobile chain ends (S = 0.43). Both recoupling methods (REPT-HDOR and REREDOR) provide similar values for the measured dipolar couplings. The slight

differences in the values measured for the chain CH_2 dipolar couplings are probably due to the specificity of the sidebands fitting procedure (the methods error is in the range of 10%).

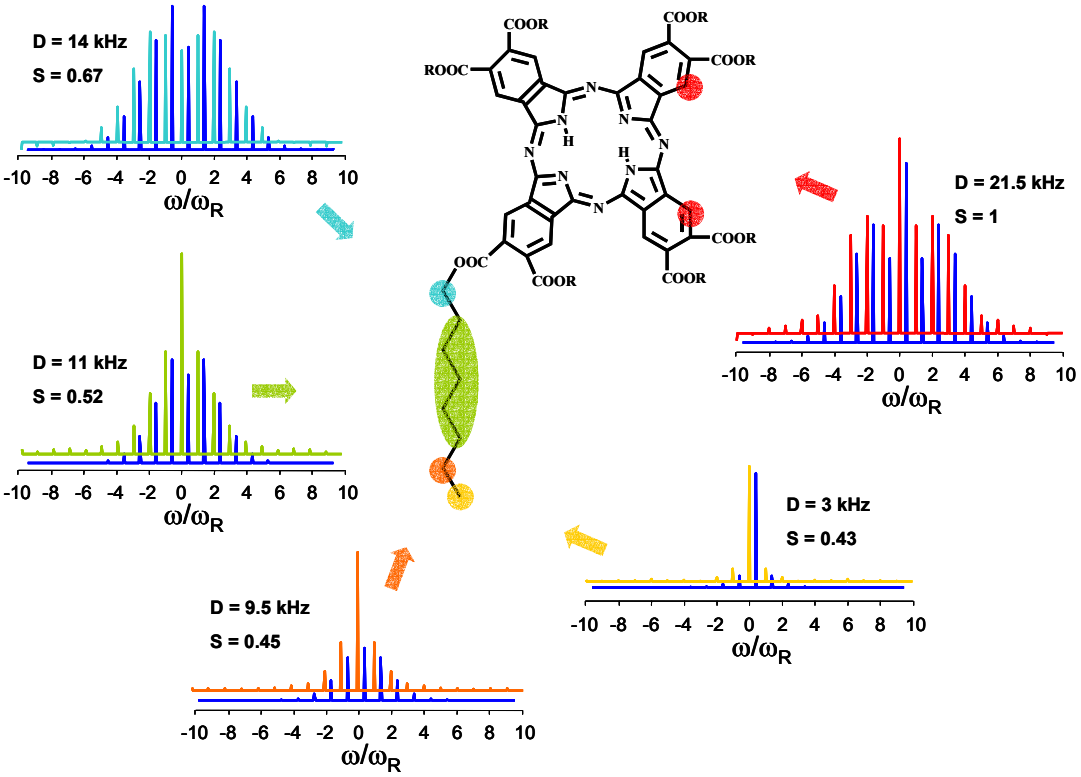

Figure 6.10 REREDOR sideband patterns recorded at 12.5 kHz MAS, 80 μs recoupling time and 37°C effective sample temperature with the simulated patterns (blue) superimposed. The effective ^{1}H-^{13}C dipole-dipole coupling constants, together with the related local dynamic order parameters, are summarized in Table 8.1. The results reveal a frozen aromatic core and a mobility gradient along the alkyl chains.

In the mesophase the dipole-dipole couplings are reduced by 50% due to the fast disc rotation about the columnar axis. Thus, a perfect in-plane rotation would lead to *ca.* 10.5 kHz ^{13}C-^{1}H coupling constant. The observed additional reduction of 1.5 kHz is due to out-of-plane disc excursions/fluctuations (see Table 6.1 and Figure 6.11). Assuming a Gaussian distribution of the angles the phthalocyanine molecules occupy in the course of their motion, it possible to evaluate the width of the distribution σ being ca. 12°. It should be noted that the relation between the width of a Gaussian distribution σ and the full width at half height of the same distribution is 2.35σ. In other chapters of this thesis (chapter 5) the full width at half height of a Gaussian distribution was used instead of σ to characterize the widths of angular distributions.

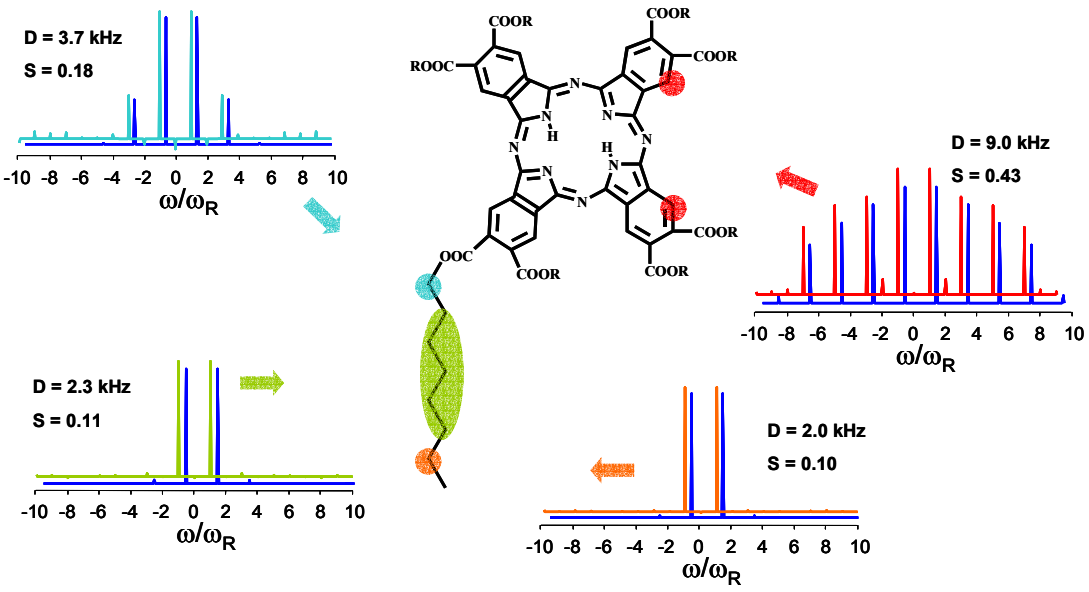

Figure 6.11 REPT-HDOR sideband patterns recorded at 12.5 kHz MAS, 640 μs recoupling time and 85°C effective sample temperature with the simulated patterns (blue) superimposed. The effective ^{1}H-^{13}C dipole-dipole coupling constants, together with the related local dynamic order parameters, are summarized in Table 6.1. The results reveal a core rotation in the mesophase with additional out-of-plane excursions with a width σ = 12°, assuming a Gaussian distribution of the excursion angles, and a mobility gradient along the alkyl chains.

In the mesophase the heteronuclear ^{13}C-^{1}H dipole-dipole couplings of the methylene groups are motionally averaged to the extent that only 10-15% is left out of the couplings of a rigid pair. Remarkably, at relatively low temperatures in the liquid-crystalline phase a gradient of mobility is observed along the chains, while at higher temperatures the couplings are motionally reduced to a similar degree.

The ^{1}H-^{13}C dipole-dipole coupling constants of the CH_n groups of the branched chain phthalocyanine derivative (Pch2-$(COOC_{8,4})_8$) are presented in Table 6.2, together with the related local dynamic order parameters, S, at two temperatures in the mesophase.

Here it should be mentioned that the complex dynamics behavior of the compound leads to difficulties in performing the recoupling NMR experiments. These include reduced signal intensity (due to the reduced value of the dipolar coupling constants) or in some cases even complete lack of ^{13}C signal (see chapter 7) as well as lack of rotor modulation.

T [°C]	NMR Method	Dipolar coupling constants D [kHz], measured for the CHn moiety; local dynamic order parameter S					
		Ar CH	OCH_2	CH	chain CH_2	(ω-1) CH_2	CH_3
		123 ppm	75 ppm	38 ppm	32-30 ppm	23 ppm	14 ppm
37	1.1	-	-	4.0 0.19	3.0 0.14	3.0 0.14	-
72	1.2	8.4 0.40	4.5 0.21	3.8 0.18	3.7 0.18	-	-

Table 6.2 Dipolar coupling constants D [kHz], measured for the CH_n moiety of Pch2-$(COOC_{8,4})_8$; local dynamic order parameters S; **1.1** ^{13}C-^{1}H REPT-HDOR, $t_{rcpl} = 2\ \tau_R$, MAS = 12.5 kHz; **1.2** ^{13}C-^{1}H REPT-HDOR, $t_{rcpl} = 4\ \tau_R$, MAS = 25 kHz

Comparing the experiments conducted at the same recoupling time (160 μs) at two different temperatures in the LC phase, leads to the conclusion that in this particular case, higher temperatures promote more favorable (in terms of NMR signal modulation/acquisition) dynamics. The ^{1}H-^{13}C dipole-dipole coupling constant of the aromatic core CH moiety in the mesophase is reduced by half due to the rapid core rotation. The additional reduction of *ca.* 4 kHz is due to out-of-plane disc excursions. This suggests angular disc fluctuations with a width of a Gaussian distribution σ = 50° and respectively very little intracolumnar order, which is indeed observed in the 2D WAXS patterns.

Considering the alkyl chains dynamics, a twofold increase in mobility is detected at the chain OCH_2 group compared to the aromatic core (S = 0.21 *vs.* S = 0.40 for the core). Such a mobility increase is well explained with the higher degree of freedom of the OCH_2 moiety, as well as the possibility of rotation around the O-C bond. Along the chains the local order parameter of the branching point (S = 0.18) remains virtually the same independent of the temperature, while a slight difference in the ^{1}H-^{13}C dipole-dipole couplings for the chain methylene groups is detected. This is consistent with the general observation that higher mesophase temperatures lead to similar local dynamic order parameters for the whole chain, while at lower temperatures a mobility gradient is characteristic for the alkyl chains.

6.7.2 ^{1}H-^{1}H DQ BaBa Sidebands

To evaluate the compounds dynamics the BaBa experiment has been performed incrementing the indirect spectral dimension in steps smaller than a rotor period, so that sidebands due to the RRE mechanism (see chapter 3) have been recorded. Figure 6.6 shows

^{1}H-^{1}H two-dimensional DQ BaBa sidebands recorded at -36°C effective sample temperature, 25 kHz MAS and 160 μs recoupling time with the t_1 period incremented to observe 7th order sidebands. The experiment was particularly useful to determine the mobility of the inner core protons.

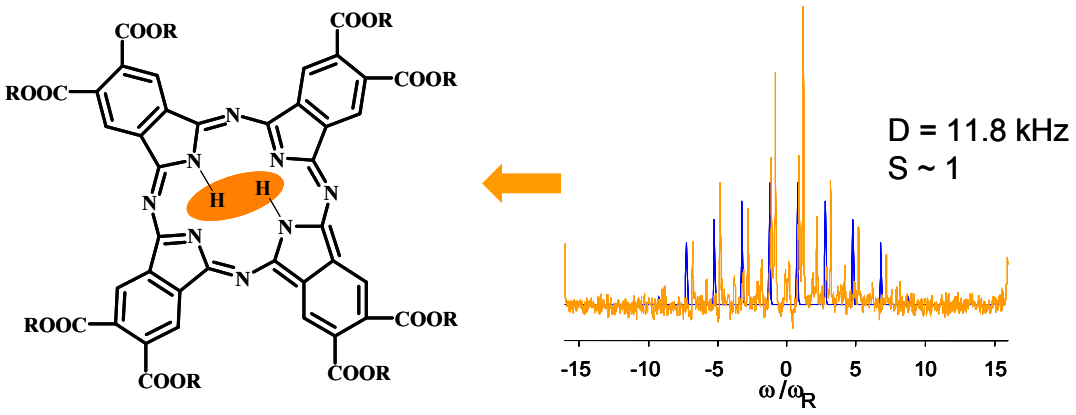

Figure 6.12 ^{1}H-^{1}H DQ BaBa sideband patterns, recorded at 25 kHz spinning at the magic angle, 160 μs recoupling time and effective sample temperature of -36°C for the coupled core protons pair, with the simulated patterns (blue) superimposed; R = C_8H_{17}.

In the crystalline state the aromatic cores are practically frozen, which is determined by evaluating the motional reduction of the heteronuclear dipolar couplings via analysis of recorded ^{13}C-^{1}H REREDOR and REPT-HDOR sideband patterns (to be discussed below). On the other hand, the distance between the inner protons, as determined by quantum mechanical calculations, is 2.04 Å. Therefore, the ^{1}H-^{1}H dipolar coupling between static inner protons pair is calculated to be 14.25 kHz. The effective ^{1}H-^{1}H dipolar coupling between these protons determined at –36°C effective sample temperature by analysis of the BaBa sideband patterns is approximately 11.7 kHz (Figure 6.12). Thus, provided a pure in-plane proton exchange, the related local dynamic order parameter S was determined to be 0.82. As previously established for similar structures, at these temperatures the slow exchange limit is reached.[123]

6.8 Conclusions

1. The modification of the phthalocyanine molecule with branched $C_{8,4}$ alkyl chains results in lowering the mesophase transition temperature as well as significant intracolumnar disorder

compared to the C_8 linear analogue. For this reason the respective $C_{8,4}$ analogue does not crystallize, but freezes at the glass transition. At the same time, the interdisc distance determined from the 2D WAXS patterns remains the same in both investigated phthalocyanine derivatives independent of the type of substituting chains. Thus, easier and less energy consuming processability of the branched analogue without significant impact on the one-dimensional charge carrier properties is expected.

2. The phthalocyanine discs of the C_8 analogues tilt with respect to the columnar axis in the crystalline state, i.e. the so-called “herringbone” packing arrangement, and remain tilted even in the mesophase. However, the tilting angle in the liquid crystalline state is reduced by half, compared to the solid crystalline state, which is related to increased chain dynamics. The latter is obviously insufficient for the planar disc orientation in the LC state, which phenomenon has been observed in all investigated alkyl chain functionalized HBC derivatives so far.

3. The molecular dynamics in the crystalline and liquid-crystalline phase was investigated by analyzing spinning sideband patterns recorded using the heteronuclear recoupling REPT-HDOR NMR technique. Thus, the local dynamic order parameters for the C-H moieties of the phthalocyanine cores and side groups, were acquired. In the crystalline state a frozen aromatic core and a gradient of mobility along the chains of the C_8 phthalocyanine derivative towards the chain ends is observed, as the terminal methylene and methyl groups retain significant mobility. In the mesophase a similar mobility gradient along the C_8 chains is observed at lower temperatures. At higher temperatures in the mesophase all sites of the alkyl chains are characterized by similar local dynamic order parameters for both phthalocyanine derivatives.

4. The dynamics of the proton migration of the inner core protons of the C_8 phthalocyanine derivative was evaluated by analyzing BaBa sideband patterns in the crystalline state. A slow exchange regime is suggested for these protons (inside the frozen phthalocyanine discs) from the measured ^{1}H-^{1}H dipole-dipole coupling as well as the additional ^{13}C signals observed for the quaternary carbons in the ^{13}C CP MAS NMR spectra (at the experimental temperatures lower than 37°C).

Chapter 7. Solid State NMR on a Mixture of Phthalocyanine and Perylene Derivatives

7.1. Introduction

Thin films made of electron donor and electron acceptor molecules and/or macromolecules are of prime importance for the development of large-area, structurally flexible, and low-temperature processable solar cells.[124-126] In this context, most studies have been devoted to the morphology of blends composed of an organo-soluble conjugated polymer and another component. The latter is either another conjugated polymer[127-130] or a low molecular weight active molecule such as a soluble fullerene[131-136] or a perylene derivative.[137] When insoluble components are used, thin films of the blended materials are fabricated by vapour phase deposition.[138]

Blending a liquid crystalline semiconductor with a crystalline or another liquid crystalline active component constitutes a novel approach to this question. The detailed knowledge of the supramolecular organization and the site-specific molecular dynamics of the individual components and the mixture is a prerequisite for the efficient synthetic modelling of the structures to obtain the most suitable properties in terms of processability, thermal stability and charge carrier mobilities. Spectroscopic techniques like solid state NMR and X-ray diffraction are of prime importance for gaining insight in the supramolecular order. The former method, applied under moderate or fast MAS, is an indispensable tool for probing the fast molecular dynamics (on $\tau \sim 10^{-5}$ s timescale).

Taking this into account, a solid state NMR study of the organization in the solid state, as well as the molecular dynamics of a phthalocyanine (Pc), which is a disk-shaped electron donor, and a lath-shaped perylenetetracarboxidiimide derivative (PTCDI), as the electron acceptor (molecular structures depicted in Figure 7.1) and the 3:1 molar mixture of those, has been carried out. The results were correlated with the structural data obtained by the X-ray diffraction experiments on the compounds and the mixture at the same thermal conditions. In addition, optical and atomic force microscopy probing the surface morphology of the individual compounds and mixtures with different ratios of the respective components completed the combined structural, thermotropic, and morphological study. The fact that both

Pc and PTCDI derivatives have been shown to be good candidates for efficient electron transfer[139] determined the interest in this investigation. The pure compounds were synthesized as described elsewhere[140-142] and the blend was prepared by a "neat method" from the melt.[142]

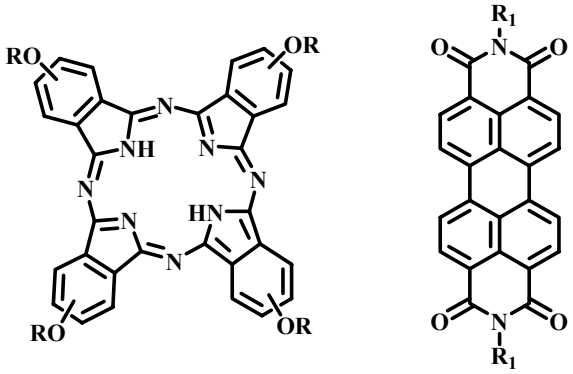

Figure 7.1 Chemical structures of the phthalocyanine (Pc) and perylenetetracarboxydiimide (PTCDI) derivatives. R = $C_{14,10}$, R_1 = $(CH_2)_8$-CH=CH-$(CH_2)_7$-CH_3

Prior to the NMR experiments a differential scanning calorimetric study has been carried out, providing the thermotropic properties of the Pc, PTCDI and the 3:1 molar blend. The phase transitions and the associated transition enthalpies are reported in (Table 7. 1).

It has been established that, upon cooling from the isotropic melt, Pc presents a columnar hexagonal phase from 174°C down to 57°C, and a columnar rectangular phase below 57°C. PTCDI presents a mesophase characterized by a lamelar structure between 282°C and 152°C and a crystalline phase below 152°C. Surprisingly, the mixture Pc: PTCDI = 3:1 (molar ratio) shows a very simple thermotropic behavior. Only one phase transition, though broad, occurring between 265°C and 245°C (peak maximum at 258°C), has been detected by DSC upon cooling from 300°C to 25°C. This phase transition marks the beginning of a temperature range in which the mixture forms a liquid crystalline columnar hexagonal phase.

Variable temperature solid state NMR studies of the supramolecular organization and site-specific molecular dynamics of the Pc, PTCDI and the 3:1 molar blend have been conducted under fast and moderate magic angle spinning conditions in the instrumentally accessible thermotropic phases of the compounds.

Pc:PTCDI[a]	phase behavior[b,c]	Cell parameters[c]
100:0	Col_r 60 Col_h 180 I	Col_r Col_h
	I 174 Col_h 57 Col_r	a = 52.1 a = 31.7
		b = 32.5
75:25	Col_h 260 I	Col_h
	I 258 Col_h	a = 32.0
0:100	Cr 178 L_{Col} 292 I	L_{col}
	I 282 L_{Col} 152 Cr	a = 10.2; b = 3.5; c = 38.1; β = 100.85°

Table 7.1 Thermotropic properties of the pure compounds and the blend. [a] molar ratio; [b] phase transition temperatures (peak, °C) measured during the second heating and cooling runs (10°C/min); [c]. Phase assignment: Cr = crystalline phase; Col_r = columnar rectangular phase; Col_h = columnar hexagonal phase, L_{Col} = Lamello-columnar phase, I = isotropic liquid. [C]a, b and c are in Å.

Taking into account that the main object of the investigation was the mixture, where due to significant peak overlap in the proton spectra the resolution was severely hampered, ^{1}H NMR spectroscopy and ^{1}H homonuclear recoupling techniques, like the DQ BaBa, were applied only to the individual compounds for their characterization. For the mixture the requirement of having well resolved proton chemical shifts, was not fulfilled. Thus, the typically used methods probing the supramolecular order[79,82] via the distance dependent proton-proton dipolar couplings or the effect of the ring currents on the proton chemical shift were not applicable here.

7.2 Pure PTCDI

7.2.1 ^{1}H NMR Spectroscopy

The ^{1}H NMR spectrum recorded at 30 kHz MAS and 45°C effective sample temperature is presented at Figure 7.2 **a)**. In the alkyl part of the spectrum the resonances of the chain CH_2 protons are observed at 1.4 ppm, as well as a shoulder originating from the signal from the NCH_2 moiety at 1.9 ppm. The signals of the CH=CH group are shifted to lower field (5.4 ppm) and the broad line of the aromatic perylene protons is detected at the typical ppm value for aromatic protons of *ca.* 7 ppm. It should be noted however, that the

peak is broadened probably due to the packing of the PTCDI molecules in the crystalline state.

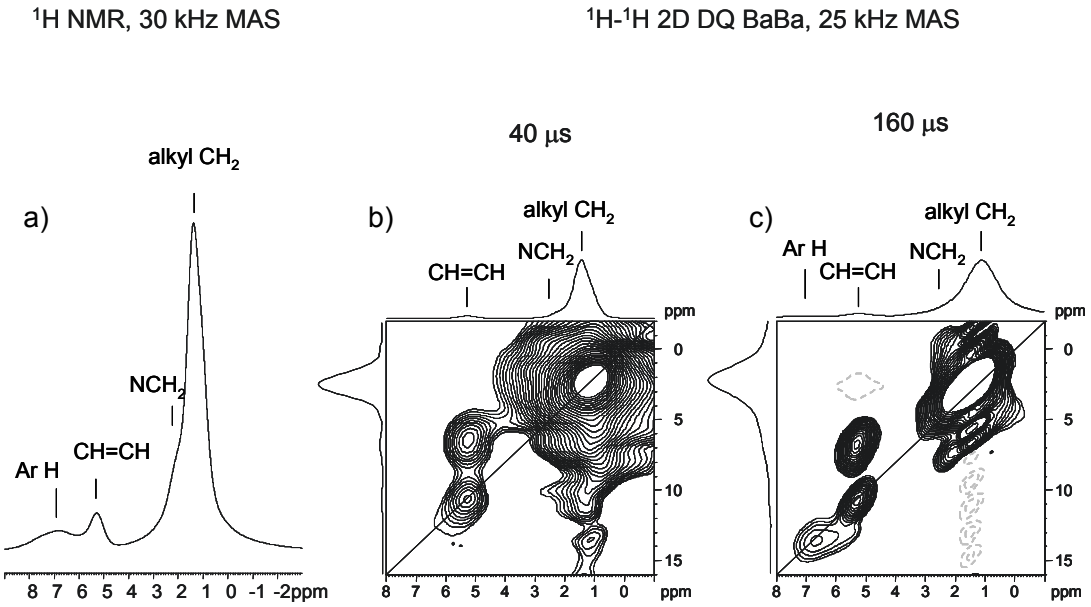

Figure 7.2 **a)** ^{1}H NMR spectrum recorded at 30 kHz MAS; ^{1}H-^{1}H two-dimensional DQ BaBa spectra (**b)** 40 μs excitation time and **c)** 160 μs excitation time) recorded at 25 kHz MAS and 40°C effective sample temperature

Figure 7.2 **b** and **c** show the ^{1}H-^{1}H two-dimensional DQ BaBa spectra of PTCDI recorded at 25 kHz MAS, 40°C effective temperature and excitation times of 40 μs (Figure 7.2 **b**) and 160 μs (Figure 7.2 **c**) respectively.

The spectra provide information about the strength of the proton dipole-dipole couplings and thus about the compounds dynamics. The dominant alkyl peak situated at the diagonal (1.4 ppm, 2.8 ppm) is observed in both 2D DQ spectra (Figure 7.2 **b)** and **c)**), but is not informative about the packing or dynamics of the molecule. More interesting is that the signal (5.4 ppm, 10.8 ppm), due to DQ coherence between the coupled protons of the CH=CH group, is observed at short as well as at long recoupling times. This can be explained with the different conformations (cis- or trans- in respect to the double bond) and respectively different interproton distances at the experimental temperature. Surprisingly, long excitation times (Figure 7.2 c) are needed to observe the signal due to DQ coherence between the aromatic protons (the diagonal peak at 6.8 ppm, 13.6 ppm). This implies mobile perylene core at temperatures as low as 40°C (in the crystalline state). The precise evaluation of the dynamics of the PTCDI molecule applying heteronuclear ^{13}C- ^{1}H recoupling methods is discussed below.

7.2.2 Conformation of PTCDI side chains as studied by VT ^{13}C CP NMR

It is well known that in the solid state the chemical shift apart from the structure of the molecule is also sensitive to differences in the packing and conformation. The sensitivity to the conformation for methylene units is the so-called *γ-gauche* effect. It is defined as the tendency of molecules to adopt the structure, which has maximum number of gauche interactions between adjacent electron pairs or polar bonds.[143] For methylene groups the local field in alkyl chains depends on the conformation of the two γ-positions: gauche-gauche, trans-gauche/gauche-trans, or trans-trans. The result is a low-field shift of approximately 4.5 ppm for a methylene unit in trans-trans chain compared to the one in trans-gauche and approximately 9 ppm compared to the one in gauche-gauche environment. Dynamic averaging of trans- and gauche states as found in fluid phases and far above the glass transition leads to correspondingly averaged values.[144] The conformation of methylene units in alkyl chains has been extensively exploited in the characterization of n-alkanes, cycloalkanes, and polyethylenes[145] and recently in L-glutamate copolymers.[146]

The VT ^{13}C cross-polarization NMR spectra of PTCDI are presented on Figure 7.3. As seen from the Figure, at low temperatures (- 43°C) the spectral lines are most intense as well as broadened. Temperature increase and thus enhanced molecular mobility leads to a reduction of the dipole-dipole couplings and respectively sharper resonances and lower cross-polarization efficiency. The change in temperature also results in a change in the alkyl chains conformation. Lower temperatures promote the low energy trans-chain conformation, which is characterized by a chemical shift value of *ca.* 33 ppm for the methylene units. In the temperature range 0°C - 35°C dominating fraction methylene units with an intermediate (between the shifts characteristic for the trans- and gauche-conformations) chemical shift of 32 ppm is observed. Upon heating, the chemical shift of the CH_2 groups experiences a shift to higher fields (*ca.* 30 ppm), where methylene groups in disordered chains (in gauche conformation) resonate. Further temperature increase (100°C) results in pure (on the time scale of the NMR experiment) gauche CH_2 group conformation, i.e. disordered alkyl chains. As will be discussed below changes in temperature influence not only the conformation, but also the chains dynamics.

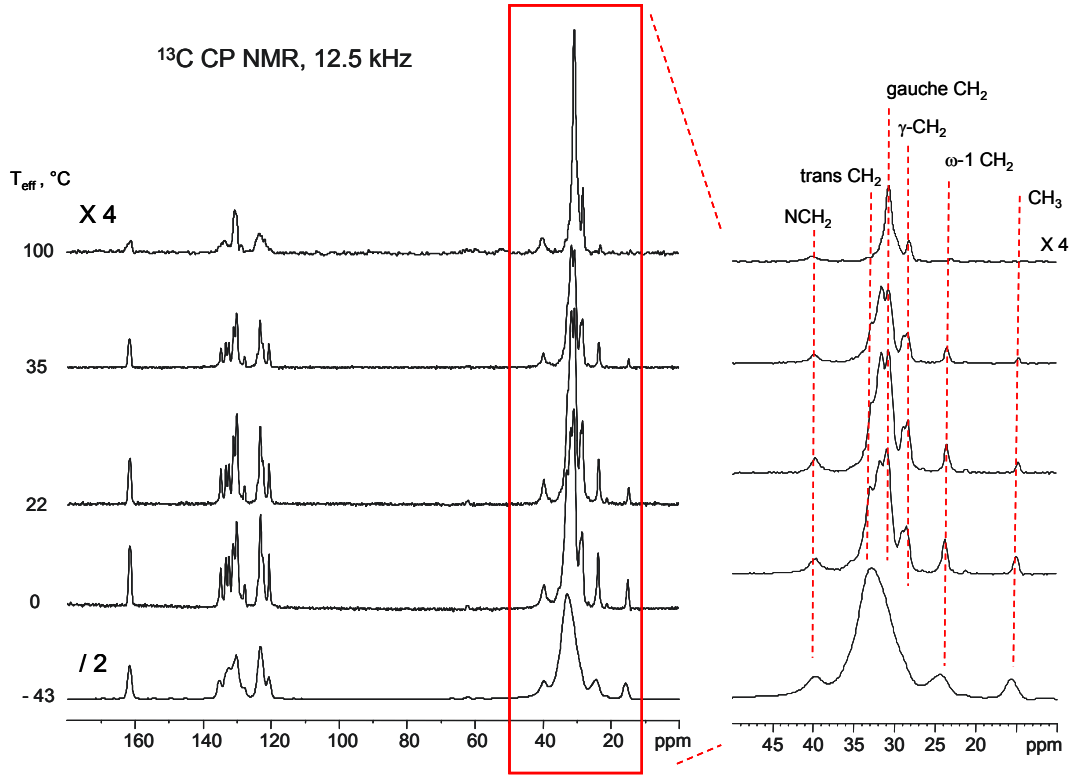

Figure 7.3 VT ^{13}C CP NMR spectra of PTCDI recorded at 25 kHz MAS

7.2.3 Molecular dynamics

In order to probe the molecular dynamics of the pure PTCDI as a function of temperature, the ^{13}C-^{1}H REPT-HDOR heteronuclear recoupling NMR technique has been applied. The ^{13}C-^{1}H REPT-HDOR sideband patterns have been recorded at 12.5 kHz MAS and using 160 or 320 μs recoupling times. To further evaluate the applicability of the method for investigating the systems of interest and for reasons of comparison, another heteronuclear recoupling technique, namely ^{13}C -^{1}H REREDOR, has been used at selected temperatures and the same spinning frequencies and recoupling times, to record spinning sideband patterns. The results are summarized in Table 7.2.

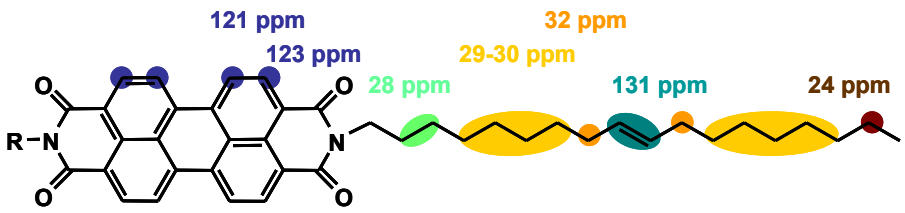

Figure 7.4 PTCDI - Chemical structure with the ^{13}C chemical shifts assignments.

T [°C]	NMR Method	Dipolar coupling constants D [kHz], measured for the CH_n moiety; local dynamic order parameter S							
		Ar CH	Ar CH	γ-CH_2	chain CH_2	CH CH_2	chain CH=CH	ω-1 CH_2	CH_3
		123 ppm	121 ppm	28 ppm	29-30 ppm	32 ppm	131 ppm	24 ppm	14 ppm
- 43	1.1	13.6 0.65	13.6 0.65	7.4 0.35	6.6 0.31	8.0 0.38	13.6 0.65	5.3 0.25	-
0	2.1	-	-	5.7 0.27	5.1 0.24	4.6 0.22	11.0 0.52	4.3 0.20	> 3.0
25	1.2	14.0 0.67	14.0 0.67	4.5 0.21	3.5 0.17	3.0 0.14	-	-	-
35	2.1	6.2 0.30	4.5 0.21	5.3 0.25	4.4 0.21	3.5 0.17	7.3 0.35	4.0 0.19	3.5
45	2.1	6.0 0.29	5.6 0.26	5.0 0.24	4.5 0.21	3.4 0.16	6.2 0.30	4.0 0.19	3.0
100	2.1	5.7 0.27	5.7 0.27	4.3 0.20	5.2 0.25	3.5 0.17	5.5 0.26	5.0 0.23	-
100	2.2	-	-	2.8 0.13	2.85 0.14	2.3 0.11	5.4 0.26	2.4 0.11	0.5-1 ~0.09
140	2.1	5.6 0.26	5.6 0.26	4.2 0.20	5.5 0.26	5.4 0.26	4.5 0.21	4.8 0.23	-

Table 7.2 Dipolar coupling constants D [kHz], measured for the CH_n moiety; local dynamic order parameters S; **1.1** ^{13}C-^{1}H REREDOR, $t_{rcpl} = 1\ \tau_R$, MAS = 12.5 kHz; **1.2** ^{13}C-^{1}H REREDOR, $t_{rcpl} = 2\ \tau_R$, MAS = 12.5 kHz; **2.1** ^{13}C-^{1}H REPT-HDOR, $t_{rcpl} = 2\ \tau_R$, MAS = 12.5 kHz;; **2.2** ^{13}C-^{1}H REPT-HDOR, $t_{rcpl} = 4\ \tau_R$, MAS = 12.5 kHz;

The REREDOR measurements at 25°C provided a value of *ca.* 14 kHz for the ^{13}C -^{1}H couplings of the aromatic core CH moieties, a value which is reduced by a factor of 2/3, compared to the immobile CH coupling constant. This (as seen also from the proton 2D BaBa NMR spectra) indicates that the perylenetetracarboxydiimide core is not completely rigid even in the crystalline phase. It should be noted that the observed reduction factor is close to the value of 0.625 characteristic for phenyl flips[31] but the reduction could as well result from significant thermal fluctuations about the symmetry axis of the molecule.

Even cooling down to -43°C, aiming to freeze the core motion, resulted in the similar ^{13}C-^{1}H coupling constant of 13.6 kHz. The slight variation of 400 Hz difference between the D_{CH} values determined at ambient conditions and under cooling, is in the 5 % error range of the method and could be attributed to imperfections of the sidebands fitting procedure. Upon heating, the effective dipolar ^{13}C-^{1}H couplings of the core CH groups are reduced, reaching a value of 5.6 kHz corresponding to S = 0.27 at 140°C. Since the melting of the crystalline

phase starts above 178 °C, the dynamic processes causing the motional averaging of the dipolar couplings have to preserve the symmetry of the crystal lattice. Thus, 180° flips and strong fluctuations about the symmetry axis of the molecule are the most likely processes (Figure 7.5).

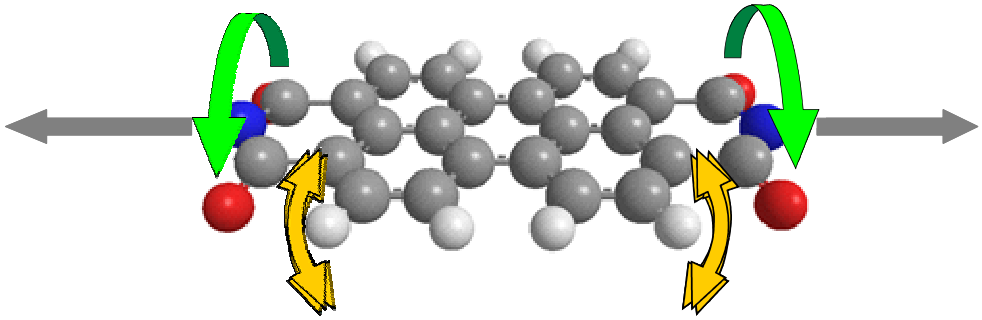

Figure 7.5 Schematic representation of the axial 180° flips and out of plane fluctuations of the PTCDI core (the $(CH_2)_8$-CH=CH-$(CH_2)_7CH_3$ side chains are not displayed) about the symmetry axis the molecule at elevated temperatures.

The dynamic behavior of the alkyl chains of PTCDI at ambient conditions reflects the characteristic gradient of mobilities along the chain, starting from an initial order parameter value of S = 0.21 for CH_2 units close to the perylene core down to S = 0.14 for the alkyl chain. The chemical structure suggests that the dynamic local order parameter of the methyne group should be elevated compared the other parts of the alkyl chain, because of the more stiff sp^2-hybridisation state of the double bond. This assumption was nicely confirmed by the experimental results as a function of temperature. Upon cooling down to -43°C the chains become less mobile with the CH=CH moiety being again the most rigid site. At these thermal conditions the methyne groups are characterized by a local dynamic order parameter S = 0.65 similar to that of the perylene core. Thus, two centres of relative rigidity, being linked by more mobile methylene moieties, are observed. Upon heating to T = 100°C, the effective couplings of segments in the alkyl chain apparently increase to an average dynamic order parameter value close to 0.2 and the gradient of mobility observed at ambient conditions vanishes. Increasing the temperature to T = 140°C does not further modify the order parameters. Only a minor decrease from S = 0.26 at T = 100°C to S = 0.21 at T = 140 °C is observed at the methyne position. Remarkably, at these temperatures the order parameter depends on the recoupling time (see Table 7.2) for all positions along the alkyl chain, apart from the methyne position. This suggests that the complex dynamic behaviour of the alkyl

side chains might be caused by a coupling of the dynamics of the rigid core and the stiff CH=CH group in middle of the chain via the more flexible alkyl chain.

7.3 Pure Phthalocyanine Derivative:

7.3.1 ^{1}H NMR spectroscopy:

The Pch2-($OC_{14,10}$)$_4$ proton NMR spectrum (not shown) recorded at fast spinning at ambient conditions confirmed the expectation of significant core and chain mobility of the sample in the liquid crystalline state (as determined also by DSC and optical microscopy). The fast molecular dynamics manifested itself in well resolved spectral peaks in both alkyl and aromatic regions. This was a prerequisite to use ^{1}H-^{1}H DQF NMR spectroscopy for investigating the Pc supramolecular arrangement as well as dynamics. The one dimensional experiments conducted at different excitation times revealed the most appropriate conditions for recording the 2D rotor synchronized experiment. In the two dimensional DQ BaBa spectrum recorded at 160 μs excitation time two diagonal auto peaks are observed due to DQCs among the aliphatic CH_2 protons (1.5 ppm, 3.0 ppm) and the well-isolated OCH_2 group (3.5 ppm, 7.0 ppm). In addition, cross-peaks due to DQCs among aromatic protons with inequivalent chemical shifts are detected in the aromatic spectral region. A careful examination of the spectral intensity and peak positions reveals that there are two proton pairs, with the corresponding chemical shifts (6.2 ppm and 6.4 ppm) and (5.8 ppm and 6.8 ppm), being coupled together.

The existence of two pairs of aromatic protons involved in a coherence when in the chemical structure there is only one such pair of inequivalent protons, can be attributed to two reasons. Possibly, ring current effects of neighbouring aromatic systems cause a high-field shift for some of the aromatic protons. However, in the mesophase the Pc discs are rotating about the columnar axis with fluctuations in both out-of-plain and off-axis directions and thus cause an averaging of the effects on the proton chemical shifts. Therefore, this hypothesis is not very likely to be true, but cannot be completely ruled out.

It is more likely that the asymmetric core substitution by alkyl chains (the Pc is a mixture of four regioisomers with different molecular symmetry) leads to the observed difference in the ^{1}H chemical shifts. Additionally, in the spectrum there are detected off-

diagonal peaks at (6.0 ppm, 7.5 ppm) and (1.5 ppm, 7.5 ppm) due to coherences between aromatic proton and protons from the alkyl chains.

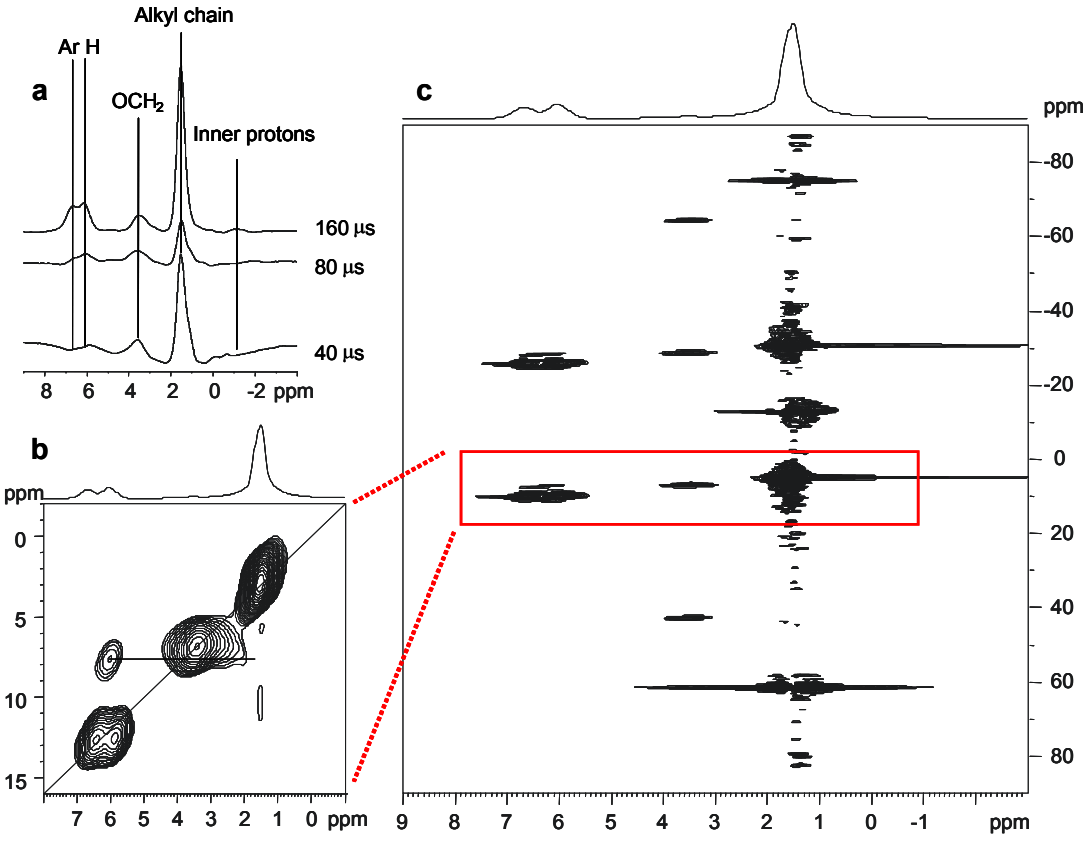

Figure 7.6 **a)** ^{1}H-^{1}H DQF BaBa NMR spectrum of Pch2-$(C_{14,10})_4$, recorded at 385 K effective temperature, 40 µs, 80 µs and 160 µs recoupling time and 25 kHz spinning at the magic angle. **b)** Rotor synchronized ^{1}H 2D DQ BaBa NMR spectrum (with the skyline projection on top) recorded with 160 ms excitation time at 25 kHz spinning at the magic angle with the evolution time set equal to the rotor period and **c)** the same experiment with the evolution period incremented

An interesting observations is that even though the inner core protons (Figure 7.6 **a**), which are situated close to each other participate in a coherence, in the two dimensional version of the experiment no diagonal peak was detected. Possible reasons are broad distribution of the chemical shifts of this type of protons, as well as relatively small amount in the sample, which results in weak signals in the noise level. It also might be interfering dynamics on the timescale of the MAS period, leading to destructive interferences and signal cancellation.

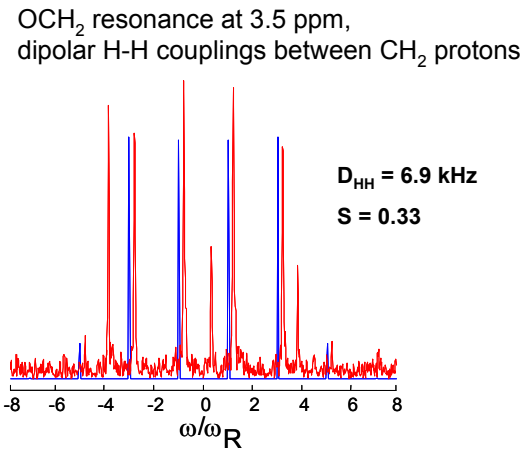

Figure 7.7 BaBa sideband pattern (red line – measured; blue line - calculated) for the OCH_2 resonance at 3.5 ppm.

To evaluate the coupling strength of the resolved homonuclear spin pairs, BaBa sidebands were recorded at 25 kHz MAS and 160 μs used to excite and reconvert DQ coherences. Due to the weak couplings between the aromatic protons (less than 2 kHz), only first order sidebands were observed. This implies, provided the geometry of the H-H dipolar coupling tensor, as well as the rotation of the discotic phthalocyanine molecule in the mesophase, significant out-of-plane motion (tumbling) of the discs, as only this type of motion would lead to reduction more than 50% of the dipole-dipole coupling between the aromatic protons.

The presence of fifth order sidebands in the BaBa spinning sideband pattern (Figure 7.7) allowed the evaluation of the ^1H-^1H dipolar coupling constant for the OCH_2 moiety with a good precision. The value of D_{HH} for the OCH_2 protons is in the range of 6.9 kHz, with the related local order parameter being S = 0.33.

7.3.2 ^{13}C NMR spectroscopy was employed to unravel the Pc molecular dynamics, as information about the dynamics of only one site was accessible using proton NMR approaches.

The ^{13}C CP spectra of the compound recorded at spinning frequencies in the range 12-30 kHz at low (-30°C) to ambient or even elevated (*ca.* 70°C) temperatures (examples presented on Figure 7.8) did not provide the expected chemical shift resolution in the carbon spectra.

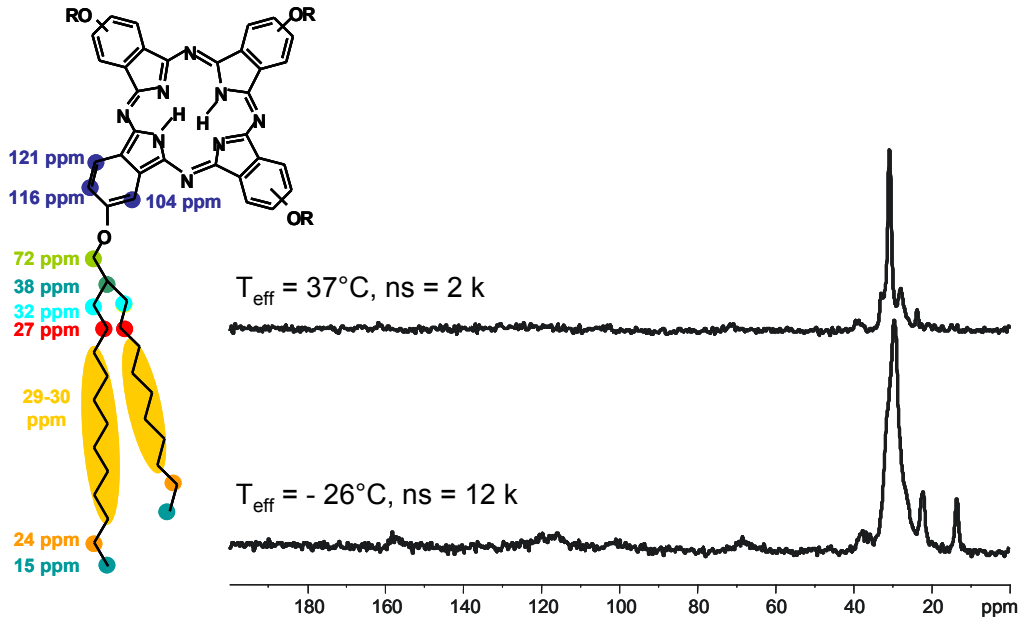

Figure 7.8 ^{13}C CP NMR spectra of Pch2-$(OC_{14,10})_4$, recorded at 25 kHz MAS, recycle delay of 4s, 1 ms cross-polarization contact time and **a)** 2k scans at 37°C and **b)** 12k scans at -26°C effective sample temperatures.

There was practically no ^{13}C signal from the aromatic core and the ^{13}C resonances of the chains were with low spectral intensity. The possible reason was unfavourable dynamics of the core motion related to the magic angle spinning frequency. Thus, a clear conclusion can be made about the Pc core (and alkyl chains, where the signal is significantly reduced) dynamics being in the kHz (10-30 kHz) motional regime in the temperature range -30°C ÷ 70°C. The only possible way to overcome the signal loss was increasing the temperature to the instrumental limit (thus enhancing the molecular dynamics) to avoid the unfavourable dynamics region. In addition, lower spinning speeds and 4 mm, instead of 2.5 mm, rotor were used to benefit from the bigger sample amount with the respective signal gain.

7.3.3 Molecular Dynamics

The ^{13}C-^{1}H REPT-HDOR NMR technique has been used to determine the ^{1}H-^{13}C dipolar couplings and thus local order parameters S from recorded sideband patterns. The experimental conditions were the same as for the perylene diimide derivative: 100°C and 140°C, 160 μs recoupling time and 12.5 kHz spinning at the magic angle. Both REREDOR and HDOR measurements at ambient conditions have been performed, but did not provide information about the core dynamics due to very poor signal intensity and a lack of rotor

modulation. The failure of the experiments is attributed to molecular tumbling with a correlation time similar to the MAS rotor period, which leads to destructive interferences during the recoupling procedure.

Thus, a site-selective study of the molecular dynamics, as described for the perylene derivative, is not feasible at ambient conditions. At T = 100°C, the effective dipolar couplings determined for the core CH moieties were in the range of 5.5-6.8 kHz, with the respective order parameter S = 0.26-0.32, depending on the CH position in the phthalocyanine core. Rapid rotation about the fourfold molecular symmetry axis of the phthalocyanine in the mesophase with additional out-of-plane excursions with a $\sigma = 20°$, assuming a Gaussian distribution of the fluctuations, well explains the reduced dipole-dipole coupling constants values. It should be noted, however, that any motion of the compound in the µs or less time scale, might lead to the observed dipolar coupling constants values. Thus, a stronger tumbling of the stacked phthalocyanine molecules ($\sigma = 30°$) in the disc plane without rotation, though not very likely, should also be considered.

T [°C]	NMR Method	Dipolar coupling constants D [kHz], measured for the CHn moiety; local dynamic order parameter S							
		Ar CH	Ar CH	Ar CH	OCH_2	chain CH	CH CH_2	δ CH_2	chain CH_2
		121 ppm	116 ppm	104 ppm	72 ppm	38 ppm	32 ppm	27 ppm	29-30 ppm
40	1	-	-	-	-	-	6.0 0.29	4.5 0.21	2.0 0.10
72	1	-	-	-	-	-	4.0 0.19	-	3.0 0.14
100	1	6.8 0.32	5.5 0.26	6.0 0.29	-	6.0 0.29	-	-	3.5 0.17
140	1	6.0 0.29	5.6 0.27	5.9 0.28	5.5 0.26	5.5 0.26	-	-	2.5 0.12

Table 7.3 Dipolar coupling constants D [kHz], measured for the CH_n moiety of Pc; local dynamic order parameters S; **2** ^{13}C-^{1}H REPT-HDOR, $t_{rcpl} = 2\ \tau_R$, MAS = 12.5 kHz

Remarkably, further heating to 140°C has no major influence on the effective dipole-dipole couplings for the core CH moieties: the effective coupling values determined at T = 140°C are in the range of 5.6 and 6.0 kHz and the derived local order parameters S = 0.27 - 0.29. The smaller spread of S values for the aromatic CH groups observed at higher temperature is indicative for a more uniform molecular dynamics of the Pc core, compared to its behavior at lower temperature. These results already suggest that further heating up to the

melting point (180°C) of the sample, which is not feasible due to NMR hardware limitations, would not change substantially the dynamic behavior of the core.

The $C_{14,10}$ side chains of the phthalocyanine derivative exhibit a gradient of mobility at 100°C. The dynamic order parameter at the chain branching position $S_{branch} = 0.29$ corresponds to the value of the core, whereas the average order parameter of the methylene units along the chain has been determined to be $S_{chain} = 0.17$. As expected, raising the temperature from 100°C to 140°C does not change the gradient of mobility and causes only a minor reduction of these order parameters ($S_{branch}= 0.26$, $S_{chain}= 0.12$).

7.4 75:25 Pc:PTCDI blend

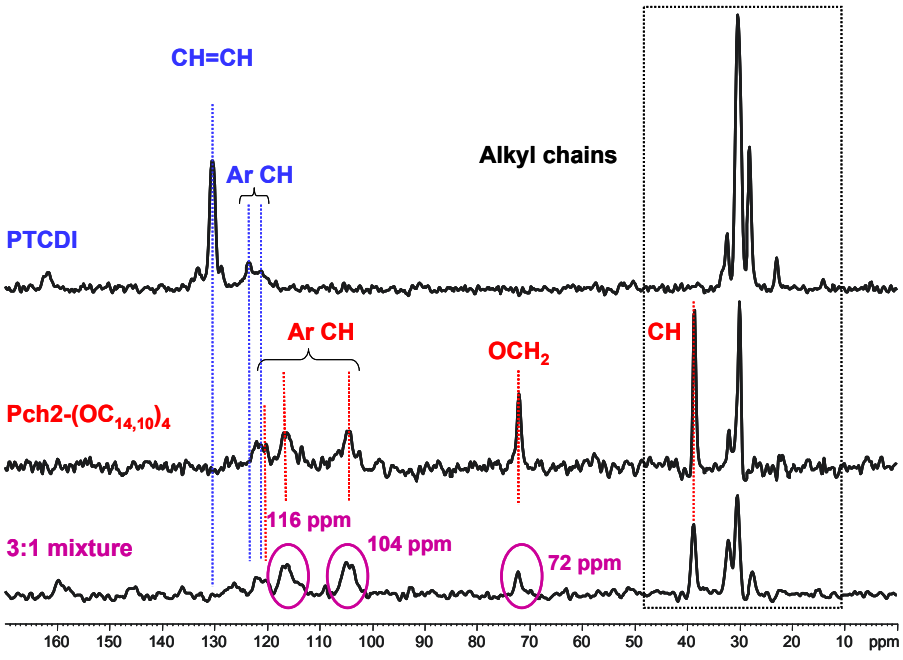

Figure 7.9 ^{13}C CP NMR spectrum, recorded at 140°C, 12.5 kHz magic angle spinning and 4 s recycle delay for the mixture and the two components. Pch2-$(OC_{14,10})_4$ and the mixture are in the mesophase; PTCDI is in its plastic crystalline state.

This system has been studied using the REPT-HDOR NMR technique. In order to evaluate the mobility of both components of the blend, spectral separation of the signals resulting from the different components is needed. This requirement, however, is not fulfilled here, because most of the signals of the PTCDI aromatic core overlap with signals from the Pc core. Nevertheless, two signals from the Pc core (at 104 and 116 ppm) are unaffected by signals from the other component (Figure 7.9), so that the dynamic behavior of the Pc

component in the blend can be investigated. The study is compared with X-ray data (Figure 7.11) which show that the symmetry of the Pc columnar hexagonal mesophase is not affected by the addition of PTCDI. Moreover, addition of PTCDI up to 40% stabilizes the phase and extends its existence to a broader temperature range.

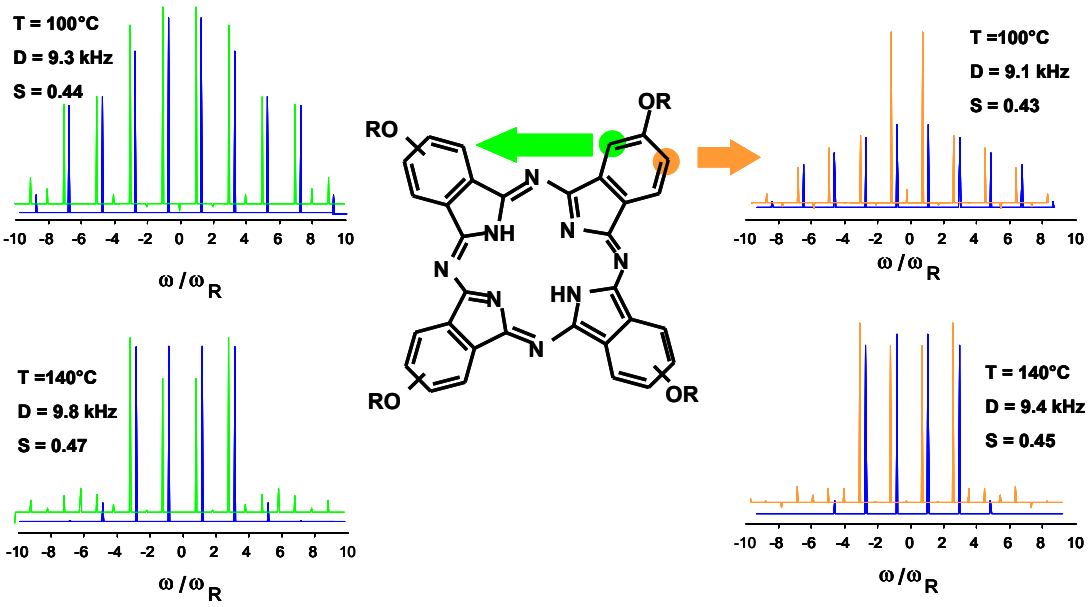

Figure 7.10 REPT-HDOR sideband patterns, recorded at 12.5 kHz MAS, and 320 µs recoupling time and 100°C and 160 µs recoupling time and 140°C, with the simulated patterns (blue) superimposed. The effective ^{1}H-^{13}C dipolar coupling constants, derived from the sideband patterns, together with the related local order parameters, S, are presented. R = $C_{14,10}$

The measurements have been performed at 12.5 kHz MAS under conditions comparable to those for the pure Pc sample. At T = 100°C, the local order parameters are S = 0.43 and S = 0.44 for the two accessible sites (Figure 7.8) of the Pc-core. Comparing these values with the local order parameters of the same sites in the pure Pc-sample (S = 0.26 and S = 0.30), an increase of the order parameter by about 50% is found upon addition of PTCDI. Moreover, the local order parameter of the Pc-component in the blend slightly increases to S = 0.46 on raising the temperature to T = 140°C (Figure 7.10).

Similar to the signals of the aromatic core, most of the signals of the aliphatic side chains of Pc and PTCDI are superimposed and cannot provide further information on the dynamic behaviour of the Pc molecules in the mixture. However, the signal of the Pc OCH_2 group is well resolved, and confirms the findings for the dynamic behavior of the aromatic

Pc-core in the mixture. At T = 140°C, the OCH_2 group exhibits a dynamic order parameter as high as S = 0.47 compared to S = 0.26 in the pure compound at the same temperature.

Considering the NMR results (discussed so far) and X-ray data (presented below) both showing significantly increased supramolecular order in the blend compared to the predominant phthalocyanine derivative, a model where the perylene molecules intercalate within the phthalocyanine columns has been proposed.

7.5 Supramolecular organization of the blend

"Knowledge is power"

Sir Francis Bacon

"Imagination is more important than knowledge. For knowledge is limited…"

Albert Einstein

Although there is no direct spectroscopic proof of intercalation of the perylene molecules into the phthalocyanine columns in the liquid-crystalline state, one can safely claim this being the case. The logical way to reach such a conclusion is first to identify all possible supramolecular organizations and consequently, based on the available spectroscopic data, to exclude the possibilities one by one until only one (which does not contradict the data) remains. Considering the way of mixture preparation (mixing the respective components of the blend and melting the mixture with the consecutive annealing and slow cooling down) there are four possibilities, namely:

1. The two compounds of the blend phase separate, each forming columns in the mesophase

2. The phthalocyanine derivative forms a columnar phase in the liquid-crystalline state, while the perylene molecules are situated in the melt between the columns thus restricting the phthalocyanine side chain motion and respectively reducing the phthalocyanine core fluctuations. This would result in higher local dynamics order parameter S for the phthalocyanine core.

3. The two compounds form statistical mixture where both perylene and phthalocyanine derivatives participate in the columns formation in the mesophase

4. Alternating regions (of different size) of the pure compounds in a column; the two regions being arbitrarily distributed in the different columns.

Taking into account the X-ray data presented on Figure 7.11 as well as the thermotropic behaviour of the pure compounds and the blend (see table 7.1) each of these possibilities will be examined separately.

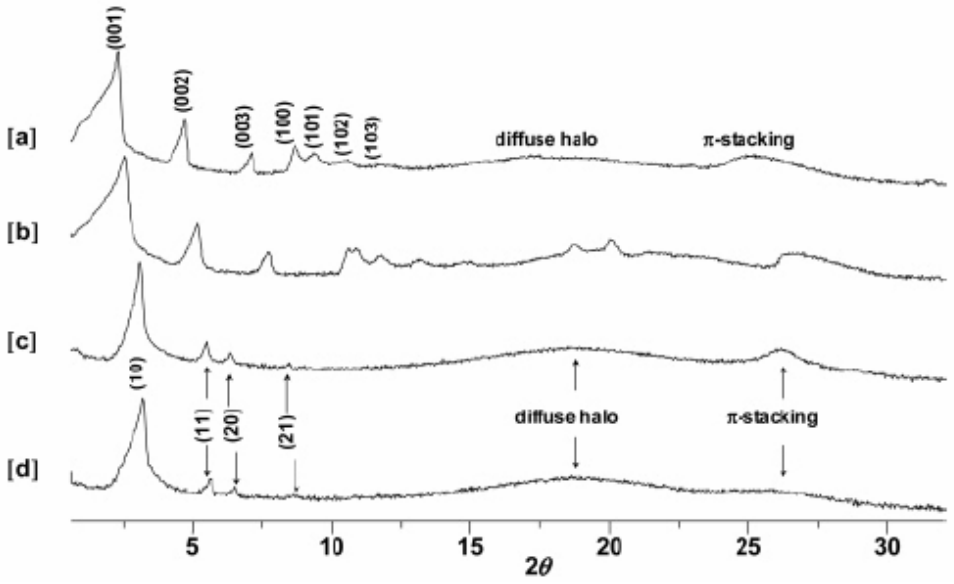

Figure 7.11 X-ray diffractograms of PTCDI at 200°C **[a]**, and 100°C **[b]**, 3:1 blend at 100°C **[c]** and Pc derivative at 100°C **[d]**

1. Phase separation of the compounds would be expected and indeed occurs for molar ratios where the perylene derivative exceeds 25%. For the 3:1 blend, however, no indications of phase separation are present. Furthermore, no mechanism explaining the improved local dynamic order parameters in the phthalocyanine columns could be identified.

2. The concept of the lath-like aromatic perylene derivative molecules being "dissolved" in the molten phthalocyanine chains though providing some vague explanation for the improved columnar order and π-stacking (by restricting the chain motion with consecutive reduction of the Pc core out-of-plane fluctuations) contradicts the X-ray data. If the perylene molecules were present in the Pc intercolumnar space, this would lead to larger

intercolumnar distances, which is not observed in the X-ray measurements. On the contrary, the intercolumnar distance remains precisely the same as in the pure Pc compound. Moreover, no driving force can be identified leading to a "dissolution" of an aromatic compound in an aliphatic environment. These arguments seem sufficient to exclude this option.

3. The concept that perylene molecules intercalate within the phthalocyanine columns seems to be most likely. On one hand, it does not contradict the WAXS spectra and on the other, π-stacking combined with donor-acceptor interactions between the aromatic cores of the two compounds[147,148] in the mixture are defined as the driving force for the intercalation phenomenon. In addition, the frustration phenomenon[148,149] (arising from differences in the closer packing of the aromatic cores compared to the aliphatic chains) does not arise (or is less or even inverted compared to the pure Pc compound case). As known[149], this phenomenon can be solved either by a tilt of the aromatic moieties or by a density modulation of the aromatic core packing along the column. In this case (PTCDI intercalated in the Pc columns), the perylene derivative with its two long alkyl chains does not have the significant spatial requirements of the four branched chains of the phthalocyanine compound. On the contrary, it provides additional space to "accommodate" the $C_{14,10}$ dove-tailed chains and thus stabilizes the system thermodynamically as well. However, it remains unclear, which of the mechanisms discussed is responsible for the improved π-π stacking and intracolumnar order of the blend.

It should also be noted the possibility that two perylenes (being almost two times smaller compared to a phthalocyanine molecule) might intercalate together the phthalocyanine column, thus optimizing the space filling, respectively leading to a more dense packing.

4. Having regions of different length in a single column with arbitrary distribution in the columns in the mesophase would not contradict the WAXS data. However, statistically this option is not very likely. In addition, no mechanism leading the observed improved intracolumnar order, apart from solving the frustration phenomenon can be identified.

7.6 Conclusions:

1. The PTCDI compound has plastic crystalline-like behaviour in the crystalline state. The perylene derivative exhibits a gradient of mobility along the alkyl chains in a wide temperature range with the CH=CH moiety being, together with the aromatic core, a centre of relative rigidity. Investigation of the behavior of the pure perylene derivative in the mesophase was not possible due to hardware limits. Rotation of the perylene molecules in the mesophase about the columnar axis is possible; however, the preferential motion for the lath-like perylene is associated more with its axial symmetry axis.
2. The pure phthalocyanine derivative is characterized by an unstable disc rotation in the mesophase with significant out-of-plane fluctuations.
3. Solid state NMR studies of the molecular dynamics show improved order in the phthalocyanine columns in the mixture compared to the single Pc compound.
4. Improved π-π stacking in the phthalocyanine columns in the 3:1 molar blend compared to the single phthalocyanine derivative detected by WAXS.
5. Based on the combined WAXS - solid state NMR study, a model about the supramolecular organization of the blend is proposed, namely - intercalation of the perylene molecules within the phthlocyanine columns of stacked discs (Figure 7.12).

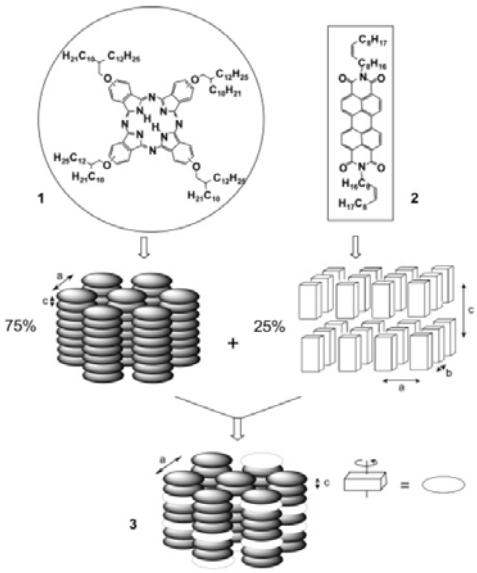

Figure 7.12 Molecular structures of Pc **1** and PTCDI **2** (top); supramolecular arrangement of **1**, **2** and **3** (bottom)[142]

Chapter 8. Order and Dynamics of Supramolecular Architectures:

Solid State NMR on Polylysine Substituted Polyphenylene Dendronized Perylenetetracarboxydiimides

8.1 Secondary Conformations of Peptides

There are different *levels of organization* of peptides and proteins, and each level is termed a structure. The first level, or *primary structure*, is the arrangement (sequence) of amino acids in a polypeptide chain. *Secondary structure* refers to the spatial arrangement, or conformation, of relatively short segments of the polypeptide chain. The *tertiary structure* of a protein reflects how the elements of the secondary structure are organized in respect to each other. Finally, *quaternary structure* refers to the organization of different subunits or monomers of a protein complex.

The conformation of the polylysine chains is of particular interest in the following study. For this reason, the elements of the secondary structure will be briefly discussed below.

It is important to mention that the peptide (amide) bond between the carboxyl and the amine group of two amino acid residues has partial double bond character. The reason is the existence of two resonant structures as seen on Figure 8.1 a.

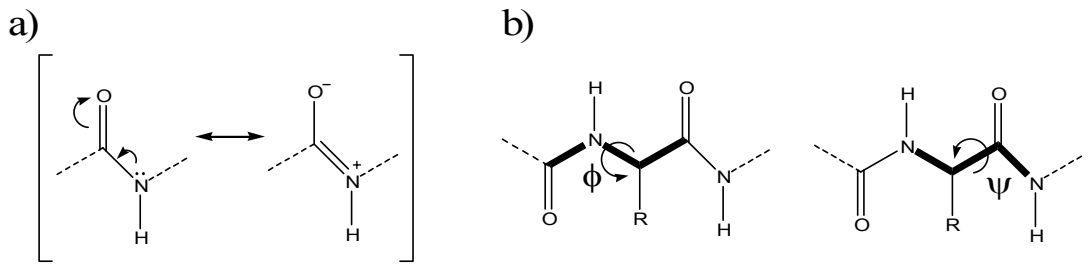

The C-N distance obtained from X-ray measurements between the carbon and nitrogen atoms in the amide bond is 1.32 Å. This is shorter than the single bond C-N distance (1.45 Å) and longer than the double bond C=N distance (1.20 Å). This partial double bond character means that the constituents of the peptide bond all lie in the same plane. In addition, the dihedral angle associated with the double bond, ω, can only adopt two values – 0° or 180°. It is the dihedral defined by $C\alpha_{(i-1)}$, $C`_{(i-1)}$, $N_{(i)}$ and $C\alpha_{(i)}$, where *i* refers to the residue number in the polypeptide chain. Due to the steric requirements of the side-chains (residues) attached to the backbone CH carbon atom, in most cases, ω is equal to 180°, i.e. the residues

adopt alternating *trans*-positions in respect to the peptide chain. If we consider the other atoms of the backbone, two more dihedral angles define the shape of the backbone. One involves the $C`_{(i-1)}$, $N_{(i)}$, $C\alpha_{(i)}$ and $C`_{(i)}$ atoms, and is called the *phi* (ϕ) angle, and the other one involves $N_{(i)}$, $C\alpha_{(i)}$, $C`_{(i)}$ and $N_{(i+1)}$, and is called the *psi* (ψ) angle (Figure 8.1 b). Since both angles ϕ and ψ are associated with single bonds, they can adopt virtually all conformations. However, due to steric hindrance between the neighboring substituent, these angles can only adopt (or populate) certain range of angular values. A three-dimensional plot of these angles versus the energies of the different conformations, called Ramachandran plot, conveniently presents the allowed (or preferred) conformations.

α-helix: In an α-helix segment with the ϕ angles ~ -60° and the ψ angles ~ -50° for all residues, the polypeptide backbone curls up (to the right) around an imaginary axis. Each full turn of the *right handed α-helix* thus formed, has a height of 5.4 Å and involves 3.6 amino acid residues (which is also called the pitch of a helix). The helical structure is stabilized by hydrogen bonds between the amide $N_{(i)}$-H hydrogen and the carbonyl oxygen $C`_{(i+3)}$, i.e. three residues away (As the energy of a single H-bond varies between 2 and 5 Kcal/mol, the stabilization energy of an α-helix increases proportionally to the number of H-bonds formed). Another important feature of the α-helix is its polarity, which arises due to the orientation of the polar carbonyl groups in the same directions (the carbonyl oxygen points to the C-terminus and the carbonyl carbon to the N-terminus). Thus, all dipoles add to provide a huge dipole moment of an α-helical secondary conformation. In addition, due to the specific geometry of the α-helix, all side groups point outside the helical axis.

β-sheet: The so-called *β-strand* corresponds to a partially extended polypeptide backbone structure characterized by dihedral angles $\phi = -120°$ and $\psi = 140°$. In a β-strand the unfavourable steric hindrance is reduced by zigzagging of the polypeptide backbone. In an isolated β-strand there are no H-bonds stabilizing the conformation. However, such stabilization is achieved by combining several β-strands in layered structures known as β-sheets, where H-bonds are formed between adjacent β-strands. Depending on the direction of the strands there are two types of β-sheets – parallel and antiparallel. Due to the disposition of the H-bonding donor and acceptors, the H-bonds in a parallel β-sheet are less stabile compared to the antiparallel one.

collagen helix (polyproline II helix): The structural element, characterized by dihedral angles $\phi = -70°$ and $\psi = 160°$, is not as extended as the β-strand and not as curled as

the α-helix, and is known as collagen helix. It is left handed with only three residue units per turn. In collagen the segment –Gly-Xaa-Pro- and –Gly-Xaa-(HO)Pro- is often found. Three of these single stranded helices coil up together forming a triple helix. The latter provides the tensile strength characteristic for tendons.

polypeptide turns: As the name implies these introduce a sharp change in the direction of the polypeptide backbone. **β-turn** is the most abundant type, which involves four amino acid residues. The β-turn is stabilized by H-bond between the amide carbonyl oxygen of residue (i) to the amide hydrogen of the residue (i+3). Depending on the values of the <ϕ,ψ> angles of residues (i+1) and (i+2), there are up to eight types of β-turns distinguished. **γ-turns** involve only three residues of the polypeptide and are stabilized by an H-bond between the amide carboxyl oxygen of residue (i) to the amide hydrogen of residue (i+2). Since they involve less residues, they are more open than the β-turns. Also, compared to β-turns the geometry of the H-bond formed is less optimal and thus γ-turns are less favourable energetically and respectively less common.

random coil: Polypeptide segments, which do not have any of the conformations discussed above are considered as being in a random coil conformation. The term "random" is not precise as the conformation might be very well defined, but changing fast on the time scale of the methods used to investigate the secondary structure (X-ray and NMR spectroscopies) and thus difficult to be described. Typical random coil segments are the N- and C-terminus of the polypeptide backbone, as well as the polypeptide loops connecting different β-sheet or α-helical backbone regions.

8.2 Introduction

Drug delivery systems such as lipid- or polymer-based nanoparticles can be designed to improve the pharmacological and therapeutic properties of drugs. Advancement of polymer chemistry has led to nano-scale construction capabilities with a potential in designing novel drug delivery systems.[150,151] Dendrimer chemistry is considered a pioneering tool for such applications since it offers ideal dimensions, monodispersity, solubility, biocompatibility, unique spherical shape that, in addition, is highly functionalizable.[152-155]

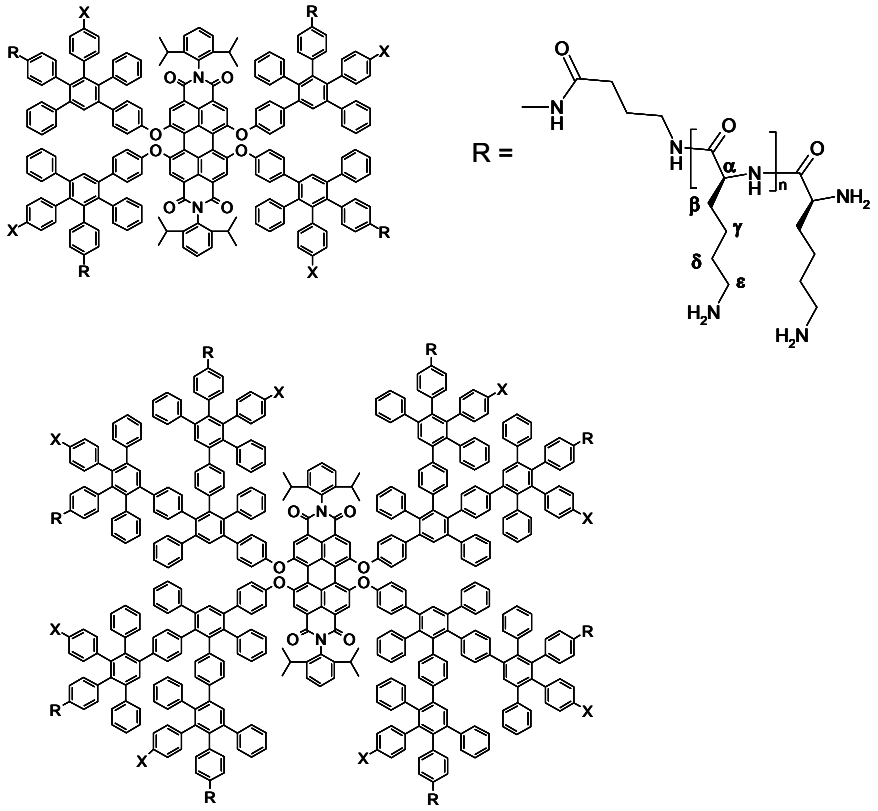

Figure 8.1 Polyphenylene scaffold of dendrimers of the first (top) and second (bottom) generation. X is either H or R. The repeat unit of lysine R is also shown together with the assignment of the different carbons.

Recently, the synthesis and conformation of dendronized polymers based on a poly-L-lysine backbone[156] as well as the synthesis of L-lysine dendronized polystyrene[157] has been reported. Dendrimers based on poly-L-lysines have attracted interest for the possible development of multiple antigen peptides or as nonviral gene delivery systems.[158,159] An interesting finding in the study of dendronized polymers based on the poly-L-lysine backbone with attached polyester dendrons was the observation of a transition from a compact α-helical backbone to a disordered yet extended conformation with increasing dendron size.[156] Steric repulsions between the dendrons were thought to be responsible for the observed helix to coil transition. Recent progress in this direction has been the development of synthetic routes leading to peptide-functionalization of polyphenylene dendrimers.[160,161] These molecules are monodisperse, shape-persistent, with topologically isolated, non-interacting functional groups that are employed as scaffolds for the attachment of poly-L-lysines giving rise to core-shell nanostructured materials. In addition, polyphenylene dendrimers bearing the fluorescent perylenediimide core provide with the possibility of optical detection of the dendritic conjugates.

Table 8.1. Molecular characteristics of the PDI dendrimers

Sample	Generation	X	$n_{Lys,\ UV}$[a]	$n_{Lys,\ GPC}$[b]	M_w/M_n[c]
30a	1	H	9	14	1.11
30b	1	H	50	54	1.16
30c	1	H	85	84	1.15
31a	1	R	9	12	1.09
31b	1	R	68	60	1.08
31c	1	R	76	74	1.10
32a	2	H	6	9	1.17
32b	2	H	28	22	1.42
32c	2	H	41	37	1.27
33a	2	R	14	16	1.26
33b	2	R	41	58	1.50
33c	2	R	89	68	1.42

[a]: number of peptide residues per chain obtained from UV
[b]: number of peptide residues per chain obtained from GPC
[c]: polydispersity of the peptide-dendrimer conjugates calculated from gel permeation chromatography, obtained in DMF against polystyrene standards.

In the present study a series of poly-L-lysine functionalized polyphenylene dendrimer analogues[161] with different polyphenylene core sizes, functionality and peptide degree of polymerization (of the type $G_xF_yN_z$, where G, F and N stands for the generation, functionality and peptide degree of polymerization, respectively with values in the range: $1\leq x\leq 2$, $4\leq y\leq 16$ and $9\leq z\leq 84$ (Table 8.1 and Figure 8.1)) has been investigated.

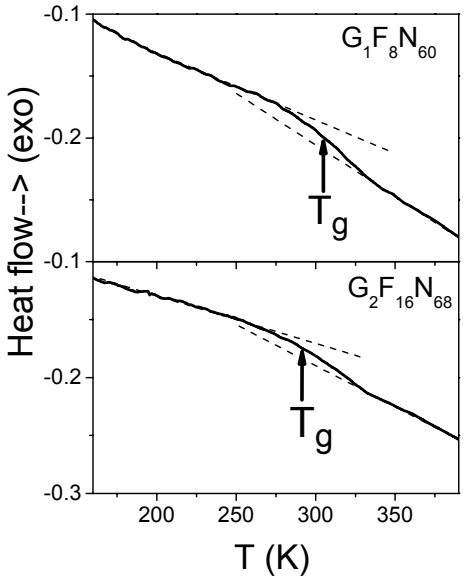

Figure 8.2 DSC traces obtained during the second heating run (rate 10 K/min) from two poly-L-lysine functionalized polyphenylene dendrimers of the first ($\mathbf{G_1F_8N_{60}}$) (top) and second ($\mathbf{G_2F_{16}N_{68}}$) (bottom) generation. The arrows indicate the corresponding glass temperatures.

The aim has been to study by solid state NMR and X-ray scattering the dependence of the conjugates self-assembly on the length of the polypeptide and the polyphenylene generation. Model linear poly-L-lysine compounds ($Plys_{20}$ and $Plys_{59}$) are used as reference systems for comparison. In addition, by applying site-specific solid state NMR heteronuclear recoupling techniques the polypeptide and polyphenylene dynamics as well as the associated dynamic order parameters in the melt state (see Figure 8.2) have been investigated.

8.3 Self-Assembly of the Poly-L-lysine Dendrimers

It is now well-established that the ^{13}C chemical shifts are sensitive probes of the local peptide conformation and thus the ^{13}C cross polarization – magic angle spinning (CPMAS) technique has been widely employed in identifying the main polypeptide secondary structures (α-helices and β-sheets)[162,163].

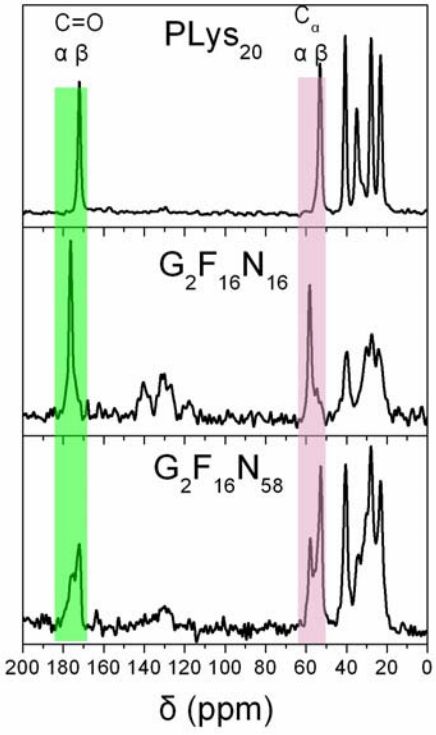

Figure 8.3 ^{13}C CP NMR spectra, recorded at 30 kHz MAS and 1 ms cross-polarization time, of a linear poly-L-lysine (**$Plys_{20}$**) and two of the poly-L-lysine functionalized polyphenylene dendrimers with N=16 (**$G_2F_{16}N_{16}$**) and N=58 (**$G_2F_{16}N_{58}$**). The C_α (δ ~ 53-58 ppm) and amide C=O (δ ~172-176 ppm) resonances suggest that $Plys_{20}$ has solely the β-sheet form whereas the peptide functionalized polyphenylene dendrimers form predominantly α-helices (**$G_2F_{16}N_{16}$**) or a mixture of β-sheets and α-helices (**$G_2F_{16}N_{58}$**). The solid state NMR results on the peptide secondary structures of the series are summarized in Table 8.2.

The conformation-dependent chemical shifts arise from the local conformations of individual amino acid residues characterized by the dihedral angles (ϕ and ψ) and the type of hydrogen bonding (i.e., intra- or intermolecular). Figure 8.3 gives some representative spectra of a linear poly-L-lysine ($Plys_{20}$) and two of the dendronized poly-L-lysines of the second generation with 16 (33a) and 58 (33b) aminoacids at 313 K.

Table 8.2 Secondary structures of the poly-L-lysine functionalized polyphenylene dendrimers, as determined by WAXS and solid state NMR. The local dynamic order parameters of the aromatic core, the peptide backbone and the side groups are presented together with the out-of-plane excursion angles[20], characteristic for each individual segment in the course of its motion.

Sample	N	Secondary structure		aromatic core	peptide backbone	peptide side groups** (C_β, C_γ, C_δ CH_2)		(C_ε CH_2)	
		NMR	WAXS	Order parameter *S*	Order parameter *S*	Order parameter *S*	Excursion angle (°)	Order parameter *S*	Excursion angle (°)
$G_2F_8N_9$	9	dis *	-	0.95	-	0.67	40	0.45	60
$G_1F_8N_{12}$	12	-	-						
$G_1F_4N_{14}$	14	dis *	-	~1	0.95	0.69	36	0.55	50
$G_2F_{16}N_{16}$	16	α	α (hcp)	0.90	0.95	0.67	40	0.60	47
$G_2F_8N_{22}$	22	α	α (hcp)	~1	0.95	0.50	54	0.50	54
$G_2F_8N_{37}$	37	α	α (hcp)	~1	0.95	0.53	52	0.35	82
$G_1F_4N_{54}$	54	α/β (3/1)	α (hcp)	~1	0.95	0.48	58	0.30	90
$G_2F_{16}N_{58}$	58	β/α (2/1)	-	~1	0.95	0.50	54	0.50	54
$G_2F_{16}N_{68}$	68	α/β (1/1)							
$G_1F_8N_{74}$	74	-	α (hcp)						
$G_1F_4N_{84}$	84	β/α (1/1)	-	~1	0.95	0.55	50	0.50	54
$Plys_{20}$	20	β							
$Plys_{59}$	59	α/β (1/1)							

* disordered state with ill-defined secondary structures.
** a gradient of mobility along the peptide side groups from the rigid core towards the side chain ends is found for most of the compounds, studied by solid state NMR. The presented local order parameters and the related excursion angles are an average of the site-specific *S* values and excursion angles of the C_β, C_γ and C_δ methylene groups. The terminal C_ε CH_2 group, being the most mobile, is discussed separately.

In the $Plys_{20}$ pattern the strong resonances with chemical shifts at 172 and 53 ppm arise from the amide C=O and C_α, respectively and suggest the formation of β-sheets. In

contrast, a longer linear Poly-L-lysine ($Plys_{59}$) displays two amide C=O resonances at 176 and 171.5 ppm as well as two C_α resonances at 58 ppm and 53 ppm with relative intensities suggesting a 35:65 α-helix to β-sheet ratio. Interestingly, in the dendronized polylysine 33a with n=16 the single C=O and C_α resonances are at 176 ppm and 58 ppm, respectively, revealing a pure α-helical secondary structure in contrast to $Plys_{20}$.

In fact, an α-helical secondary structure is the only peptide conformation for the dendronized polylysines with intermediate degrees of polymerization ($16 \leq n \leq 37$) independent of generation and functionality. On the other hand, in the dendronized polylysines with the shorter peptides ($n \leq 14$) a mixture of the two secondary structures was found with a majority of β-sheets. Presumably, these oligopeptides are too short to stabilize an α-helical structure. For the longer polylysines $n \geq 54$, a mixture of both secondary structures is formed as revealed by the spectrum of 33b in Figure 8.3. The results for the secondary structures from all samples are summarized in Table 8.2.

These results suggest an effect of the polyphenylene core on the peptide secondary conformation. This is especially the case for the dendronized polylysines with intermediate degrees of polymerization that form pure α-helices in contrast to their linear counterparts. To investigate further the reason for this effect X-ray scattering at the appropriate length scales has been used.

Small-angle X-ray scattering (SAXS) revealed a broad peak with corresponding distances that reflect polyphenylene core-to-core correlations. The intensity and sharpness of the peak is a function of the number of polylysine residues; the shorter the polylysine the better resolved the SAXS peak. This is shown in Figure 8.4 for the 31 series as a function of polylysine length (n=12, 60, and 74, respectively, for 31a, 31b and 31c). The broad peak at $q \sim 2.25$ nm^{-1} in 31a results in a characteristic distance of 6.7 nm (assuming only nearest neighbor correlations, i.e., $d = 1.23 \times 2\pi/q$). This distance is a function of generation, clearly demonstrating as reflecting correlations between the polyphenylene cores. These correlations become very weak for the longer polylysines as shown by the absence of a SAXS peak for 31b and 31c in the SAXS patterns of Figure 8.4.

WAXS was employed for two reasons: first, to identify the peptide conformation in the conjugates, in comparison to the NMR results, and second, to estimate their lateral coherence (packing efficiency). With respect to the type of secondary structure the WAXS images from extruded fibers (Figure 8.5) revealed hexagonally packed α-helical structures for the peptide substituted polyphenylenes dendrimers with the longer poly-L-lysines.

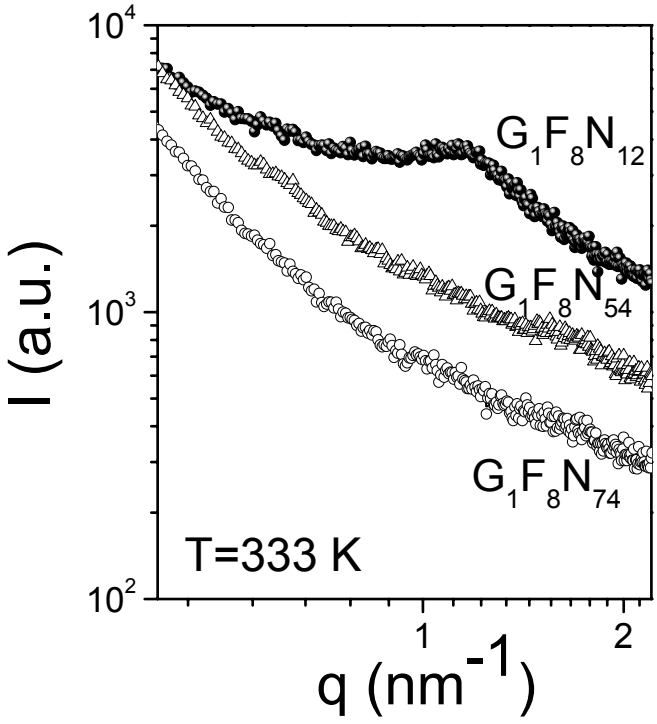

Figure 8.4 SAXS curves from three first generation peptide functionalized polyphenylene dendrimers as a function of the poly-L-lysine degree of polymerization: N=12 (**$G_1F_8N_{12}$**), N=60 (**$G_1F_8N_{54}$**) and N=74 (**$G_1F_8N_{74}$**). Notice the broad peak at q~1.15 nm^{-1} (with corresponding distances at *l*~ 6.7 nm) that is absent in the dendrimers with the longer poly-L-lysines.

As an example, in Figure 8.5 the two-dimensional image and the total integrated intensity from **$G_1F_8N_{74}$** (N=74) is shown. The integrated intensity profile contains strong equatorial reflections at relative positions $1:3^{1/2}:4^{1/2}$ suggesting hexagonally packed α-helices and a broader reflection with a corresponding spacing of ~ 0.5 nm originating from inter-atomic distances. The type of secondary structure is generally in good agreement with the NMR results (Table 8.2).

In addition to the type of the peptide secondary structure, the WAXS images revealed a correlation between the poly-L-lysine length and their lateral packing efficiency; the WAXS patterns exhibit sharp reflections associated with the lateral spacing of α-helixes only for the longer poly-L-lysines (as in Figure 8.5 right, for the G_2F_8 series), and the longer the poly-L-lysine, the better resolved the hexagonal reflections of α-helices. This suggests a coupling between the longer-range core-to-core correlations (SAXS) with the shorter range correlations originating from the packing of α-helices (WAXS).

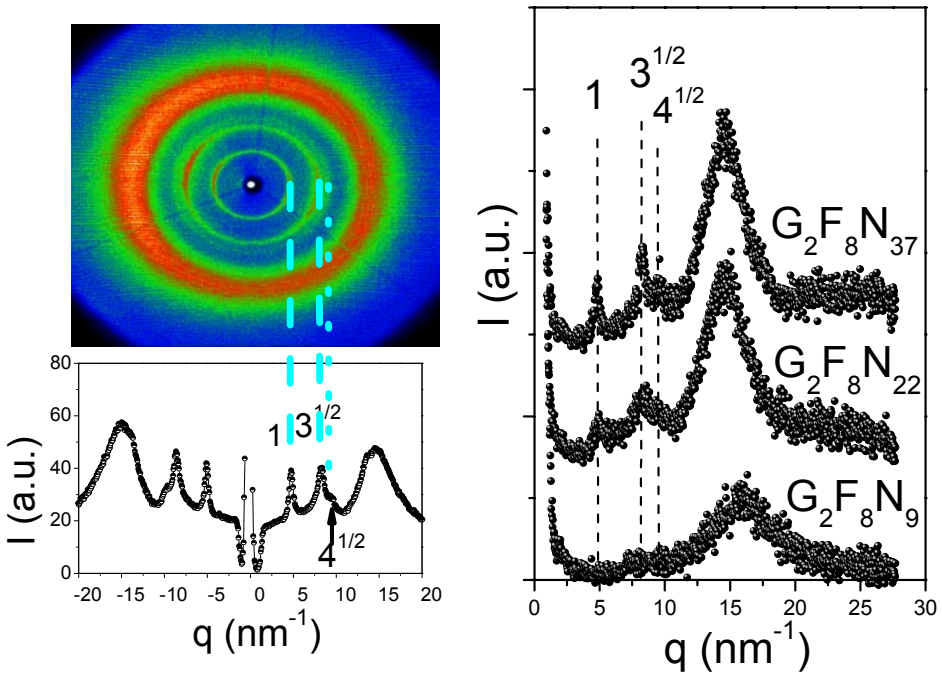

Figure 8.5 (Left): Two-dimensional wide-angle X-ray diffraction pattern from an oriented $\mathbf{G_1F_8N_{74}}$ fiber (extruded at 423 K and measured at 303 K). The total integrated intensity profile obtained from the 2-d pattern is shown together with the positions of the most intense reflections with relative positions at $1:3^{1/2}:4^{1/2}$ suggesting hexagonally packed poly-L-lysine α-helices. (Right): Dependence of the WAXS reflections (obtained with a θ-θ diffractometer) on the poly-L-lysine degree of polymerization. The G_2F_8 series is shown with N=9 ($\mathbf{G_2F_8N_9}$), N=22 ($\mathbf{G_2F_8N_{22}}$) and N=37 ($\mathbf{G_2F_8N_{37}}$) at 303 K. Notice the intense reflections with relative positions at: $1:3^{1/2}:4^{1/2}$ for the longer poly-L-lysines.

For the peptide substituted polyphenylenes dendrimers with the short polypeptide chains (N<16) the secondary structure is ill-defined, consisting mostly of random conformations as well as some extended conformations and α-helices (as determined by solid state NMR) attached into the polyphenylene cores. The latter possess some correlations between their centers and give rise to the SAXS peak. These oligolysines exhibit only weak lateral correlations within their secondary structures as shown by the very weak WAXS reflections (Fig. 8.5).

In contrast, the substituted polyphenylenes dendrimers with the longer polypeptides (N>20) lack correlations among their polyphenylne cores but do show improved lateral correlations between their secondary structures that assemble into hexagonally packed α-helices (Fig. 8.5).

This situation in the poly-L-lysine substituted polyphenylene dendrimers is depicted in a schematic way in Figure 8.6. The Figure exhibits the core-to-core correlations for the

shorter polylysines that are absent in the longer ones. In the latter case, however, the α-helices self-assemble into a hexagonal lattice.

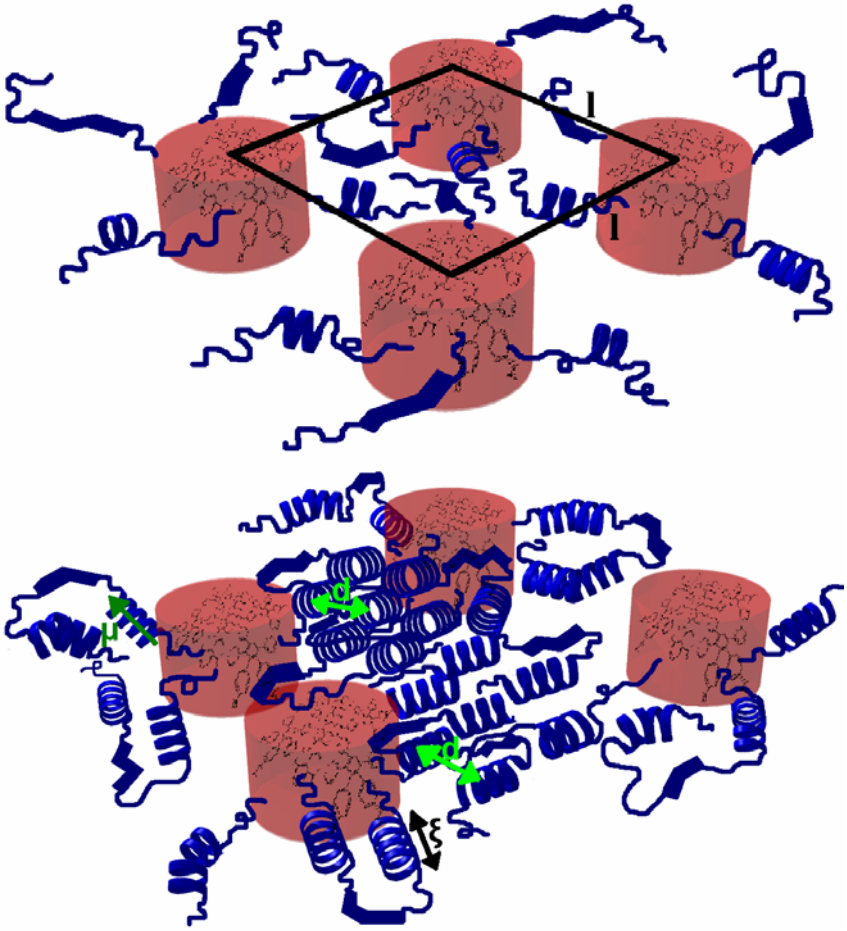

Figure 8.6. Schematic representation of the self-assembly in the functionalized polyphenylene dendrimers with (up) short polypeptides (N<16) and (down) longer polypeptides (N>20). Notice in the former the absence of a well-defined secondary peptide structure and that the polyphenylene dendrimers forming the core have some degree of order as revealed from SAXS. In the latter, the α-helical secondary structure prevails (with persistence length ξ), that in addition, display packing in a hexagonal lattice (with a distance d) (WAXS). Notice the absence of correlations between the cores in this case.

8.4 Molecular dynamics by solid state NMR spectroscopy

Local dynamic processes have been studied using advanced solid state NMR methods at an effective samples temperatures of 323 K. In particular, techniques based on heteronuclear spin coherences, such as the rotor-encoded rotational-echo double resonance (REREDOR) or recoupled polarization transfer heteronuclear dipolar order rotor-encoding (REPT-HDOR)[87], can be used to determine the effective ^{13}C-^{1}H dipolar couplings via the

analysis of spinning sideband patterns observed at the ^{13}C chemical shift of the CH_n group. The chemical selectivity of ^{13}C NMR spectra allows the assignment of dynamic processes to specific molecular sites and helps in elucidating the molecular origin of these dynamic processes. The dipolar coupling constant for two nuclear spins i and j spaced by an inter-nuclear distance of r_{ij} is

$$D_{ij} \sim \frac{1}{r_{ij}^{3}} \cdot \frac{1}{2}\left(3\cos^2\theta_{ij} - 1\right) \tag{8.1}$$

where θ_{ij} is the angle of the internuclear tensor r_{ij} with respect to the external magnetic field. From the dipolar coupling constant a local dynamic order parameter S_{ij} can be defined that is independent of the internuclear distances of the coupled spins as the ratio of the motionally averaged dipole-dipole couplings and that of rigid group:

$$S_{ij} = \left\langle \frac{1}{2}\left(3\cos^2\theta_{ij}(t) - 1\right) \right\rangle_t = \frac{\left\langle D_{ij}(t) \right\rangle_t}{D_{ij,static}} \tag{8.2}$$

For fast isotropic reorientational motions the dynamic order parameter vanishes because the effective dipolar coupling, D_{ij}, is averaged to zero, whereas for uniaxial rotations S_{ij} depends on the angle between the internuclear tensor with the rotation axis through the second Legendre polynomial.

The solid state NMR ^{13}C-^{1}H REREDOR recoupling technique was used to record spinning sideband patterns for most of the poly-L-lysine functionalized polyphenylene dendrimers under investigation. From these patterns, the effective ^{13}C-^{1}H dipolar couplings were derived and the associated local dynamic order parameters, S, were determined and the results are summarized in Table 8.2. As an example, we show in Figure 8.7 the recorded spinning sideband patterns together with the computed patterns for compound $\mathbf{G_1F_4N_{14}}$ (N=14). The number and intensity of these spinning sideband patterns originates from the ratio of the dipolar coupling constant and the magic angle spinning frequency. In general, the bigger the intensity of higher order sidebands, in comparison to the central band, the stronger the dipolar couplings and the associated local dynamic order parameters.

The results presented in Table 8.2 reveal that on the time scale of the NMR experiment (30 kHz, i.e. $\tau \sim 10^{-5}$s at 323 K) the polyphenylene core, as well as the peptide

backbone, are essentially frozen (typically *S*~0.9-1), whereas the poly-L-lysine side groups are generally characterized by a gradient of mobility from the rigid backbone towards the more mobile end CH_2 groups (the *S* values of the side groups presented in Table 8.2 are an average of the local dynamic order parameters of the C_β, C_γ, and C_δ CH_2 moieties, as the *S* values of the C_ε CH_2 groups are reported separately). As expected, the highest residual anisotropy of the recoupled dipolar ^{13}C-^{1}H interaction is observed for the C_β CH_2 moieties (adjacent to the polypeptide backbone), where the lower degree of motional freedom gives rise to a higher local dynamic order parameter. The dipolar coupling constants gradually decreased towards the C_ε CH_2 groups, as the values determined for the side CH_2 moieties were in the range D_{CH2} = 11.5 - 14 kHz (*S* = 0.50 – 0.70) for the different poly-L-lysine functionalized polyphenylene dendrimers. Furthermore, the side group dynamics seem to be independent of the poly-L-lysine molecular weight and type of secondary structure.

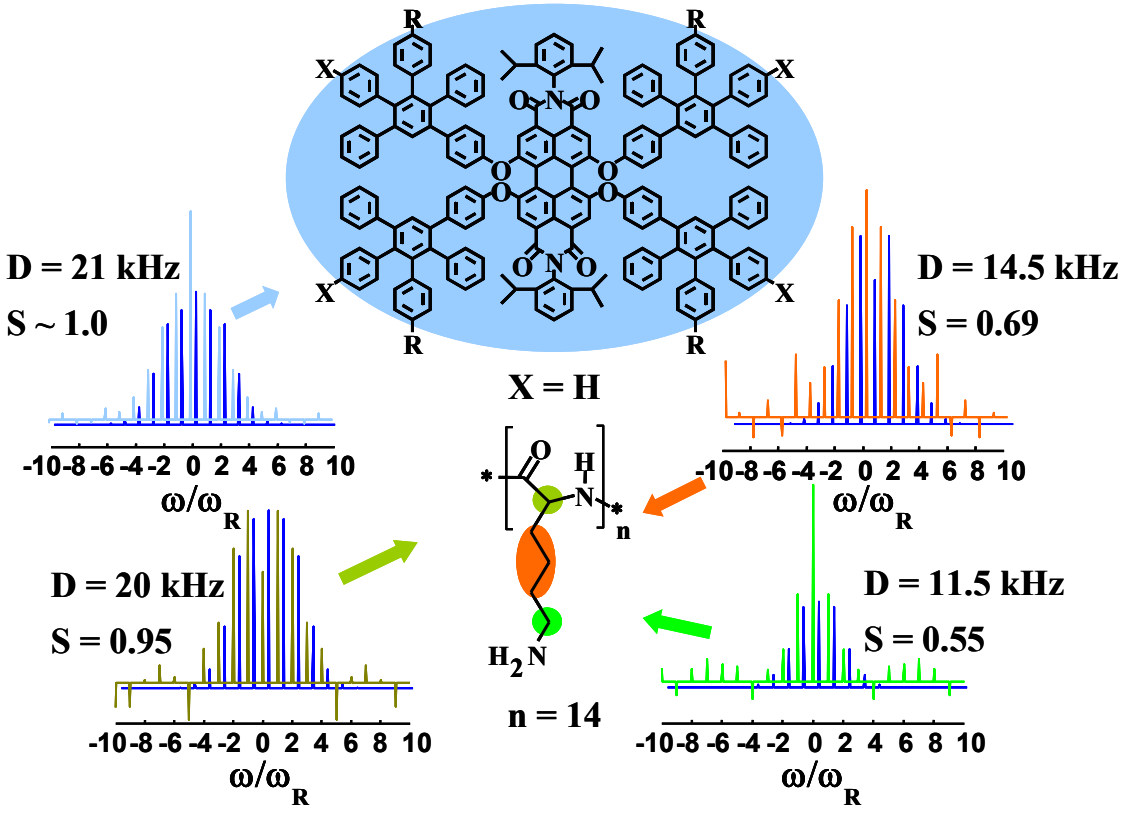

Figure 8.7 REREDOR sideband patterns recorded at 30 kHz MAS, 67.2 μs recoupling time and 323 K effective sample temperature for compound $\mathbf{G_1F_4N_{14}}$, with the simulated patterns (blue) superimposed. The effective ^{1}H-^{13}C dipolar coupling constants, together with the related local dynamic order parameters, *S*, for the phenyl rings, the peptide backbone and the peptide side groups are summarized in Table 8.2. These results suggest a practically frozen polyphenylene core and a mobility gradient in going from the relatively immobile peptide backbone to the side chains.

The dynamic order parameters of the side CH_2 moieties are remarkably high with values (0.50-0.70) typically found in nematic or even smectic liquid crystals.[164] This suggests that these groups take part in a supramolecular organization, possibly due to hydrogen bonding of the pendant amine groups. This is particularly true for compounds **$G_2F_8N_{22}$**, **$G_2F_{16}N_{58}$** and **$G_1F_4N_{84}$**, where the determined average dynamic order parameters of the C_ε CH_2 moieties are as high as for the C_β, C_γ and C_δ methylene groups. As described in detail elsewhere[51,165], the dynamic order parameter values can be rationalized in terms of mean excursion angles that the respective group explores during its motion. The excursion angles for C_β, C_γ and C_δ CH_2 (as an average) and C_ε CH_2 groups (Figure 8.1) are also given in Table 8.2. Based on these mean excursion angles, it is possible to define the space volume which the side CH_2 groups occupy in their motion.

The present solid state NMR study reveals that the side groups, for most of the poly-L-lysine functionalized polyphenylene dendrimers, explore a conical shaped[166] space volume in the course of their motion with an opening at the C_ε CH_2 position of about 47-60° with only two exceptions (**$G_1F_4N_{54}$** and **$G_2F_8N_{37}$**, where the opening angle reach even higher values (Table 8.2)).

8.5 Conclusions

The study of the solid-state morphology and the associated molecular dynamics in a series of poly-L-lysine functionalized polyphenylene dendrimers as a function of the polyphenylene core size, functionality and peptide degree of polymerization revealed several unanticipated findings:

1. The self-assembly mechanism is governed by correlations between the polyphenylene cores and between the α-helical poly-L-lysine chains for the shorter and longer oligopeptides, respectively. Therefore the predominant factor controlling the self-assembly is the polypeptide length.

2. These packing requirements have consequences on the peptide secondary structures: oligolysine substituted polyphenylenes form ill-defined secondary structures, intermediate poly-L-lysines stabilize predominantly α-helical structures in contrast to their linear analogues, and longer poly-L-lysines display mixed secondary structures. Thus constrained poly-L-lysines of intermediate length can adopt secondary structures that differ

from their linear analogues. This fact is of particular importance in the design of multiple antigen peptides where knowledge of the peptide secondary structure is essential.

3. The molecular dynamics in the glassy state was investigated by analyzing spinning sideband patterns recorded using the heteronuclear recoupling REREDOR NMR technique. Thus, the identification of the site-specific geometry of the motion as well as of the dynamic order parameters for the C-H bonds on the polyphenylenes, the peptide backbone and side groups, was achieved. The results revealed a practically frozen polyphenylene core, on the timescale of the NMR experiment, and a mobility gradient in going from the rigid peptide backbone to the more mobile peptide side groups.

Chapter 9. Conclusions

The goal of this thesis was the investigation of the structure, conformation, supramolecular order and molecular dynamics of different classes of functional materials (phthalocyanine, perylene and hexa-*peri*-hexabenzocoronene derivatives and mixtures of those), all having planar aromatic cores modified with various types of alkyl chains. The planar aromatic systems are known to stack in the solid and the liquid-crystalline state due to π-π interactions forming columnar superstructures with high one-dimensional charge carrier mobility and potential application in photovoltaic devices. The different functionalities attached to the aromatic cores significantly influence the behavior of these systems allowing the experimentalists to modify the structures to fine-tune the desired thermotropic properties or charge carrier mobility. The aim of the presented studies was to understand the interplay between the driving forces causing self-assembly by relating the structural and dynamic information about the investigated system.

Structural investigations

The structural investigations were conducted using ^{1}H, ^{13}C, ^{13}C CP and ^{1}H-^{13}C correlation solid state NMR experiments and fast magic angle spinning conditions. The information from these methods (usually as a function of temperature) was used for characterization as well as a proof of purity (in some cases not reported here, paramagnetic impurities from remaining inorganic catalysts lead to complete loss of signal; or a dramatic reduction of the ^{13}C CP efficiency occurred due to solvent remaining in the samples).

Phase behavior

It is well known that planar aromatic systems modified with alkyl chains adopt liquid-crystalline behavior and the transition temperatures between the different thermotropic phases depend strongly on the chain length, branching or additional functionalization. The application of VT solid state NMR techniques (^{1}H, ^{1}H-^{1}H DQ BaBa, ^{13}C CP, ^{1}H-^{13}C TEDOR) is used to characterize the molecular dynamics in the different phases of the phthalocyanine octaesters in addition to the DSC measurements (chapter 6), WAXS or optical microscopy. It was found that a columnar discotic LC phthalocyanine derivative (Pch2-$(COOC_8)_8$) enters the mesophase *via* a transition state, characterized by signals typical for both solid crystalline and liquid-crystalline phases. Furthermore, it was shown that in a temperature range of *ca.* 15°C in the *mesophase* (as seen from the DSC trace) the Pch2-

($COOC_{8,4}$)$_8$ disc dynamics significantly changes at the coalescence point (from slow to fast exchange regime).

Conformational analysis

Peptide backbones or long alkyl chains were the subject of the conformational analysis performed by ^{13}C CP NMR spectroscopy at fast MAS conditions.

The different types of peptide secondary structure are related with conformation-dependent ^{13}C chemical shifts, which arise from local conformations of individual amino acid residues characterized by the dihedral angles (ϕ and ψ) and the type of hydrogen bonding (intra- or intermolecular). The results of the conformational analysis of polylysine-substituted polyphenylene dendrimers reveal that oligolysine substituted polyphenylenes form ill-defined secondary structures, intermediate poly-L-lysines stabilize predominantly α-helical structures, and longer poly-L-lysines display mixed secondary structures. Furthermore, it was found that constrained poly-L-lysines of intermediate length could adopt secondary structures that differ from those of their linear analogues. Finally, it was shown that the type of peptide backbone conformation, which is directly related with the backbone length, has consequences on the self-organization of the polyphenylene dendrimers in the solid state.

The so-called *γ-gauche* effect was examined in respect to the perylene derivative (PTCDI) C_{18} chains and the shorter C_8 chains of phthalocyanine compound (Pch2-($COOC_8$)$_8$) by applying solid state ^{13}C MAS NMR spectroscopy. The different methylene ^{13}C chemical shifts, related with different chain conformations, allow distinguishing between the extended trans- (characteristic for crystalline chains or chain segments) and the energetically less favourable gauche conformation (typical for amorphous chains) of the alkyl CH_2 groups. Temperature dependent change from trans- (at low temperatures) to gauche-conformation (increasing the temperatures) was found in the studies presented here.

Supramolecular order

The supramolecular arrangement of the stacked molecules was investigated using combined ^{1}H NMR and ^{1}H-^{1}H DQ MAS NMR and 2D WAXS. The reason for choosing these experiments is the abundant information enclosed in the differences between the ^{1}H chemical shifts in solution compared to the solid state as well as the differences in solid state ^{1}H chemical shifts of otherwise chemically equivalent protons in the same molecule. Such

differences arise from the shielding effects of the neighboring aromatic systems above and below, leading to different electronic environments, respectively ^{1}H shifts.

Tilted disc arrangement in columns (the so-called “herringbone” packing) was found in the crystalline state of all investigated HBC derivatives symmetrically modified with alkyl chains (with no additional functionalities), as well as in the phthalocyanine octaester Pch2-$(COOC_8)_8$ by 2D WAXS and solid state NMR techniques. In the mesophase the HBCs adopted planar disc orientation in respect to the columnar axis (chapter 5). Contrary (chapter 6), tilted Pch2-$(COOC_8)_8$ discs were still observed in the LC phase. Increasing the steric requirements of the substituting chains by introducing branches resulted in lower mesophase transition and lower intracolumnar order in the Pch2-$(COOC_{8,4})_8$ derivative.

In the mixture of phthalocyanine discotic (Pch2-$(OC_{14,10})_4$)and perylene lath-like (PTCDI) mesogens due to peak overlap in the ^{1}H spectrum, the two components could not be distinguished one from the other. Thus, ^{13}C NMR methods and related recoupling techniques with signal detection on the carbon channel were used. The study (chapter 7) revealed that the addition of a small amount of the PTCDI component to the abundant phthalocyanine derivative resulted in enlarged LC phase of the mixture compared to the pure Pch2-$(OC_{14,10})_4$ component and significantly improved supramolecular order.

The study on the organization of the poly-L-lysine polyphenylenes (chapter 8) with different size of the aromatic cores and polylysine chain lengths revealed that the predominant factor controlling the self-assembly is the polypeptide length.

Molecular dynamics

Solid state ^{13}C-^{1}H recoupling NMR techniques (REREDOR, REPT-HDOR) as well as the ^{1}H-^{1}H homonuclear recoupling BaBa method, were applied to investigate the fast molecular dynamics of the functional materials via the analysis of the recorded spinning sideband patterns. The molecular dynamics evaluation was conducted in terms of local dynamics order parameters related with the reduction of site-specific ^{13}C-^{1}H and ^{1}H-^{1}H dipole-dipole couplings.

In most of the cases discussed in the present work, the systems under investigation contained large aromatic cores with flexible side chains or long peptide backbones attached. In the solid state the large aromatic systems or backbones were rigid or completely frozen ($S \rightarrow 1$). The only exception was the perylene derivative ($S = 0.67$), which behaved like a plastic crystal, retaining significant mobility in the solid state (chapter 6). The reduction of

the dipole-dipole couplings in this case was related with 180° jumps/vibrations around the twofold symmetry of the molecule.

Entering the liquid-crystalline state (if present) the discotic molecules start a rapid rotation about the columnar axis, which motion resulted in a 50% reduction of the dipole-dipole coupling constants related with the dipolar tensors situated in the molecular plane. Further reduction of the dipolar coupling constants was attributed to out-of-plane fluctuations of the discs.

The alkyl chains/side groups attached to the aromatic systems were typically characterized by a gradient of mobility starting from the most rigid core towards the chain ends. Only in some cases (HBC-$C_{10,6}$ – chapter 5, Pch2-$(COOC_8)_8$ in the mesophase – chapter 6 and the macrocycle on Figure 3.11 in the mesophase – chapter 3) all chain sites were characterized by similar local dynamic order parameters.

The combined structural and dynamics information acquired by solid state NMR, together with complementary methods like X-ray diffraction, DSC, and microscopy in general, resulted in full characterization of the functional materials studied and served as basis for fine-tuning the structures, respectively favorable properties for use in devices.

Appendix.

Experimental Details

Solid state NMR. The solid state NMR experiments were carried out on digital Bruker Avanche type spectrometers with B_0 fields corresponding to ^1H resonance frequencies of 500.12 MHz (DSX500, 11.74 T, 89 mm bore magnet) and 700.13 MHz (DRX700, 16.4 T, standard 54 mm bore magnet). The MAS experiments were carried out using commercial 2.5 mm or 4.0 mm MAS double/triple resonance probes, manufactured by Bruker, at spinning speeds varying from 12 kHz to 30 kHz.

At high spinning speeds, the heating effects caused by the air friction become significant. All reported sample temperatures were corrected for these effects using the resonance of ^{119}Sn of $Sm_2Sn_2O_7$ as a chemical shift thermometer, following the known procedure.

In all ^{13}C-detected experiments, the TPPM decoupling scheme was applied for dipolar decoupling, using 170° pulses and a phase modulation angle of 30°. Ramped-CP (80-100%) was used for the experiments where initial cross-polarization was needed.

A modified Julabo F83 ultra-low refrigerated circulator was used for sample cooling.

WAXS. All 2D WXAS experiments presented in this thesis were performed on oriented by filament extrusion samples. The 2D WAXS measurements on the "dove-tail" HBC derivatives, presented on Figure 5.9 in chapter 5 were conducted by Dr. W. Pisula, the 2D WAXS experiments presented on Figure 6.7 in chapter 6 were performed by Michael Bach and those on Figure 8.5 in chapter 8 by Prof. Dr. Floudas. For the measurements a rotating anode (Rigaku 18 kW9 X-ray beam with a pinhole collimation and a 2D detector (Siemens) with 1024x1024 pixels was used. A double graphite monochromator for the CuK_α radiation (λ = 0.154 nm) was used. The beam diameter was about 0.5 mm and the distance sample to detector was 80 mm. The patterns recorded were with vertical orientation of the filament axis and with the beam perpendicular to the filament.

The X-ray diffractogram of PTCDI presented on Figure 7.11 in chapter 7 was recorded by Bertrand Donnio in Strasbourg.

SAXS. SAXS measurements were made at the X27C beamline at Brookhaven National Laboratory. The wavelength was 0.1371 nm, and the sample-to-detector distance was at 2.173 m.

DSC. DSC measurements were run on a Mettler-Toledo heat-flux DSC-30 at a heating/cooling rate of 10°C/min.

Simulation Programs. The simulations of the sideband patterns generated by the various recoupling techniques were carried out using the Sidebands program based on Matlab routines, which calculate the analytical expressions for the different experiments. The program was created by Dr. A. Hofmann and modified by M. Schultz-Dobrick.

Bibliography

[1] Purcell, E. M.; Torrey, H. C.; Pound, R. V, *Phys. Rev.* **1946**, 69, 37
[2] Bloch, F.; Hansen, W. W.; Packard, M. E., *Phys Rev.* **1946**, 70, 474
[3] Lauterburg, P. C., Image formation by induced local interactions: examples employing nuclear magnetic resonance, *Nature* **1973**, 242:190, 1973
[4] Mansfield, P.; Grannell, P. K., NMR "diffraction" in solids?, *J. Phys. Chem.: Solid State Phys.* **1973**, 6, L422-L426
[5] Andrew, E. R.; Bradbury, A.; Eades, R. G., Nuclear Magnetic Resonance Spectra from a Crystal Rotated at High Speed, *Nature* **1958**, *182*, 1659
[6] Lowe, I. J., Free Induction Decay of Rotating Solids, Phys. Rev. Lett. **1959**, *2*, 285
[7] Ernst, M.; Samosoon, A.; Meier, B. H., Low-power Decoupling in Fast Magic Angle Spinning NMR, Chem. Phys. Lett. **2001**, *348*, 293
[8] Samoson, A.; Tuherm, T., High Performance MAS (2003), Poster contribution at the ENC 2003
[9] Gullion, T.; Schaefer, J., Rotational Echo Double-Resonance NMR, J. Magn. Reson. **1989**, *81*, 196
[10] Carravetta, M.; Eden, M.; Zhao, X.; Brinkmann, A.; Levitt, M. H., Symmetry Principles for the Design of Radio Frequency Pulse Sequences in Nuclear Magnetic Resonance of Rotating Solids, Chem. Phys. Lett. **2000**, *321*, 205
[11] Van de Craats, A. M.; Warman, J. M. ; Fechtenkoetter, A.; Brand, J. D.; Harbison, M.; Müllen, K., Record Charge Carrier Mobility in a Room Temperature Discotic Liquid Crystalline Derivative of Hexabenzocoronene, Adv. Mater. **1999**, *11*, 1469
[12] Sakurai, J. J., *Modern Quantum Mechanics* **1994**, Addison-Wesley Publishing Co., 72
[13] Levitt, M. H., *Spin Dynamics:Basics of Nuclear Magnetic Resonance* **2001**, John Wiley&Sons, Ltd, 144
[14] Fischbach, I.; Ebert, F.; Spiess, H. W.; Schnell, I., Rotor modulations and recouling startegies in 13C solid-state magic-angle-spinning NMR spectroscopy: Probing molecular orientations and dynamics, *ChemPhysChem* **2004**, 5, 895
[15] Rutar, V.; Blinc, R.; Vilfan, M.; Zann, A.; Dubois, J. C., *J. Phys.* **1982**, 43, 761
[16] Meriles, C. A.; Sakellariou D.; Moule, A.; Goldman, M.; Budinger, T. F.; Pines, A., High resolution of static samples by rotation of magnetic field, *J. Magn. Reson.* **2004**, 169, 13
[17] Sakellariou D.; Meriles, C. A.; Martin M. W.; Pines, A., NMR in rotating magnetic fields: magic angle field spinning, *Magn. Reson. Imaging* **2005**, 23, 295
[18] Maricq, M. M.; Waugh, J. S., NMR in rotating solids, *J. Chem. Phys.* **1979**, 70, 3300
[19] Filip, C.; Hafner, S.; Schnell, I.; Demco, D. F.; Spiess, H. W., Solid-state nuclear magnetic resonance spectra of dipolar-coupled nuclear spin systems under fast magic angle spinning, *J. Chem. Phys*. **1999**, 110, 423-440
[20] Marion, D.; Wüthrich, K., Application of Phase Sensitive Two-dimensional Correlated Spectroscopy (COSY) for Measurements of H-1 H-1 Spin-spin Coupling constants in Proteins. *Biochem. Biophys. Res. Commun.* **1983**, 113, 967–974
[21] Marion, D.; Ikura, M.; Tschudin, R.; Bax A., Rapid Recording of 2D NMR-Spectra without Phase Cycling- Application to the Study of Hydrogen-Exchange in Proteins. *J. Magn. Res,***1989***,* 85, 393–399
[22] Herzfeld, J.; Berger, A. E., Sideband Intensities in NMR Spectra of Samples Spinning at the Magic Angle. J. Chem. Phys. **1980**, 73, 6021–6030
[23] Stejskal, E. O.; Schaefer, J.; McKay, R. A., High-Resolution, Slow-Spinning Magic-Angle Carbon-13 NMR. *J. Magn. Res.* **1997**, 25, 569–573

[24] Blümich, B.; Hagemeyer, A.; Schaefer, D.; Schmidt-Rohr, K.; Spiess, H. W., Solid State NMR Spectroscopy in Polymer Science, *Adv. Mat,* **1990**, 2, 72–81
[25] Gullion, T.; Schaefer, J., Rotational-Echo Double-Resonance NMR. *J. Magn. Reson.* **1989**, 81, 196–200
[26] Carravetta, M.; Edén, M.; Zhao, X.; Brinkmann, A.; Levitt, M. H.,. Symmetry Principles for the Design of Radiofrequency Pulse Sequences in the Nuclear Magnetic Resonance of Rotating Solids. *Chem. Phys. Lett.* **2000**, 321, 205–215
[27] Brinkmann, A.; Edén, M.; Levitt, M. H., Synchronous Helical Pulse Sequences in Magic-angle Spinning Nuclear Magnetic Resonance. *J. Chem. Phys*. **2000**, 112, 8539–8554
[28] Zhao, X.; Edén, M.; Levitt, M. H., Recoupling of Heteronuclear Dipolar Interactions in Solid-state NMR Using Symmetry-based Pulse Sequences. *Chem. Phys. Lett.,* **2001**, 342, 353–361
[29] Gullion, T.; Schaefer. J., Detection of Weak Heteronuclear Dipolar Coupling by Rotational-Echo Double-Resonance Nuclear Magnetic Resonance. *Adv. Magn. Reson.* **1989**, 13, 57–83
[30] Feike, M.; Demco, D. E.; Graf, R.; Gottwald, J.; Hafner, S.; Spiess, H. W. Broadband Multiple-Quantum NMR Spectroscopy. *J. Magn. Reson. A* **1996**, 122, 214–221
[31] Fernandez, C.; Lang, D. P.; Amourex, J.-P. ; Pruski, M., Measurement of dipolar interactions between quadrupolar and and spin-½ nuclei in solids by multiple quantum REDOR NMR, *J. Am. Chem. Soc.* **1998**, 120, 2672-2673
[32] Gullion, T.; Baker, D. B.; Conradi, M.S., New, Compensated Carr-Purcell Sequences, *J. Magn. Reson*..,**1990**, 89, 479–484
[33] Saalwächter, K.; Graf, R.; Spiess, H. W., Recoupled Polarization-Transfer Methods for Solid-State ^{1}H-^{13}C Heteronuclear Correlation in the Limit of Fast MAS, *J. Magn.Reson.* **2001**, 148, 398–418.
[34] Saalwächter, K.; Schnell, I., REDOR-based Heteronuclear Dipolar Correlation Experiments in Multi-spin Systems: Rotor-encoding, Directing and Multiple Distance and Angle Determination, *Solid State Nucl. Magn. Res.* **2002**, 22, 154–187
[35] Hing, A. W.; Vega, S.; Scheaefer, J., Transfer-echo double resonance NMR, *J. Magn. Reson.* **1992**, 96, 205-209
[36] Hing, A. W.; Vega, S.; Scheaefer, J., easurement of heteronuclear dipolar coupling by transferred-echo double-resonance NMR, *J. Magn. Reson. A* **1993**, 151-162
[37] Schnell, I.; Spiess, H. W., Advances in Magnetic Resonance: High resolution ^{1}H NMR Spectroscopy in the Solid State: Very Fast Sample Rotation and Multiple-quantum Coherences. *J. Magn. Reson.* **2001**, 151, 153–227.
[38] Graf, R.; Demco, D. E.; Hafner, S.; Spiess, H. W., Selective Residual Dipolar Couplings in Cross-linked Elastomers by ^{1}H Double-quantum NMR Spectroscopy, *Solid State Nucl. Magn. Reson.* **1998**, 12, 139–152.
[39] Höger, S.; Cheng, X. H.; Ramminger, A. D.; Enkelmann, V.; Rapp, A.; Mondeshki, M.; Schnell, I., Discotic Liquid Crystals with an Inverted Structure, *Angevandte Chemie Int. Ed.* **2005**, 44, 2801-2805
[40] Möller, M:, Wendorf, J. H.; Wert, M.; Spiess, H. W.; Bengs, H.; Karthaus, O.; Ringsdorf, H., Molecular dynamics of discotic charge-transfer complexes, dielectric spectroscopy and ^{2}H NMR study, *Liq. Cryst.* **1994**, 17, 381-395
[41] DeAzevedo, E. R.; Hu, W.-G; Bonagamba, T.; Schmidt-Rohr, K., Principles of centerband-only detection of exchange in solid-state nuclear magnetic resonance, and extension to four-time centerband-only detection of exchange, *J. Phys. Chem.* **2000**, 112 (20), 8988-9021
[42] DeAzevedo, E. R.; Hu, W.-G; Bonagamba, T.; Schmidt-Rohr, K., Centerband-only detection of exchange: Efficient analysis of dynamics in solids by NMR, *J. Am. Chem. Soc.* **1999**, 121, 8411-8412

[43] Reichert, D.; Bonagamba, T.; Schmidt-Rohr, K., Slow-down of ^{13}C spin diffusion in organic solids by fast MAS: A CODEX NMR study, *J. Magn. Reson.* **2001**, 151, 129-135
[44] Fischbach, I, *PhD thesis*, **2003**
[45] Spiess, H. W., Deutron spin alignment: A probe for studying ultraslow motions in solids and solid polymers, *J. Chem. Phys.* **1980**, 72, 6755-6762
[46] Schmidt, A.; Smith, S. O.; Raleigh, D. P.; Roberts, J. E.; Griffin, R. G.; Vega, S., Chemical exchange effects in the NMR spectra of rotating solids., *J. Chem. Phys.* **1986**, 85, 4248-4253
[47] Vanderhart, D. L.; Earl, W. L.; Garroway, A. N., Resolution in 13C NMR of organic solids using high power proton decoupling and magic angle sample spinning., *J. Magn. Reson.* **1981**, 44, 361-401
[48] Long, J. R.; Sun, B. O.; Bowen, A.; Griffin, R. G., Molecular dynamics and magic angle spinning NMR, *J. Am. Chem. Soc.* **1994**, 116, 11950-11956
[49] Ishii, A.; Ashida, J.; Terao, T., ^{13}C-^{1}H Dipolar recoupling dynamics in ^{13}C multiple pulse solid sate NMR, *Chem. Phys. Lett.* **1995**, 246, 439-445
[50] Atkins, P.; De Paula, J., *Physical Chemistry*, Oxford University Press, **2006**
[51] Schmidt-Rohr, K.; Spiess, H.W., Multidimensional Solid State NMR and Polymers, Academic press, New York, **1994**
[52] Fischbach, I.; Ebert, F.; Spiess, H. W.; Schnell, I., Rotor Modulations and Recoupling Strategies in ^{13}C Solid-State Magic-Angle Spinning NMR Spectroscpy: Probing Molecular Orientation and Dynamics, *ChemPhysChem* **2004**, 5, 895-908.
[53] Kwasniewski, S. P.; Francois, J. P.; Deleuse, M. S., Temperature effects on the UV-VIS Electronic spectrum of trans-stilbene, *Int. J. Quant. Chem.* **2001**, 85, 557-568
[54] Shen, Y.; Chen, E. Q.; Ye, C.; Zhang, H. L.; Wu, P. Y.; Noda, I.; Zhou, Q. F., Liquid-crystalline phase development of a mesogen-jacketed polymer – Application of two-dimensional infrared correlation analysis, *J. Phys. Chem. B* **2005**, 109, 6089-6095
[55] Painter, P.; Sobcowaik, M.; Park, Y., Vibrational relaxation in atactic polystyrene, *Macromolecules* **2007**, 40, 1730-1737
[56] Zorrilla, S.; Hink, M. A.; Visser, A. J. W. G.; Lillo, M. P., Translational and rotational motions of proteins in a protein crowded environment, *Biophys. Chem.* **2007**, 125, 298-305
[57] Wind, M.; Saalwächter, K.; Wiesler, U. M.; Müllen, K.; Spiess, H. W., Solid-state NMR investigation of molecular dynamics in polyphenylene dendrimers, *Macromolecules* **2002**, 35, 10071-10086
[58] Leisen, J.; Schmidt-Rohr, K.; Spiess, H. W., Multidimensional H-2 NMR studies of the nonexponencial chain relaxation of polystyrene above the glass transition, *J. Non-cryst. Solids* **1994**, 172, 737-750
[59] Schweiger, A.; Jeschke, G., *Principles of pulse electron paramagnetic resonance*, **2001**, Oxford university press, Oxford
[60] Graf, R.; Ewen, B.; Spiess, H. W., Geometry of phenylene motion in polycarbonate from NMR spectroscopy and neutron scattering, *J. Chem. Phys.* **2006**, 126
[61] Kremmer, F.; Schönhals, A., Eds., *Broadband dielectric spectroscopy*, Spinger, **2002**
[62] Mondeshki, M.; Mihov, G.; Graf, R.; Spiess, H. W.; Müllen, K.; Papadopoulos, P.; Gitsas, A., Floudas, G., Self-assembly and mlecular dynamics of peptide-functionalized polyphenylene dendrimers, *Macromolecules*, **2006**, 39, 9605-9613
[63] Höger, S.; Enkelmann, V.; Bonrad, K.; Tschierske, C., *Angew. Chem. Int. Ed.* **2000**, 39, 13, 2267-2270
[64] Fischer, M.; Lieser, G.; Rapp, A.; Schnell, I.; Mamdouh, W.; De Feyter, S.; De Schryver, F.; Höger, S., *J. Am. Chem. Soc.* **2004**, 126, 214-222
[65] Chandrasekhar, S.; Sadashiva, B. K.; Surish, K. A. *Pramana* **1977**, *9*, 471-480
[66] Kohne, B.; Praefcke, B., *Ang. Chem. Int. Ed.* **1984**, 23, 82
[67] Halleux, A.; Martin, R. H.; King, G. S. D. *Helv. Chim Acta* **1958**, 41, 1177-1182

[68] Iyer, V. S.; Wehmeier, M.; Brand, J. D.; Keegstra, M. A.; Müllen, K. *Angew. Chem., Int. Ed. Engl.* **1997**, *36*, 1604-1607; *Angew. Chem.* **1997**, *109*, 1675-1679
[69] Whitlock, J. D.; Panayotatos, P.; Sharma, G. D.; Cox, M. D.; Sauers, R. R.; Bird, G. R., Investigatins of materials and device structures for organic semiconductor solar cells, *Opt. Eng.* **1993**, 32, 1921-1934
[70] Yasuda, T.; Saito, M.; Nakamura, H.; Tsutsui, T., Control of p- and n-type carriers by end-group stabilization in oligo-p-phenylenevinylene-based organic field-effect transistors, *Appl. Phys. Let.* **2006**, 89, 182108
[71] Davis, W. B.; Ratner, M. A.; Wasielewski, M. R., Conformatioanl gating of long distance electron transfer through wire-like bridges in donor-bridge-acceptor molecules, *J. Am. Chem. Soc.* **2001**, 123, 7877-7886
[72] van de Craats, A. M.; Warman J. M. ; Müllen K. ; Geerts Y.; Brand, J. D. *Adv. Func. Mater.* **1998**, 10, 36-38
[73] Kastler, M.; Pisula, W.; Wasserfallen, D.; Pakula, T.; Müllen, K. *J. Am. Chem. Soc*. **2005**, *127*, 4286-4296
[74] Fechtenköttet, A.; Tchebotareva, N.; Watson, M.; Müllen, K. *Tetraedron* **2001**, 57, 3769-3783
[75] Wu, J.; Watson, M.; Li, Z.; Wang, Z.; Müllen, K. *J. Am. Chem. Soc*. **2004**, *126*, 177-186
[76] Thünemann, A. F.; Kubowicz, S.; Burger, C.; Watson, M.; Tchebotareva, N.; Müllen, K. *J. Am. Chem. Soc*. **2003**, 125, 352-356
[77] Mondeshki, M.; Floudas, G.; Spiess, H. W., unpublished results
[78] Ochsenfeld, C.; Brown, S.; Schnell, I.; Gauss, J.; Spiess, H. W., Structure asignment in the solid state by coupling quantum chemical calculations with NMR experiments: A columnar hexabenzocoronene derivative, *J. Am. Chem. Soc.* **2001**, 123, 2597-2606
[79] Ochsenfeld, C.; Brown, S. P.; Schnell, I.; Gauss, J.; Spiess, H. W. *J. Am. Chem. Soc*. **2001**, *123*, 2597-2606
[80] Brown, S; Schnell I.; Brand J. D.; Müllen, K.; Spiess, H. W. *J. Am. Chem. Soc.* **1999**, 121, 6712-6718
[81] Goldfarb, D.; Luz, Z.; Zimmermann, H., *J. Chem. Phys.* **1981**, 42, 1803
[82] Brown, S; Schnell I.; Brand J. D.; Müllen, K.; Spiess, H. W. *J. Mol. Struct.* **1999**, 521, 179-195
[83] Fischbach I.; Pakula T.; Piotr M.; Fechtenkötter A.; Müllen K.; Spiess H. W. *J. Phys. Chem. B* **2002**, 106, 6408-6418
[84] Wasserfallen D.;Fischbach I.; Chebotareva N.; Kastler M.; Pisula W.; Jäckel F.; Watson M.; Schnell I.; Rabe J. P.; Spiess H. W.; Müllen K. *Adv. Func. Mater.* **2005**, 15, 1585-1594
[85] Pisula, W.; Kastler, M.; Wasserfallen, D.; Mondeshki M.; Schnell I.; Müllen K.; Spiess H. W., Relation between supramolecular order and charge carrier mobility of branched alkyl hexa-*peri*-hexabenzocoronenes, *Chem. Mater.* **2006**, 18, 3634-3640
[86] Saalwächter, K.; Schnell, I.; *Solid State Nucl.Magn. Res.* **2002**, *22*, 154-187
[87] Saalwachter, K.; Graf, R; Spiess, H. W. *J. Magn. Reson.* **2001**, *148* (2), 398-418
[88] Saalwächter, K.; Spiess, H. W., Heteronuclear ^{1}H-^{13}C spin correlation in solid state nuclear magnetic resonance: Combining rotational-echo double-resonance recoupling and multiple-quantum spectroscopy, *J. Chem. Phys.* **2001**, 114, 5707-5728
[89] Schultz-Dobrick, M.; Metzroth, T.; Spiess, H. W.; Gauss, J.; Schnell, I. *ChemPhysChem* **2005**, *6*, 315-327
[90] Fischbach, I.; Pakula, T.; Minkin, P.; Fechtenkötter, A.; Müllen, K.; Spiess, H. W.; Saalwächter, K., Structure and dynamics in columnar discotic materials: A combined X-ray and solid state NMR study of hexabenzocoronene derivatives, *J. Phys. Chem. B* **2002**, 106, 6408-6418

[91] deAzevedo, E. R.; Hu, W.-G.; Bonagamba, T. J.; Schmidt-Rohr, K., Centerband-only detection of exchange: Efficient analysis of dynamics in solids by NMR, *J. Am. Chem. Soc.* **1999**, 121, 8411-8412
[92] Van de Craats, A. M.; Warman, J. M. ; Fechtenkoetter, A.; Brand, J. D.; Harbison, M.; Müllen, K., Record Charge Carrier Mobility in a Room Temperature Discotic Liquid Crystalline Derivative of Hexabenzocoronene, Adv. Mater. **1999**, *11*, 1469
[93] Langer, B.; Schell, I.; Spiess, H. W.;Grimmer, A.-R., J.Magn. Res. **1999**, *138*, 182-186
[94] Kranig, W.; Boeffel, C.; Spiess, H. W., ^{2}H NMR studies of molecular motions and allignment processes of discotic liquid-crystalline compounds based on substituted triphenylenes, *Macromolecules* **1990**, 23, 4061-4067
[95] Percec, V.; Clodde, M.; Bera, T. K.; Miura, Y.; Shiyanovskaya, I.; Singer, K. D.; Balagurusamy, V. S. K.; Heiney, P. A.; Schnell, I.; Rapp, A.; Spiess, H. W.; Hudson, S. D. ; Duan, H., Self-organization of supramolecular helical dendrimers into complex electronic materials, *Nature* **2002**, 419, 384-387
[96] Schnell, I., *Prog. Nucl. Magn. Res. Spec.* **2004**, 45, 145-207
[97] Schmidt-Mende, L.; Fechtenkötter, A.; Müllen, K.; Moons, E.; Friend, R. H.; MacKenzie, J. D., *Science*, **2001**, 293, 1119
[98] van de Craats, A. M.; Stutzmann, N.; Bunk, O. ; Nbielsen, M. M.; Watson, M.; Müllen, K.; Chanzy, H. D.; Sirringhaus, H.; Friend, R. H., *Adv. Mater.* **2003**, 15, 495
[99] Pisula, W.; Menon, A.; Stepputat, M.; Lieberwirth, I.; Kolb, U.; Tracz, A.; Sirringhaus, H.; Pakula, T.; Müllen, K., *Adv. Mater.* **2005**, 17, 684
[100] Maree, M. D.; Kuznetsova, N.; Nyokong, T., Silicon octaphenoxyphthalocyanines: photostability and singlet oxygen quantum yields, *J. Photochem. Photobiol. Chem. A* **2001**, 140, 117-125
[101] Nyokong, T.; Vilakazi, S., Phthalocyanines and related complexes as electrocatalysts for the detection of nitric oxide, *Talanta* **2003**, 61, 27-35
[102] Bora, M.; Schut, D.; Baldo, M. A., Combinatorial detection of volatile organic compounds using metal phthalocyanine field-effect transistors, *Anal. Chem.* **2007**, 79, 3298-3303
[103] McKeown, N. B.; Budd, P. M.; Msayib, K. J.; Ghanem, B. S.; Kingston, H. J.; Tattershall, C. E.; Makhseed, S.; Reynolds, K. J.; Fritsch, D., Polymer of intrinsic microporosity (PIM): Bridging the void between microporous and polymer materials, *Chem. Eur. J.*, **2005**, 11, 2610-2620
[104] Gregory, P., Steamrollers, sports cars and security: phthalocyanine progress through the ages, *J. Porphyr. Phthaloc.*, **1999**, 3, 468-475
[105] Lux, A.; Rozenberg, G. G.; Petritsch, K.; Moratti, S. C.; Holmes, A. B.; Friend, R. H., A series of novel octakis(alkylthio)-substituted phthalocyanines, *Synthetic Metals*, **1999**, 102, 1527-1528
[106] Engel, M. K., Single-crystal and solid state molecular structures of phthalocyanine complexes, *Kawamura Rikagaku Kenkyusho Hokoku*, **1997**, 11-54
[107] Frydman, L.; Olivieri, A.; Diaz, L. E.; Valasinas, A.; Frydman, B., A variable temperature solid state ^{13}C CPMAS NMR analysis of meso-tetrapropylpophyrin and of octaethylporphyrin, *J. Am. Chem. Soc.*, **1988**, 110, 5651-5661
[108] Schlabach, M.; Scherer, G.; Limbach, H. H., Kinetic HH/HD/DH/DD isotope effects on nondegenerate stepwise reversible double proton transfer reactions. NMR study of the tautomerism of meso-tetramethylchlorin, *J. Am. Chem. Soc.*, **1991**, 113, 3550-3558
[109] Braum, J.; Schlabach, M.; Wehre, B.; Köcher, M.; Vogel, E.; Limbach, H. H., NMR study of the tautomerism of porphryn including the kinetic HH/HD/DD isotope effects in the liquid and in the solid state, *J. Am. Chem. Soc.*, **1994**, 116, 6593-6604

[110] Langer, U.; Hoelger, C.; Wehrle, B.; Latanowitz, L.; Vogel, E.; Limbach, H. H., ^{15}N NMR study of proton localization and proton transfer thermodynamics and kinetics in polycrystalline porphycene, *J. Phys. Org. Chem.*, **2000**, 13, 23-34
[111] Sergeyev, S.; Pouzet, E.; Debever, O.; Levin, J.; Gierchner J.; Cornil, J.; Aspe, R. G.; Geerts, Y. H., Liquid crystalline octaalkoxycarbonyl phthalocyanines: design, synthesis, electronic structure, self-aggregation and mesomorphism, *J. Mater. Chem.*, **2007**, 17, 1777-1784
[112] Dulog, L.; Gittinger, A., *Mol. Cryst. Liq. Cryst.,* **1992**, 213, 31–42
[113] Thünemann, A. F.; Kubovicz, S.; Burger, S.; Watson, M.; Tchebotareva, N.; Müllen, K., α-Helical-*within*-discotic columnar structures of a complex between poly(ethylene oxide)-*block*-poly(L-lysine) and a hexa-*peri*-hexabenzocoronene, *J. Am. Chem. Soc.*, **2003**, 125, 352-356
[114] Thünemann, A. F.; Ruppelt, D.; Ito, S.; Müllen, K., *J. Mater. Chem.*, **1999**, 9, 1055-1057
[115] Thünemann, A. F.; Ruppelt, D.; Burger, C.; Müllen, K., *J. Mater. Chem.*, **2000**, 10, 1325-1329
[116] Collard, D. M.; Lillya, C. P., *J. Am. Chem. Soc.,* **1991**, 113, 8577–8583
[117] Pisula, W.; Kastler, M.; Wasserfallen, D. ; Pakula, T.; Müllen, K., *J. Am. Chem. Soc.,* **2004**, 126, 8074–8075
[118] Brown, S.; Schnell, I.; Brand, J. D.; Müllen, K.; Spiess, H. W., The competing effects of π-π packing and hydrogen bonding in a hexabenzocoronene carboxylic acid derivative: A ^{1}H solid-state MAS NMR investigation, *Phys. Chem. Chem. Phys.*, **2000**, 2, 1735-1745
[119] Schnell, I.; Brown, S.; Low, H. Y.; Ishida, H.; Spiess, H. W., *J. Am. Chem. Soc.*, **1998**, 121, 6712
[120] Desiraju, G. R.; Gavezzoti, A., *Acta Cryst. B*, **1989**, 45, 473
[121] Gavezzoti, A.; Desiraju, G. R., *Acta Cryst. B*, **1988**, 44, 427
[122] Engel, M. K., Single crystal and solid state molecular structures of phthalocyanine complexes, *Kawamura Rikagaku Kenkuisho Hokoku, (vol. 1996)*, **1997**, 11-54
[123] Earl, W. L.; Storm, C. B.; Meier, B. H., Two-dimentional chemical exchange NMR in the solid: Proton dynamics in the phthalocyanine, *J. Am. Chem. Soc.*, **1986**, 108, 6072-6074
[124] O'Neil, M.; Kelly, S. M., *Adv. Mater.* **2003**, 15, 1135
[125] Adam, D.; Schumacher, P.; Simmerer, J.; Haussling, L.; Siemensmeyer, K.; Etzbach, K. H.; Ringsdorf, H.; Haarer, D., *Nature*, **1994**, 371, 141
[126] Yu, G.; Gao, J.; Hummelen, J. C.; Wudl, F.; Heeger, A. J., *Science* **1995**, 270, 1789
[127] Halls, J. J. M.; Arias, A. C.; MacKenzie, J. D.; Wu, W.; Inbasekaran, M.; Woo, E. P.; Friend, R. H. *Adv.Mater.* **2000**, *12*, 498.
[128] Arias, A. C.; MacKenzie, J. D.; Stevenson, R.; Halls, J. J. M.; Inbasekaran, M.; Woo, E. P.; Richards, D.; Friend, R. H., *Macromolecules*, **2001**, 34, 6005.
[129] Corcoran, N.; Arias, A. C.; Kim, J. S.; MacKenzie, J. D.; Friend, R. H. *Appl. Phys. Lett.* **2003**, *82*, 299.
[130] Babel, A.; Jenekhe, S. A., *Macromolecules*, **2004**, 37, 9835.
[131] Shaheen, S.E.; Brabec, C. J.; Sariciftci, N. S.; Padinger, F.; Fromherz, T.; Hummelen J. C., *Appl. Phys. Lett.*, **2001**, 78, 841.
[132] Wienk, M. M.; Kroon, J. M.; Verhees, W. J. H.; Knol, J.; Hummelen, J. C.; van Hal, P. A.; Janssen, R. A., *Angew. Chem. Int. Ed*., **2003**, 42, 3371.
[133] Van Duren, J. K. J.; Yang, X.; Loos, J.; Bulle-Lieuwma, C. W. T.; Sieval, A. B.; Hummelen, J. C.; Jansen, R. A., *Adv. Funct. Mater.*, **2004**, 14, 425.
[134] Hoppe, H.; Niggemann, M.; Winder, C.; Kraut, J.; Hiesgen, R.; Hinsch, A.; Meissner, D.; Sariciftci, N. S., *Adv. Funct. Mater.*, **2004**, 14, 1005.
[135] Yang, X.; Van Duren, J. K. J.; Janssen, R. A.; Michels, M. A. J; Loos J., *Macromolecules*, **2004**, 37, 2151.

[136] Hoppe, H.; Glatzel, T.; Niggemann, M.; Hinsch, A.; Lux-Steiner, M. Ch.; Sariciftci N. S., *Nano Lett.* **2005**, 5, 269.
[137] Dittmer, J. J.; Marseglia, E. A.; Friend, R. H., *Adv. Mater.* **2000**, *12*, 1270.
[138] Shtein, M.; Peumans, P.; Benziger, J. B.; Forrest, S. R., *J. Appl. Phys.* **2003**, *93*, 4005.
[139] Lemaur, V.; Steel, M.; Beljonne, D.; Brédas, J.L.; Cornil, J., *J. Am. Chem. Soc.* **2005**, *127*, 6077.
[140] Tant, J.; Geerts, Y. H.; Lehmann, M.; De Cupere, V.; Zucchi, G.; Lemaur, V.; Marcq, V.; Hennebicq, E.; Cornil, J.; Wegge Laursen, B.; Bjørnholm, T., Manuscript in preparation.
[141] Langhals, H. *Chem. Ber.* **1985**, *118*, 4645.
[142] Zucchi, G.; Donnio, B.; Geerts, Y. H., *Chem. Mater.* **2005**, 17, 4273
[143] Smith, M. ; March, J., *March´s advanced organic chemistry : Reactions, mechanisms, and structure*, John Wiley &Sons inc. **2001**, Canada
[144] Clauss, J. ; Schmidt-Rohr, K. ; Adam, A.; Boeffel, C.; Spiess, H. W., Stiff macromolecules with alyphatic side chains: Side chain mobility, conformation, and organization from 2D solid state NMR spectroscopy, *Macromolecules* **1992**, 25, 5208-5214
[145] Möller, M., *Adv. Polym. Sci.* **1985**, 66, 59
[146] Gitsas, A. ; Floudas, G. ; Dietz, M. ; Mondeshki, M.; Spiess, H. W.; Wegner, G., Self-assembly and molecular dynamics of poly(γ-methyl-L-glutamate-co-γ-stearyl-L-glutamate) copolymers, *Macromolecules*, submitted
[147] Möller, M.; Wendorf, J. H.; Werth, M.; Spiess, H. W.; Bengs, H.; Karthaus, O.; Ringsdorf, H., Molecular dynamics of discotic charge transfer complexes, dielectric spectroscopy and ^{2}H NMR studies, *Liq. Cryst.* **1994**, 17, 381-395
[148] De Gennes, P. G., *J. Phys. Lett.* **1983**, 44, 657
[149] Möller, M.; Wendorf, J. H.; Werth, M.; Spiess, H. W.; Bengs, H.; Karthaus, O.; Ringsdorf, H., Molecular dynamics of discotic charge transfer complexes, dielectric spectroscopy and ^{2}H NMR studies, *Liq. Cryst.* **1994**, 17, 381-395
[150] Duncan, R. *Nature Reviews* vol2, 2003
[151] Allen, T.M.; Cullis, P.R. *Science* **2004**, *303*, 1818
[152] Bosman, A.W. ; Janssen, H.M. ; Meijer, E.W. *Chem. Rev.* **1999**, *99*, 1665
[153] Fréchet, J.M.J.; Hawker, C.J. in *Comprehensive Polymer Science*, Aggarwal, S.L. ; Russo, S.S. (Eds), Pergamon Press, Oxford (1996)
[154] Stiriba, S.-E. ; Frey, H. ; Haag, R. *Angew. Chem. Int. Ed.* **2002**, *41*, 1329
[155] Veprek, P.; Jezek, J. *J. Peptide Sci.* **1999**, *5*, 203
[156] Lee, C.C.; Fréchet, J.M.J., *Macromolecules* **2006**, *39*, 476
[157] Lübbert, A.; Nguyen T.Q.; Sun, F.; Sheiko, S.S, Klok, H.-A. *Macromolecules* **2005**, *38*, 2064
[158] Choi, J.S.; Joo, D.K.; Kim, C. H.; Kim, K.; Park, J. S. *J. Am. Chem. Soc.* **2000**, *122*, 474
[159] Ohsaki, M.; Okuda, T.; Wada, A.; Hirayama, T.; Niidome, T.; Aoyagi, H. *Bioconjugate Chem.* **2002**, *13*, 510
[160] Wiesler, U. M.; Weil, T.; Muellen, K. *Top. Curr. Chem*. **2001**, *212*, 1
[161] Mihov, G.; Gregel-Koehler D.; Lübbert, A.; Vandermeulen G.W.M.; Herrmann, A.; Klok, H.-A.; Müllen, K. *Bioconjugate Chem*. **2005**, *16*, 283
[162] Kricheldorf, H.; Müller, D., *Macromolecules* **1983**, *16*, 615
[163] Shoji, A.; Ozaki T.; Saito, H.; Tabeta, R.; Ando I., *Macromolecules* **1984**, *17*, 1472
[164] Pressner, D.; Goeltner, C.; Spiess, H. W.; Müllen, K., *Berichte der Bunsen-Gesellschaft* **1993**, *97*, 1362
[165] Hentschel, D.; Sillescu, H.; Spiess, H. W., *Polymer* **1981**, *22*, 1516
[166] Rapp, A.; Schnell, I.; Sebastiani, D.; Brown, S.; Percec, V.; Spiess, H. W., *J Am. Chem. Soc.* **2003**, *125*, 13284